KINEMATICS OF OB STARS
IN THE
NEARBY GALACTIC DISK

INAUGURALDISSERTATION

ZUR

ERLANGUNG DER WÜRDE EINES DOKTORS DER
PHILOSOPHIE
VORGELEGT DER
PHILOSOPHISCH-NATURWISSENSCHAFTLICHEN FAKULTÄT
DER UNIVERSITÄT BASEL

VON

CAROLINE GIRARD

aus Grenchen im Kanton Solothurn

Basel, im Januar 2006

Genehmigt von der
Philosophisch-Naturwissenschaftlichen Fakultät
auf Antrag von

Prof. Dr. Ortwin E. Gerhard und Prof. Dr. Burkhard Fuchs
(Mitglieder des Dissertationskomitees)

Basel, den 14. Februar 2006
(Datum der Fakultätssitzung)

Prof. Dr. Hans-Jakob Wirz
Dekan

"Zwei Dinge sind zu unserer Arbeit nötig: unermüdliche Ausdauer und die Bereitschaft, etwas, in das man viel Zeit und Arbeit gesteckt hat, wieder wegzuwerfen."

Zitat von Albert Einstein

"Für Di ..."

Contents

Lists of Symbols & Abbreviations

Symbol	Explanation
$L_\odot$	Sun Luminosity
$M_\star$	Star Mass
$M_\odot$	Sun Mass
Ω_{bar}	Pattern Speed (bar)
Ω_G	Ascending Node Longitude
Ω_p	Pattern Speed
Ω_{sp}	Pattern Speed (spiral arms)
R_{CR}	Corotation Radius
R_{cut}	Radius to split the potential in a model
R_D	Disk scale-length
R_{GC}	1/2 of the Bar length
R_{OLR}	OLR Radius
$R_\odot$	Sun Distance to the GC
$\tau_{M.S.}$	Life time on the Main Sequence
φ_{bar}	Angle in the Galactic plane between the bar's major axis at $l > 0$ and the Sun-center line.

Abbreviation	Explanation
AU	Astronomical Unit
CR	Corotation Radius Resonance
COBE	Cosmic Background Explorer
DEC	Declination
DIRBE	Deep Infrared Background Explorer
DWT	Density Waves Theory
ESA	European Space Agency
GC	Galactic Center
HCRF	Hipparcos Celestial Reference Frame
HIC	Hipparcos Input Catalogue Number
HIP	Hipparcos Catalogue Number
HST	Hubble Space Telescope
IAU	International Astronomical Union
ICRS	The International Celestial Reference System
ILR	Inner Lindblad Resonance
LPO	Long Period Orbit
LSR	Local Standard of Rest
MC	Monte Carlo (Simulation)
MW	Milky Way
NCP	North Celestial Pole
NGC	New General Catalogue
NGP	North Galactic Pole
NIR	Near Infra-Red
OBA	OB Association
OLR	Outer Lindblad Resonance
RA	Right Ascension
$SgrA^*$	Sagittarius A^*
SCP	South Celestial Pole
SGP	South Galactic Pole
SoS	Surface of Section (Poincaré section)
SPH	Smoothed Particles Hydrodynamics
SPO	Short Period Orbit
SMBH	Super-Massiv Black Hole
TVC	Galactic Terminal Velocity Curve
VE	Vernal Equinox
wrt	with respect to
ZVC	Zero Velocity Curve

Abstract

The goal of this thesis is it to learn something about the kinematics and structure of the Milky Way. By analysing a sample of young stars in the nearby Galactic disk we can get to know more about the global large-scale structure of our host Galaxy. If we see resonance phenomena in a velocity field, then we are able to back-reference from this effect to a possible asymmetric features in the potential.

The reality of science is of course not as simple as that. There are many assumptions to make and weighted for being able to work. But step by step information can be filtered out of the entire ensemble.

In the first part of this work we relate the velocities of a sample of OB stars, to the average velocity field of the nearby areas of the Galaxy. Our analysed region covers a ± 2.2 kpc square around the Sun. A star with an orbit passing near the Sun would spend more than 12% of its time period[1], in this analysed field.

Our sample of young OB stars has complete phase space information. For kinematic analysis and to investigate the characteristics of this sample, such as its completeness-, spectral type dependence, and errors- tests are made. The completeness of our sample is particularly discussed in the view of possible kinematic biases. Different spectral type limited sub-samples are analysed, and error bars are estimated with Monte Carlo simulations.

Our aim is to understand the large-scale velocity field, thus we remove runaway stars and members of prominent OB associations out of the Gould belt, and we implement a random procedure to construct a spatially nearly homogeneous sample of OB star tracers for the young star velocity field.

The individual velocity vectors of these stars are randomly distributed with respect to the mean field in the solar neighbourhood, perhaps due to a variety of dynamical processes occurring at or after the birth of these stars. Our goal is to recover the mean velocity field by fitting a smooth velocity field to the in-plane velocities of all our sample stars. For this task we use the non-parametric smoothing algorithm and software of Wahba and Wendelberger (1980, hereafter WW-algorithm), originally developed for analyzing meteorological data. We fit a two-dimensional surface to the data points for each of the in-plane velocity components, as a function of posi-

---

[1]The average time a star needs to turn around the Galactic Center.

tion relative to the Sun, and thus derive a smoothed velocity field. For testing the WW-algorithm and adjusting a smoothing parameter, and for understanding the results of applying the algorithm to the OB star data, we analyse simulated data sets. The general idea is to draw Monte Carlo realisations from a known velocity field, so that the resulting artificial data sets closely resemble the OB star samples under investigation.

We made a number of tests to ensure that our fitted velocity field is independent of the (sub)sample used in the analysis, of the assumptions made for the Galactic parameters, and of the technical details of the fitting procedure. In particular we tested if the fitted velocity field does not depend on: (1) the size of the region around the Sun used for the fitting, (2) the rotation of the region and of the coordinate system in which the fit is made, (3) whether we use the nearly complete sample of early-type OB stars, or the full sample which has the advantage of the best space coverage but with a bad sample completeness, (4) by changing subsamples through different modulo functions, (5) by restricting the sample to lower heights ($|z| < 100$ kpc vs. $|z| < 200$ kpc), (6) by using only the half of the sample with the better distance estimates, (7) by changing the assumed rotation velocity of the LSR, and (8) by changing the assumed galactocentric solar radius.

To make these differences between our fitted velocity field and a circular field more intuitive, we convert the observed velocity field to the Galactic Center reference frame, by subtracting the solar motion in the LSR and adding the LSR rotation for an assumed position of the Sun at $R_0 = 8$ kpc. We then determine streamlines by integrating through the converted velocity field.

Deviations of the fitted field to a circular one are clearly visible. They are in the sense that the streamlines derived from the OB star velocities are more elongated than those expected from circular orbits, especially for radii $R < R_\odot$. These elongated flow-lines reach their minimum galactocentric radii at points that are located approximately on the line that connects the Sun with the Galactic Center. At $R > R_\odot$ the streamlines seem to be slightly turned forward.
This result is very robust appropriate to all the listed tests. And it inspired us to think at periodic orbit families near resonances.

Using linear perturbation theory for near-circular orbits, one finds that closed orbits in a barred potential are elongated either parallel or perpendicular to the bar. The orientation changes at each of the fundamental resonances. The situation at the OLR shows two closed orbits (in a frame of reference co-rotating with the bar) just inside and outside the Outer Lindblad Resonance (OLR). The innermost is antialigned and the outermost is aligned with the bar. Because of their ellipticity they can reach the other side of the OLR. Clearly, if all disk stars moved on closed orbits, the stellar kinematics would deviate from that of a nonbarred galaxy only

at positions very close to R_{OLR}, where the closed orbits are significantly noncircular.

By using 4 different potentials we simulate the corresponding orbit families in a rotating frame with the corresponding pattern speed of the implemented bar. The main differences between the models are the positioning of the OLR and the incorporation of an asymmetric potential represented by 4 equal spiral arms. Each model includes a symmetric potential and an asymmetric bar potential, for two models we included a halo component. In all the cases we worked with only one pattern speed.

As a first step, using the well established potential from Bissantz et al. (2003), we found orbits having the characteristic of our non-circular velocity field, but not at an expected solar region. By shifting the OLR we could provoke an intersection between the wanted orbit families and the analysed OB star field. The ellipticity of these orbits is strong, for a better result we have to shift the OLR even further out, what we plan to do. Our modeling with the arm potential included, showed that the inclination of the orbit families, as we see it in the observed field, can be reproduced by these technique.

Chapter 1

General Aspects

1.1 Galaxies

Galaxies appear on the sky as huge clouds of light, thousands of parsecs across. Each galaxy contains about 10^6 to 10^{12} stars. Bounded by gravity stars can not wander freely through space. Galaxies contain gas and dust as well but almost all the visible light is emitted by their stars, and stellar births and deaths profoundly influence the structure of galaxies.

For detailed information about properties of stars see Binney and Merrifield (1998) (Galactic Astronomy, *Chap.* 3) and Sparke and Gallagher (2000) (Galaxies in the Universe, *Chap.* 1.1)

Hubble (1926) classified galaxies into a sequence of *ellipticals*, *lenticulars* and *spirals*. There is a fourth class called the *irregulars*.

The terms "early type" and "late type" are often used to describe the position of galaxies within the subsequence. The size of a central brightness condensation (bulge), the smoothness of the visible light and arms- or bar- features are the criteria Hubble used to obtain a classification for a *galaxy morphology* called the **tuning fork** scheme, see Fig. 1.1. The additional category of *irregulars*, Fig. 1.2, allows one to deal with galaxies that do not fit within this simple scheme. In the nearby universe, the vast majority of bright galaxies can be fairly reliably fit into this system. Note that this diagram is not meant to indicate an evolutionary sequence and that the formation and evolution of galaxies is still not fully understood.

Elliptical galaxies appear smooth and structureless. They vary in their shape from round to fairly highly elongated. A galaxy of this type is designated E_n, where the number n describes the apparent axial ratio b/a by the formula $n = 10[1-(b/a)]$. Thus a galaxy which appears round on the sky is designated E_0, and one whose major axis a is twice as long as its minor axis b is an E_5 galaxy.

Elliptical galaxies contain very little dust or gas so new stars are no longer forming and therefore elliptical galaxies are rather old.

In the middle of Hubble's tuning-fork diagram, at the junction of the ellipticals
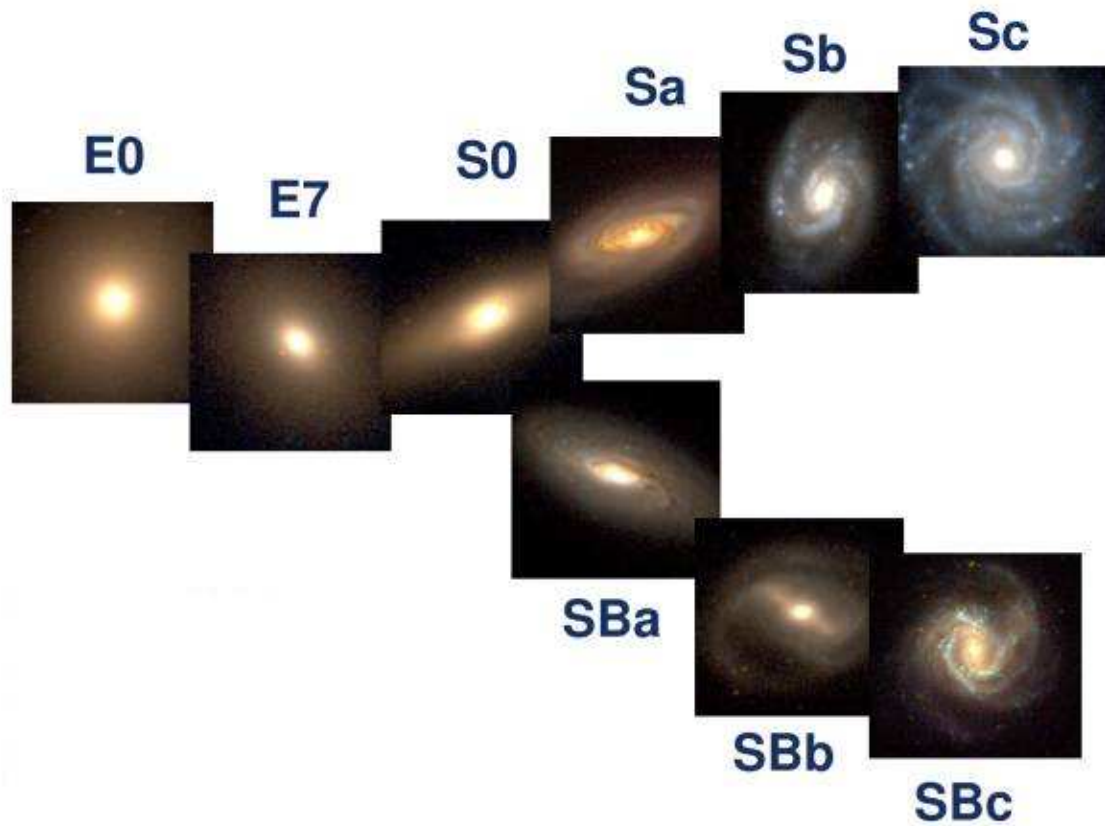
Figure 1.1: Classification of galaxies after E.P. Hubble, by using representative galaxies from the galaxy catalogue of Frei et al. (1996). At the left side there are the *ellipticals* which range from E_0 to E_7. *Lenticular galaxies SO* are placed before the tines of the fork start, the upper one consists of the *normal spirals* (Sa) while in the lower one are the *barred* (SBa) galaxies. ($www.astro.livjm.ac.uk/.../pic/cosmo/htf\_col.jpg$)

Figure 1.2: Starburst Irregular (Irr) Galaxy NGC 1313

and the spirals, comes a class of galaxies known as the **lenticulars**.

These galaxies are designated as (S0) or (SB0) according to whether or not they do have a bar structure in the center. The S0 galaxies are characterized by a smoothed central brightness condensation (the bulge or spheroidal component) similar to an elliptical galaxy, surrounded by a large region of less steeply declining brightness. This latter component, which is generally rather structureless, is believed to be intrinsically flat. They resemble ellipticals in lacking extensive gas and dust, but they share with spirals the thin and fast-rotating stellar disk.

In the Hubble sequence the lenticulars are followed by the **spiral** galaxies. A normal spiral comprises a central brightness condensation, the bulge, which resembles an elliptical, located at the center of a thin disk containing more or less conspicuous spirals of enhanced luminosity, the *spiral arms*. A barred spiral has, together with the spiral arms, a *bar*, often containing dark lanes believed to be produced by absorption of the stellar light by dust. The spiral arms of barred spirals generally emanate from the ends of the bar. Within each class of spirals, barred or not, a sequence of subtypes is identified by division according to a combination of 3 criteria:

1. The relative importance of the central luminous bulge and the outlying disk in producing the overall light distribution of the galaxy.

2. The tightness with which the spiral arms are wound.

3. The degree to which the spiral arms are resolved into stars and individual emission nebulae (HII-regions).

Early-type spirals, placed on the left side of the sequence, are those having conspicuous bulges and tightly wound, smooth arms. They are designated as Sa or SBa according to whether they are barred or not. Late-type spirals are on the right side, having smaller bulges and loosely wound, highly resolved arms. They are called Sc or SBc galaxies.

The central bulge of a spiral galaxy contains old stars similar to those found in an elliptical galaxy, but in its arms still a lot of gas and dust can be found and so new stars are continuously formed. Glowing clouds of ionized hydrogen (HII regions) and hot young stars make the spiral arms look bright and blue in photographs.

Bulges are comparable with elliptical galaxies in terms of stars moving on randomly oriented orbits. In the disk, stellar orbits are nearly circular.

Asymmetrical galaxies are assigned as **irregulars** (see Fig. 1.2), which split up into two main groups: (1) *Irr I* galaxies; objects that lack symmetry or well defined spiral arms and display bright knots that contain young and bluish stars of spectral types O and B (see Sec. 1.3.2; *Young Stars as tracers*). (2) *Irr II* galaxies; asymmetrical objects that have rather smooth images. They frequently display dust lanes.
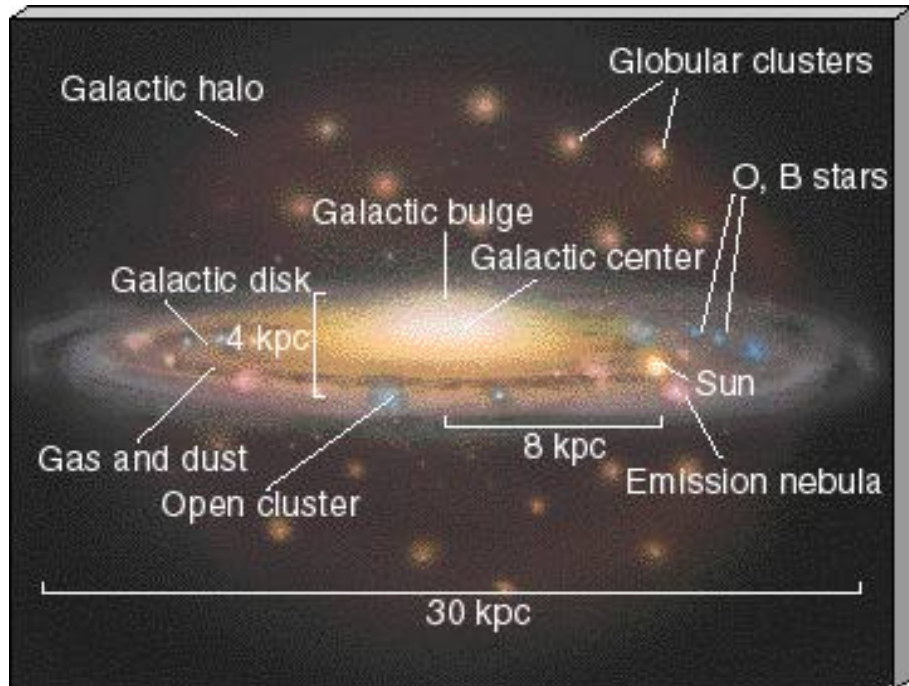
Figure 1.3: Schematic (edge-on) view of the major components of the MW's overall structure. (*www.cfa.ustc.edu.cn/.../IMAGES/AACHDGM0.JPG*)

1.2   Structure of the Milky Way

The velocity field of young stars in the solar neighbourhood is the main topic of my thesis, so it is important to have a certain knowledge about our host galaxy, the Milky Way (*MW*).

The MW's Hubble-type is *SBbc*, a large Spiral with a prominent bar (Sparke and Gallagher (2000); Cole and Weinberg (2002)). By sitting inside, the overall structure is hidden. Gaining information about it is tedious and difficult and may easily lead to misinterpretations. Actually MW is the only galaxy which can be studied in detail in three dimensions.

Classically, the stellar component of the Galaxy can be divided into four populations, namely the **halo**, the **bulge**, the **thick** and the **thin disk**. Additional structure further diverts this classification. Namely a bar shaped structure within the bulge and spiral arms within the disk. Finally the concept of a Dark Halo (or MOND) has to be introduced to explain the observed attributes of the structure.

1.2.1 Stellar Halo

Shape	
$\sim$Spherical $R \sim 100\,\mathrm{kpc}$	Sirko et al. (2004)
somewhat flattened, less than the bulge	Newberg and Yanny (2005)
Content	
Total mass $\sim 2 \times 10^9\,\mathrm{M_\odot}$	Carney et al. (1990)
Star Density $\rho(r) \propto r^{-3.5}$ for $r \lesssim 25\,\mathrm{kpc}$	Kinman et al. (1994)
Luminosity $L_V = 4 \times 10^7\,\mathrm{L_\odot}$	Binney and Merrifield (1998)
only $\sim 1\%$ of the luminous mass of the Galaxy	Christopher et al. (2005)
Metal-poor $[Fe/H] \sim -1.5\,\mathrm{dex}$	Ryan and Norris (1991)
and very old stars	Christopher et al. (2005)
little gas and dust	Wyse and Gilmore (2005)
Kinematics	
High velocity dispersions (wrt LSR)	Binney and Merrifield (1998)
$(\sigma_R, \sigma_\Phi, \sigma_z) = (135, 105, 90)\,\mathrm{km\,s^{-1}}$	
Slow rotation, (if at all) $\sim 20\,\mathrm{km\,s^{-1}}$	Sirko et al. (2004)
Peculiarities	
Tidal stream	Majewski et al. (2005)

The shape of the galactic stellar halo is almost spherical and extends to $\sim 100\,\mathrm{kpc}$ (Sirko et al., 2004). Compared to its huge size its mass is rather small, with $\sim 2 \times 10^9\,\mathrm{M_\odot}$ (Carney et al., 1990), seen in relation to the total galactic mass of $1.5 - 4.0 \times 10^{12}\,\mathrm{M_\odot}$ (Beers et al., 2004). Kinman et al. (1994) determine the halo star density up to $r \lesssim 25\,\mathrm{kpc}$ to be a $\rho(r) \propto r^{-3.5}$ relation.

There are two main building blocks of the halo: the "globular cluster[1] "- and the "field star"-system. The field star halo is nearly 2 orders of magnitude more luminous then the globular system. Globular clusters, there are just a few hundred of them in the MW, start to be seldom outside $\sim 25\,\mathrm{kpc}$ but field stars can rise up to $\sim 100\,\mathrm{kpc}$ (Binney and Merrifield, 1998).

Another important splitting is the distinction between objects close to the disk and the ones at large height above the plane. Armandroff (1989b),(1989a) analysed globular clusters, by comparing a "halo" and a "disk" sample. He found $[\sigma_{los,halo} = 116 \pm 11\,\mathrm{km\,s^{-1}}, v_{rot,halo} = 43 \pm 29\,\mathrm{km\,s^{-1}}]$ and $[\sigma_{los,disk} = 59 \pm 14\,\mathrm{km\,s^{-1}}, v_{rot,disk} = 193 \pm 29\,\mathrm{km\,s^{-1}}]$. This shows, that the "halo" candidates are much more dominated by a random motion, while the "disk" subsystem rotates rapidly. Sirko et al. (2004) showed that their halo rotation analysis of $v_{rot,halo} \sim 20\,\mathrm{km\,s^{-1}}$ is marginally consistent with zero at the 1σ level.

Armandroff's metallicity studies reason a wide range in the two components: $[Fe/H]_{halo}$ can go down to $-2.6\,\mathrm{dex}$ and $[Fe/H]_{disk}$ stays around $\sim -0.5\,\mathrm{dex}$. The mean metal-

---

[1]Globular clusters can contain up to several thousand of stars bound together by their mutual gravitational attraction. As an example ωCentauri contains about a million stars and its core radius is only $4\,\mathrm{pc}$. Globular clusters are the oldest objects in the Galaxy.

licity of the stellar halo is $[Fe/H] \sim -1.5$ dex (Carney et al., 1990), low compared to that of the solar neighbourhood value $[Fe/H] \sim -0.2$ dex (Nordström et al., 2004).

Substructures and Stellar Streams

The halo stellar density is sufficiently low that its stars must have formed in higher density systems and have dispersed later. The field stellar halo could rather naturally be formed from the debris of stellar clusters, with on-going mass-loss (Odenkirchen et al., 2003, Pal 5). Ibata et al. (1994)'s work, of the Sagittarius dwarf galaxy which is in the process of being tidally disrupted by the gravitational field of the MW, assists the idea of hierarchical-clustering theories of structure formation (Silk and Wyse, 1993). Analysis of merger interactions are done by Majewski et al. (2005), for a better understanding of halo formation processes in general and the formation of our Galaxy in particular. Newberg and Yanny (2005) could measure from such streams a slight flattening of the halo.

Substructure in the disk has also been noted since the early days of galactic structure research (Eggen, 1998) and has usually been interpreted as signature of the gradual dissolution of loosely bound star clusters in the clumpy potential of the disk. Extra galactic origins for subsamples, where ages and chemical composition of stars do not match with their environment, could be an explanation (Navarro et al., 2004). The role of tidal forces in the formation of the galactic components is not yet fully
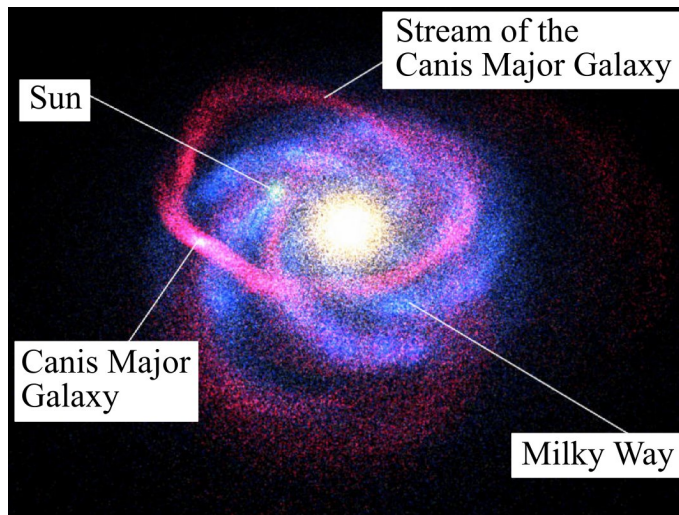
Figure 1.4: The tidal forces of the Milky Way slowly pull apart the Canis Major dwarf galaxy (shown here in red). The stars ripped off in this fashion, surround the galaxy in a vast ring. Image: (Martin et al., 2004, Observatoire de Strasbourg).

understood, but there is a strong evidence that the Canis Major dwarf galaxy is one of the building blocks of the Galaxy (Martin et al., 2004, see Fig. 1.4) like other galactic mergers as well.

1.2.2 Bulge

Shape	
"boxy" axis ratio (1:[0.3-0.6]:[0.22-0.4])	López-Corredoira et al. (2005)
Content	
Dominated by old ($\gtrsim 10\,\mathrm{Gyr}$) and metal-rich ($[Fe/H] \sim -0.3\,\mathrm{dex}$) stars	Wyse and Gilmore (2005)
Recent star formation in the inner region ($R < 500\,\mathrm{pc}$) indicated by massive stars	Genzel et al. (1994)
Kinematics	
Velocity dispersion $\sigma_{los} \sim 110 \pm 10\,\mathrm{km\,s^{-1}}$	Binney and Merrifield (1998)
Significant rotational velocity ($< v_{los} > = 66 \pm 5\,\mathrm{km\,s^{-1}}$)	Minniti et al. (1995)
Peculiarities	
Star formation in the inner Nucleus	Wyse and Gilmore (2005)

The morphology of the MW's bulge is "boxy" (López-Corredoira et al., 2005). With near-infrared images Dwek et al. (1995) traced that its bar-shaped structure points with its near end in the first galactic quadrant. Its photometrically defined mass is around $1.3 \times 10^{10}\,\mathrm{M_\odot}$ and the bulge has a luminosity measured in the direction of Baade's window[2] of about $5.3 \times 10^{9}\,\mathrm{L_\odot}$.

The central $\sim 150\,\mathrm{pc}$ of the galactic bulge is a gas-rich region which is actively forming stars; it harbors at least $10^{8}\,\mathrm{M_\odot}$ of molecular gas (Sparke and Gallagher, 2000). At the heart of the Galaxy, a torus of hot dense molecular clouds, about $7\,\mathrm{pc}$ in radius, partially surrounds the innermost cluster, which lies almost on top of the MW 's central radio source, Sagittarius A^* ($SgrA^*$). $SgrA^*$ lies within a stellar nucleus, an extraordinary concentration of stars. In mass and size the nuclear star cluster is similar to a massive globular cluster, but there is still an ongoing star formation fed by gas that flows into it. This compact object at the center of the nucleus is probably a super massive black hole ($SMBH$), with a mass $\lesssim 4 \times 10^{6}\,\mathrm{M_\odot}$ and a Schwarzschild radius of only $\sim 1 - 2\,\mathrm{AU}$ (Shen et al., 2005).

Stellar population studies of the bulge help to understand its structure and its formation scenario. Krabbe et al. (1995) and Blum et al. (1996) claim that there have been multiple epochs of star formation in the central few parsecs of the Galaxy. The most recent epoch was less than $10\,\mathrm{Myr}$ ago and others happened more than about $400\,\mathrm{Myr}$ in the past. van Loon et al. (2003) also detected a young population in the plane near the galactic center, but this discovery is affected by the fact that the scale-height of the thin disk is comparable to that of the central bulge, so that

---

[2]The distribution of dust is highly non-uniform, in the direction of *Baade's window* at $(l, b) = (1, -3.9)^\circ$ the extinction varies in a range of $1.26 < A_v < 2.79$ (Stanek, 1996) and so it is possible to see much further into the Galaxy along this line of sight.

membership in either component is ambiguous.

Finally we can say, that the outer region of the bulge is dominated by old, metal-rich stars (Wyse and Gilmore, 2005), while in the inner nucleus there is a still ongoing star formation at a rate of $\gtrsim 10 \, \mathrm{M}_\odot \, \mathrm{yr}^{-1}$ (Wyse and Gilmore, 2005).

1.2.3 Disk

The disk is the most prominent feature in the MW. As its name implies, it is flat and roughly circular, a plane full of stars, gas and dust. It can be divided into two substructures, a "thin" and a "thick" disk. Both intersect the bulge and as the names indicate the thin disk lies inside the thick disk. The outer part of the disk seems to have a warp, it starts somewhere around the solar circle, and the Sun happens to lie near one of its nodelines (Binney (1992); Smart and Lattanzi (1996)). Bulge and disk are rotating in the same direction. The stars in the disk orbit the GC at about $\sim 200 \, \mathrm{km \, s}^{-1}$ on nearly circular paths.

The disk's stellar mass is around $6 \times 10^{10} \, \mathrm{M}_\odot$ and its luminosity is between $1.5 - 2.0 \times 10^{10} \, \mathrm{L}_\odot$ (Sparke and Gallagher, 2000). But most (95%) of the stars are members of the thin disk, especially all young massive stars (Sparke and Gallagher, 2000). The gas and dust, which are needed for new star formations lie in an even thinner layer than the stars itself. In the solar region this layer's height is around $\sim \pm 100 \, \mathrm{pc}$. The thickness of the gas layer increases in proportion to the galactocentric radius. Gas is also found near ongoing star formation sites as well as near the locations of spiral arms and the bar.

Thin Disk

Shape	
Scale height: $\sim 300 \, \mathrm{pc}$	Fuhrmann (2004)
Scale length: $\sim 3 \, \mathrm{kpc}$	Fuhrmann (2004)
Content	
Mass $\sim 5 \times 10^{10} \, \mathrm{M}_\odot$	Sparke and Gallagher (2000)
95% of all disk stars	Sparke and Gallagher (2000)
All young massive stars	
Both young and old stars; gas and dust	
$\rightarrow$ Site of ongoing star formations	
Metallicity $[Fe/H] \sim -0.2 \, \mathrm{dex}$	Wyse and Gilmore (2005)
Kinematics	
Velocity dispersions $(\sigma_R, \sigma_\Phi, \sigma_z) = (34, 21, 18) \, \mathrm{km \, s}^{-1}$ Gas and stars move on near circular orbits	Binney and Merrifield (1998)
Peculiarities	
Hosts spiral arms and a bar	

Thick Disk

Shape	
Scale height: $600 - 1500\,\mathrm{pc}$	Fuhrmann (2004)
Scale length: $\sim 4\,\mathrm{kpc}$	Fuhrmann (2004)
Content	
Mass $\sim 10^{10}\,\mathrm{M_\odot}$	Wyse and Gilmore (2005)
$10 - 20\%$ of the thin disk mass	
Old stars ($\sim 10 - 12\,\mathrm{Gyr}$)	Nordström et al. (2004)
Metallicity $[Fe/H] \sim -0.6\,\mathrm{dex}$	Wyse and Gilmore (2005)
Poorer in heavy elements than	Sparke and Gallagher (2000)
the thin disk stars	
Kinematics	
Velocity dispersions	Binney and Merrifield (1998)
$(\sigma_R, \sigma_\Phi, \sigma_z) = (61, 58, 39)\,\mathrm{km\,s^{-1}}$	
Gas and stars move on near circular orbits	
Peculiarities	
Hosts the thin disk	
Warped structure	Sparke and Gallagher (2000)

It is not yet clear how the "thin" and the "thick" disks got formed. One picture predicts a heating-mechanism which blows a thin disk up to a thick disk. But "normal" disk heating mechanisms like transient gravitational perturbations in the disk produce vertical velocity dispersion values in the range of $\sigma_W \sim 20\,\mathrm{km\,s^{-1}}$. But the kinematics of the thick disk are intermediate between the halo and the thin disk with a azimuthal streaming velocity $v_{rot} \lesssim 170\,\mathrm{km\,s^{-1}}$ (Wyse and Gilmore, 2005) and a fairly high velocity dispersion of $\sigma_W \sim 40\,\mathrm{km\,s^{-1}}, \sigma_{total} \sim 80\,\mathrm{km\,s^{-1}}$ which is twice the predicted value.

The old age of $\sim 10-12\,\mathrm{Gyr}$ (Nordström et al., 2004) for the thick disk indicates that star formation has not happened in the recent past. Not so in the thin disk where star formation is still ongoing. Additionally the pattern of elemental abundances differs between the thick and thin disks (Fuhrmann, 2004). This implies distinct star formation and enrichment histories for the thick and thin disk.

Fuhrmann (2004) reasons that the origin of the thick disk cannot be a merger, because if it is as massive as it comes out from his work then there is nothing "to merge with" at this look-back time. Merging scenarios (Abadi et al., 2003) can explain many observations but not the full mechanism. Fuhrmann implies that the Galaxy formed 13 or 14 Gyr ago with the implementation of a massive, rotationally-supported population of thick disk stars. The very high star formation rate in that phase gave rise to a rapid metal enrichment and an expulsion of gas in supernovae-driven galactic winds, but was followed by a star formation gap for no less than $3 - 5\,\mathrm{Gyr}$ at the Sun's galactocentric distance. In a second phase, then, the thin disk came on stage.

1.2.4   Bar

Bars in general are a very common feature, found in over half of all spiral galaxies (Whyte et al., 2002). Since some years, it has been established that the MW is *barred* as well (Gerhard, 2002). Its bar is a triaxial structure, hosted in the middle of the disk, with a probable age of less than 3 Gyr (Cole and Weinberg, 2002). A 3.4 kpc long cigar, inclined wrt the "Sun-GC" line by $\sim 20°$ can be given as a first guesstimate.

The large non circular motion of HI and CO observations, NIR light distributions, source count asymmetries, gas kinematics, and large microlensing optical depth studies are used for a better understanding of this substructure. Parameters like the **orientation**, the **shape** and the **pattern speed** define the bar.

A summary of publications, methods, main results, and bar characteristics are composed in Tab. 1.1.

Evidences for an Asymmetric Feature (Bar?)

The best clues to the existence of a bar in an edge-on system come from the kinematics of its gaseous components, where the non-axisymmetric bar potential induces non-circular orbits in the gas.
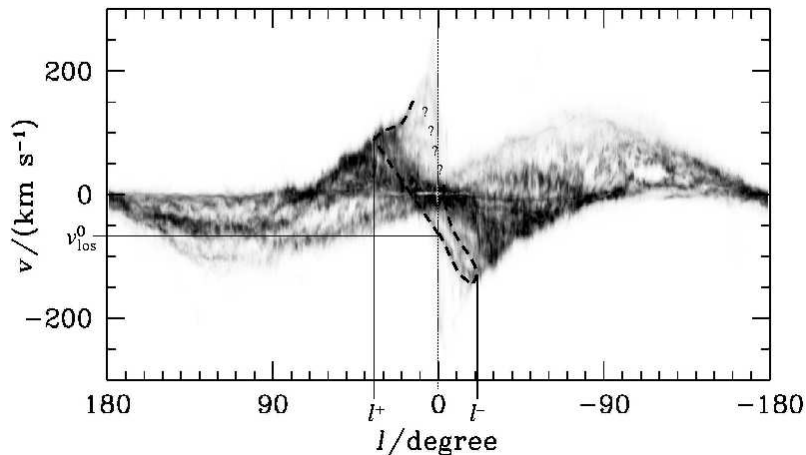

Figure 1.5: Plot showing the distribution of atomic hydrogen in the plane of the Milky Way as a function of galactic longitude and line-of-sight velocity, as indicated by its 21 cm emission. The 3 *kpc arm* is shown by the dashed line, along with its important measurable parameters; the part of the feature that is too faint to trace reliably is indicated by question marks. (Adapted from Binney and Merrifield (1998))

Fig. 1.5, the so called *l-v diagram* of the MW, shows the line-of-sight velocity versus galactic longitude in the plane of the Galaxy. It reveals a clear signature of a non-axisymmetric distribution. There is a significant asymmetry between the

data	φ_{bar} $^\circ$	length R_{GC} kpc	axis ratio	scale length R_D kpc	publication
starcounts	12 ± 6		$10 : 5.4 : 3.3$	3.0	López-Corredoira 2000
	$20 - 30$				Nikolaev 1997
	$20 - 30$		$10 : 4 : 3$		Stanek 1997
				2.5	Ortiz 1993
	44 ± 10	4.4; $R_\odot = 8.5$			Benjamin 2005
integrated light	$15 - 35$				
combined	$20 - 25$ 25% error	$3.1 - 3.5$	$10 : 3 - 4 : 3$	2.1	Bissantz 2002
		$3.1 - 3.5$	$10 : 6 : 4$	2.5	Binney 1997a
star formation region		$3.1 - 3.5$	$10 : 3 - 4 : 3$	3.5	Hammersley 2000
microlensing	15				Zhao 1996
good accepted value	20	$3.1 - 3.5$	$10 : 4 : 3$		

method	R_{CR} kpc	Ω_p $\mathrm{km\,s^{-1}\,kpc^{-1}}$	3kpc arm	special properties	
hydrodynamical simulation	$3 - 4.5$		inside R_{CR}		Englmaier 1999
	$3 - 4.5$		"		Fux 1999
	5.0	42		$\varphi_{bar} = 34\,\mathrm{deg}$	Weiner 1999
	3.4 ± 0.3	60 ± 5		$\Omega_{sp} \sim 20$	Bissantz 2003
orbital resonances	4.4 ± 0.4	51 ± 4		quadrupole moment strong enough?	Dehnen 2000
direct method		59 ± 15		OH/IR arm-bar ?	Debattista 2002
good accepted value	4 ± 0.5				

Table 1.1: Summary of the main bar and disk parameters represented in a table, see Gerhard (2002) *The Galactic Bar*. Ω_p pattern speed (bar); Ω_{sp} pattern speed (spiral arms); R_{CR} corotation radius; R_D disk scale-length; R_{GC} bar length; φ_{bar} angle in the galactic plane between the bar's major axis at $l > 0$ and the Sun-center line. (Because of space-saving in this Table the publications are exceptionally given by the first author's name only and the date of the publication.)

gas properties at positive and negative longitudes, which is inconsistent with an axisymmetric disk. Further evidence for non-circular motions come from the non-zero line-of-sight velocities of some of the HI gas at zero longitude: if the gas were following circular orbits, then all of its motion should be transverse to the line of sight at this point. The strongest feature that illustrates these properties is classically known as the 3 *kpc arm* (see Fig. 1.8) because of its approximate radial location in the Galaxy. This feature, highlighted in Fig. 1.5, is asymmetric about the center of the Galaxy, lying between galactic longitudes of $l^- \sim -20°$ and $l^+ \sim +35°$. Tracing it through the center of the Galaxy reveals that it crosses zero longitude at a velocity of $v_{los}^0 = -53 \, \text{km s}^{-1}$; presumably this loop in the *l-v diagram* recrosses $l = 0$ at positive velocity, but this part of the feature is too faint to be traced reliably. It was this observation that led to the idea that the feature might be an expanding arm of material thrown out from the center of the Galaxy in our direction.

1.2.5 Spiral Arms

Vallée (2005) published his third, updated statistical study about MW *spiral arms*. A summarizing Table with the main publications and characteristics out of the analysed working period (1980 to early 2005) is printed in the Appendix, see Tab. A.1. Tab. 1.2 lists the trends in MW-modelling and their enhancement in the last few years analysed by Vallée's study.

The early pioneer of studies on the formation of the spiral arms was Bertil Lind-

Publication year		1987	1998	2002	2004	Trend
% of publications which used ...						
"4 arm" Study		65	84	83	85	↗
"log arm" Study		93	81	82	92	88
Mean value used in published papers						
"Pitch Angle" Study	*deg*	-12.7	-12.0	-11.0	-12.6	-12.1
"Inter arm distance" Perseus and Sagittarius Study	kpc	3.7	3.45	3.6	2.75	3.4

Table 1.2: Summary analysis of 4 MW trends: Most MW-models include ("4 arms") and logarithmic formed spirals ("log arm"). The ("Pitch Angle") represents the arm's winding degree, the distance between arms ("Inter arm distance") is of main interest as well.

blad. He realized that the idea of stars arranged permanently in a spiral shape was untenable due to the *winding dilemma*. Since the rotation speed of the galactic disk
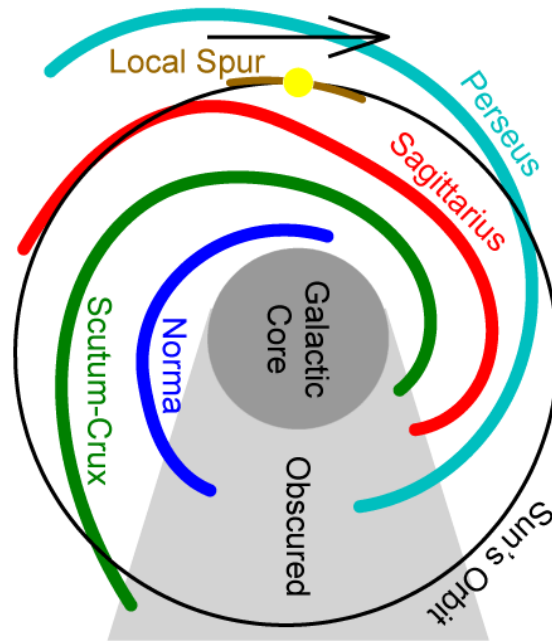
Figure 1.6: Observed spiral structure of the MW following Taylor and Cordes (1993). The arrow points the direction of the solar system's motion relative to the spiral arms.

varies with distance from the center of the galaxy, a radial arm (like a spoke) would quickly become curved as the galaxy rotates. The arm would, after a few galactic rotations, become increasingly curved and wind around the galaxy ever tighter.

The first acceptable theory was devised by Lin and Shu (1964), the **Density Wave Theory** (DWT). They suggested that the spiral arms were manifestations of spiral density waves. A "stellar traffic jam" where stars are packed more densely. The DWT of spiral structure is based on the premise that mutual gravitational attraction of stars and gas clouds at different radii can offset the kinematic spiral's tendency to wind up, and will cause a pattern to grow which rotates rigidly with a single pattern speed.

Alternative hypotheses that have been proposed involve waves of star formation moving about the galaxy; the bright stars produced by the star formation die out quickly, leaving darker regions behind the waves, and hence making the waves visible.

Figure 1.6 shows a diagram of the observed MW spiral structure (Taylor and Cordes, 1993). The arm's names, the position of the Sun and the rotation direction of the Sun's orbit are shown. The gray shadow in the plot represents the obscured region, where observations from our solar position are difficult or even impossible due to its hidden position behind the dense galactic core.

13

1.2.6 Dark Halo or MOND?

The existence of a *dark halo* is inferred from its gravitational pull on the visible matter. Its composition is unknown, since this matter does not consist of luminous stars.

For almost twenty years models of the Galaxy have included such mass, responsible for supporting a substantial fraction of the local rotation velocity and a flat rotation curve at large distances. There is a tremendous amount of evidence for such assumptions, based on the assumption that the Newtonian theory can safely be extrapolated from the solar system (where it is well tested) to the scales of galaxies. There exists another theory which explains the discrepancy between visible matter, high velocities and Newtonian theory. In 1983, Milgrom hypothesized a specific change in the equations governing particle motions at very low accelerations. He called this the modified Newtonian dynamics, or **MOND**, therefore e.g.:.

(*http* : *//www.astro.umd.edu/ ssm/mond/astronow.html*) MOND reduces to the usual Newtonian form in the regime of high acceleration, but at accelerations lower than 1 part in 10^{11} of what we feel here on earth, things change in a way that might account for the mass discrepancy. Fits to the observed rotation curves of galaxies have now been performed for over 100 galaxies, with comparable results. While there is certainly the occasional puzzle, there are no known cases where MOND clearly fails. However, in many other systems the picture is less clear. Any modification of dynamical laws must explain the mass discrepancy everywhere. The model has to explain not only rotation curves, but also the velocity dispersions of spheroidal galaxies, the gas temperatures of clusters of galaxies, and the peculiar motions of galaxies in the large scale structure of the universe.

1.3 Solar Neighbourhood

In the outer part of our Galaxy, where our Sun is located at, most of the visible stars lie in a flattened, nearly axisymmetric disk.

Stars and gas travel around the galactic center (GC) under the force of gravity. Stars are much denser than the interstellar gas through which they move. Neither gas pressure nor the forces from embedded magnetic fields can deflect them from their paths. If one knows how the mass is distributed, one find the the resulting gravitational force and the time dependent positions and velocities of stars and galaxies can be calculated. This can be inverted by taking the stellar motions to deduce the distribution of mass. Newton's equation of motion Eq. 1.3 and the Poisson equation Eq. 1.1 describe these correlations.

$$\nabla^2 \Phi = 4\pi G \rho. \tag{1.1}$$

In disk galaxies many stars, at a certain distance from the GC, move on nearly circular orbits. Effects produced by arms and bars strongly depend on their masses and location wrt the stellar orbit. Axisymmetric approximation is valid only when

the gravitational strengths of the bar and the spiral arms are weak in comparison to the influence all other axisymmetric mass distributions. Orbits of stars in the solar neighbourhood act as good candidates for such an approximation done by the **epicycle theory**.

1.3.1 The Classical Approach: Epicycle Theory

Orbits in Axisymmetric Potentials

Stars in a galaxy do not collide like molecules[3] in a box. If the density of stars is uniform, then a star will be attracted in all directions by the same gravitational force, resulting in a vanishing net force. Consequently the force on any star in an "almost" uniform system will not vary rapidly and each star in the galaxy may be supposed to accelerate smoothly by the force field that is generated by the galaxy as a whole. Additionally galaxies typically have $\sim 10^{11}$ stars and are a few hundred crossing times (typical time for a star to cross the galaxy) old, for such systems stellar encounters are entirely unimportant. So in the case of a galaxy like the MW, the gravitational dynamics are those of a collisionless system in which the constituent stars move under the influence of the mean potential generated by all the other stars within the galaxy. The orbits of stars depend almost entirely on the smooth part of the gravitational field, averaged over a region containing many stars. Often, the mean field potential has some symmetries which simplify the orbit calculations. Here we look at the orbits of stars in an axisymmetric galaxy. Non-axisymmetric structures like the bar, the spiral arms or local features will be neglected. Still we are able to investigate the general aspects of an underlying smoothed out velocity field we are looking for. The orbits in such a model are nearly but not quite circular and lie in the same plane.

In the galactocentric cylindrical polar coordinates (R, ϕ, z) the midplane or the disk is at $z = 0$ and the center at $R = 0$. Because of the axisymmetric assumption the gravitational smoothed potential $\Phi(R, \phi, z)$ is independent of ϕ, thus $\partial\Phi/\partial\phi = 0$.

The study of orbits in such an axisymmetric galaxy can be reduced to a two-dimensional problem by exploiting the conservation of angular momentum of any star

$$\frac{d}{dt}(R^2\dot{\phi}) = 0. \tag{1.2}$$

The general equation of motion of a star is, in a conservative force field, given by

$$M\frac{d^2\vec{r}}{dt^2} = -\nabla\Phi(R, z). \tag{1.3}$$

were $\vec{r} = R\hat{e}_R + \phi\hat{e}_\phi + z\hat{e}_z$ represents the position of the object, t the time and $\nabla\Phi = \frac{\partial\Phi}{\partial R}\hat{e}_R + \frac{\partial\Phi}{\partial z}\hat{e}_z$ the force. $\hat{e}_R$, $\hat{e}_\phi$ and $\hat{e}_z$ are the unit vectors, while from now on

---

[3]No low pressure gas.

the mass M will be set to unity.

The acceleration transformed to cylindrical coordinates looks like

$$\ddot{R} - R\dot{\phi}^2 = -\frac{\partial \Phi}{\partial R}, \tag{1.4}$$

$$\ddot{z} = -\frac{\partial \Phi}{\partial z}. \tag{1.5}$$

These equations describe the coupled oscillations of the star in the $R-$ and $z-$ directions. The potential can be expressed in terms of an **effective potential** and the rotational energy of the system; L_z is the angular momentum.

$$\Phi_{eff} \equiv \Phi(R, z) + \frac{L_z^2}{2R^2} \tag{1.6}$$

and so the equations (1.4) and (1.5) can be transformed into

$$\ddot{R} = -\frac{\partial \Phi_{eff}}{\partial R}, \tag{1.7}$$

$$\ddot{z} = -\frac{\partial \Phi_{eff}}{\partial z} \tag{1.8}$$

to describe the evolution of R and z.

Thus the three-dimensional motion of a star in an axisymmetric potential $\Phi(R, z)$ can be reduced to the motion of the star in a plane. This (non-uniformly) rotating plane with cylindric coordinates (R, z) is often called the **meridional plane**.

Stable orbitals arise only when the net force vanishes, hence looking at extrema of the potential, we find

$$0 = \frac{\partial \Phi_{eff}}{\partial R} = \frac{\partial \Phi}{\partial R} - \frac{L_z^2}{R^3} \tag{1.9}$$

$$0 = \frac{\partial \Phi_{eff}}{\partial z}. \tag{1.10}$$

If Φ_{eff} is symmetric about $z = 0$ then Eq. 1.10 is satisfied anywhere in the equational plane $z = 0$, and Eq. 1.9 at a certain radius R_g, where

$$\left(\frac{\partial \Phi}{\partial R}\right)_{(R_g, 0)} = \frac{L_z^2}{R_g^3} \equiv R_g \dot{\phi}^2 \tag{1.11}$$

is given. This represents the condition for a circular orbit with angular velocity $\Omega = \dot{\phi}$.

In the disk, many stars are on nearly circular orbits, so it is useful to derive approximate solutions to equations which are describing them. x is the stars deviation from its **guiding center** R_g (see Fig. 1.7).

$$x \equiv (R - R_g)\hat{e}_R \tag{1.12}$$

Thus $(x, z) = (0, 0)$ represents the coordinates of a minimum in the meridional plane Φ_{eff}. At these positions circles with radius R_g occur. When we expand Φ_{eff} in a Taylor series about this point R_g, we obtain

$$\Phi_{eff} = \frac{1}{2}\left(\frac{\partial^2\Phi_{eff}}{\partial R^2}\right)_{(R_g,0)} x^2 + \frac{1}{2}\left(\frac{\partial^2\Phi_{eff}}{\partial z^2}\right)_{(R_g,0)} z^2 + \text{``higher order terms''}. \quad (1.13)$$

The terms proportional to x, z vanish because Φ_{eff} is symmetric about $z = 0$. Then the equations of motion (1.7) and (1.8) are reduced to the **epicycle approximation**.

$$\ddot{x} = -\kappa^2 x, \quad (1.14)$$
$$\ddot{z} = -\nu^2 z \quad (1.15)$$

with

$$\kappa^2 \equiv \left(\frac{\partial^2\Phi_{eff}}{\partial R^2}\right)_{(R_g,0)}, \quad (1.16)$$

$$\nu^2 \equiv \left(\frac{\partial^2\Phi_{eff}}{\partial z^2}\right)_{(R_g,0)}. \quad (1.17)$$

According to these equations, x and z evolve like the displacements of two harmonic oscillators with the frequencies κ and ν. They are called the **epicycle** and the **vertical** frequencies, respectively.

The relation between the frequency of the epicycle κ and the one of the underlying circular orbit Ω can be seen from the effective potential as mentioned in Eq. 1.6, then

$$\kappa^2 = \left(\frac{\partial^2\Phi}{\partial R^2}\right)_{(R_g,0)} + \frac{3L_z^2}{R_g^4}, \quad (1.18)$$

$$\nu^2 = \left(\frac{\partial^2\Phi}{\partial z^2}\right)_{(R_g,0)}. \quad (1.19)$$

Ω can be written as

$$\Omega^2(R) = \frac{1}{R}\left(\frac{\partial\Phi}{\partial R}\right)_{(R,0)} = \frac{L_z^2}{R^4} \quad (1.20)$$

and so the relation between κ and Ω is

$$\kappa^2 = \left(R\frac{d\Omega^2}{dR} + 4\Omega^2\right)_{R_g}. \quad (1.21)$$

The *Point mass* ($\kappa = \Omega$) and the *Solid body* ($\kappa = 2\Omega$) model are representing the extrema of possibilities, thus the limiting cases for κ-values are given by

$$\Omega \leq \kappa \leq 2\Omega. \quad (1.22)$$

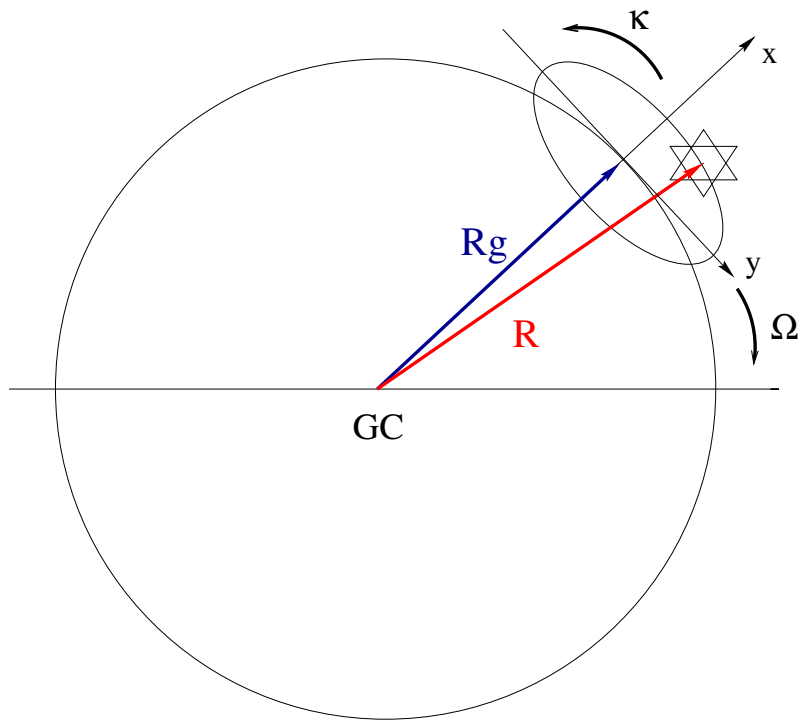Some special characteristics of models are listed in Tab. 1.3.

Figure 1.7: Geometry and description of a Monte Carlo (MC) model background and the definition of the coordinate system. The movement of a star is well approximated by the superposition of a retrograde motion at angular frequency κ around a small ellipse with axis A_x and A_y, and a prograde motion of the ellipse's center, called *Guiding Center* at angular frequency Ω around a circle with radius R_g. Individual epicycles are elongated in the azimuthal direction, but the velocity ellipsoid is elongated in the radial direction.

$\kappa = \Omega$	$v \propto \sqrt{\frac{1}{R}}$	$\Omega \propto R^{\frac{-3}{2}}$	$\frac{A_x}{A_y} = \frac{1}{2}$	Point mass Keplerian Potential
$\kappa = \sqrt{2}\Omega$	$v \propto cte.$	$\Omega \propto \frac{1}{R}$	$\frac{A_x}{A_y} = \frac{1}{\sqrt{2}}$	Halo-Model Isothermal
$\kappa = 2\Omega$	$v = R$	$\Omega \propto const.$	$\frac{A_x}{A_y} = 1$	Solid body Harmonic oscillator

Table 1.3: Special cases

General Solutions for the Equations of Motion

The equations of motion (Eq. 1.14 and 1.15) lead to two integrals, namely the energies

$$E_R \equiv \frac{1}{2}(\dot{x}^2 + \kappa^2 x^2) \tag{1.23}$$

$$E_z \equiv \frac{1}{2}(\dot{z}^2 + \nu^2 z^2) \tag{1.24}$$

of such a star. While the total energy is

$$E_{tot} = E_R + E_z + \Phi_{eff}(R_g, z). \tag{1.25}$$

General solutions for the equations of motion are given by

$$x(t) = A_x \cos(\kappa t + \psi) \tag{1.26}$$
$$z(t) = A_z \cos(\nu t + \varsigma), \tag{1.27}$$

where A_x, A_z and ψ, ς are given by the boundary condition of the specific problem.

Next, since $\Omega_g = \frac{L_z}{R_g^2}$ is the angular velocity of the circular orbit with conserved angular momentum L_z, and L_z is conserved, we obtain

$$\dot{\phi} = \frac{L_z}{R^2} = \frac{L_z}{R_g^2}\left(1 + \frac{x}{R_g}\right)^{-2} \tag{1.28}$$

$$\simeq \Omega_g\left(1 - \frac{2x}{R_g}\right). \tag{1.29}$$

Substituting x from Eq. 1.26 and integrating, we obtain

$$\phi = \Omega_g t + \phi_0 - \frac{2\Omega_g A_x}{\kappa R_g}\sin(\kappa t + \psi). \tag{1.30}$$

The nature of the motion described by these equations can be clarified by taking Cartesian coordinates (x, y, z) in a rotating frame with origin at the guiding center $R = R_g, \Phi = \Omega_g t + \Phi_0$. The x and z coordinates have already been defined, and the y coordinate is perpendicular to both. To a first order it will be

$$y(t) \quad \sim \quad -\frac{2\Omega_g}{\kappa} A_x \sin\left(\kappa t + \psi\right) \tag{1.31}$$

$$= \quad -A_y \sin\left(\kappa t + \psi\right) \tag{1.32}$$

Eq. 1.26 and Eq. 1.31 are the complete solution for the orbit in the epicycle approximation. The motion in the z-direction is independent of the motion in x and y. In the (x, y) plane a star moves on an ellipse called the **epicycle** around the guiding center. The lengths of the semi-axes of the epicycle are in the ratio

$$\frac{A_x}{A_y} = \frac{\kappa}{2\Omega_g}. \tag{1.33}$$

1.3.2 The Local Disk

Properties and Position of the Sun

On account of its rotation, chemistry, and age ($\sim 4.5\,\mathrm{Gyr}$) we know that the Sun is very typical among its G-type neighbours (Fuhrmann, 2004) (see Sec. 1.3.2; *Young Stars as tracers*).

Its mass $\mathrm{M}_\odot$, as determined from the orbit of Earth and other planets, is $\sim 2 \times 10^{30}\,\mathrm{kg}$. To set it in a context with other stars: their range covers $0.075\,\mathrm{M}_\odot$ to $120\,\mathrm{M}_\odot$. The Sun's luminosity $\mathrm{L}_\odot$ is $3.86 \times 10^{26}W = 4.83\,\mathrm{mag}$. Stars differ enormously in this value: the brightest are over a million times more luminous than the Sun, while stars as faint as $10^{-4}\,\mathrm{L}_\odot$ have been already observed as well. The Sun's radius ($\mathrm{R}_\odot$) is around $6.96 \times 10^5\,\mathrm{km}$; estimated range of stellar radii varies from $0.1 \times \mathrm{R}_\odot$ to $1000 \times \mathrm{R}_\odot$.

The Sun does not lie exactly in the galactic midplane, but is located $10 - 20\,\mathrm{pc}$ above it, and its path around the galactic center is not precisely circular. The **Local Standard of Rest** (LSR) is defined as the average motion of stars near the Sun. Relative to this average the Sun is moving with velocities referred as solar **peculiar velocities**: $u_\odot$ points to the GC, $v_\odot$ in the direction of the galactic rotation and $w_\odot$ up toward the NGP (north galactic pole). (Dehnen, 1998, derived out of Hipparcos data)

$$u_\odot \quad = \quad 10.0 \pm 0.4 \ \ \mathrm{km\,s^{-1}} \tag{1.34}$$

$$v_\odot \quad = \quad 5.2 \pm 0.6 \ \ \mathrm{km\,s^{-1}} \tag{1.35}$$

$$w_\odot \quad = \quad 7.2 \pm 0.4 \ \ \mathrm{km\,s^{-1}}. \tag{1.36}$$

Often it is assumed, that the LSR follows a circular orbit around the GC, at a solar radius $\mathrm{R}_\odot \sim 8\,\mathrm{kpc}$ and a velocity of $\mathrm{V}_\odot \sim 220\,\mathrm{km\,s^{-1}}$. Thus the Sun takes roughly

230 Myr to complete one revolution around the GC.

The Sun lies within a giant star-and-gas complex that is known as the Gould's Belt (see Sec. 1.3.2; *Substructures near the Sun*) with a radius of ~ 500 pc and a lifetime $\tau \sim 6 \times 10^7$ yr (Bobylev, 2004). In turn, the Gould's Belt is part of an older ($\tau \sim 5 \times 10^8$ yr) and more massive ($\sim 2 \times 10^7$ M$_\odot$) structure about 1000 pc in size that is known as the **Local (Orion) Arm**. Fig. 1.8 illustrates the embedding of the local disk into the large-scale spiral structure of the MW. By the star symbol the position of the Sun between the **Perseus** and the **Sagittarius-Carina** arm is plotted. The Orion spur is sketched by a long dashed line. Russeil's best *4-arm-*
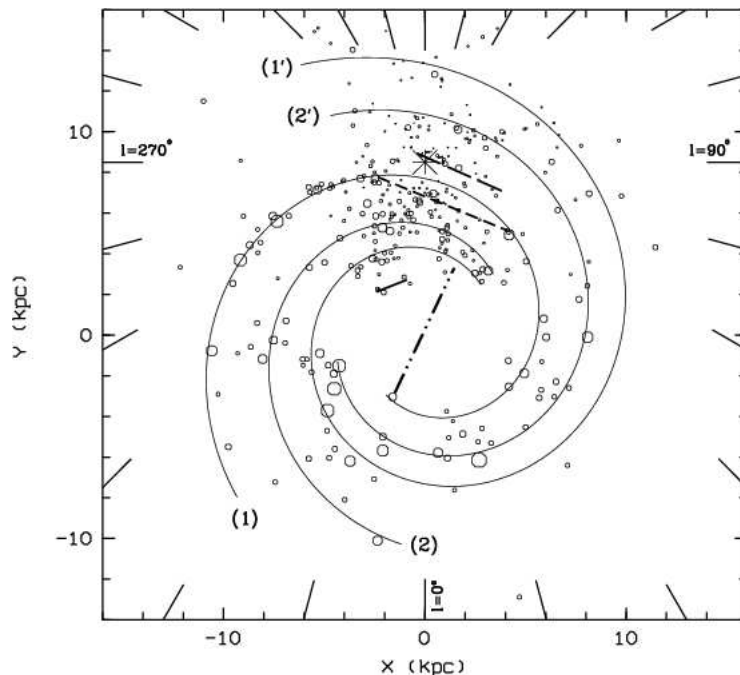

Figure 1.8: A four-arm model from Russeil (2003), Fig. 5. The symbol size is proportional to the excitation parameter of the star-forming complexes Russeil used for her work. The Sun's position is given by the large star symbol. 1: Sagittarius-Carina arm, 2: Scutum-Crux arm, 1': Norma-Cygnus arm and 2': Perseus arm. The local arm feature is sketched as a long dashed line, the bar orientation and length (dashed-dot-dot line) is taken from Englmaier and Gerhard (1999), the expected deviation from a logarithmic spiral arm observed for the Sagittarius-Carina arm (short dashed line) and finally a feature certainly linked to the 3-kpc arm (solid line).

3

model fits define a "mean arm-width" of 1.32 kpc and a "mean arm-to-arm" distance of 2.12 kpc.

In the solar neighbourhood there is about 1 star in every 10 pc^3, and the diameter of

a Sun-like object is only about $\sim 10^{-7}\,\mathrm{pc}$, so most of the interstellar space is empty of stars, but is filled up with gas and dust.

Solar Environment, an Approximation

The Oort's constants A and B are defined by the relations

$$A \;\equiv\; \frac{1}{2}\left(\frac{v_c}{R} - \frac{dv_c}{dR}\right)_{R_0} = -\frac{1}{2}\left(R\frac{d\Omega}{dR}\right)_{R_0} \tag{1.37}$$

$$B \;\equiv\; -\frac{1}{2}\left(\frac{v_c}{R} + \frac{dv_c}{dR}\right)_{R_0} = -\left(\frac{1}{2}R\frac{d\Omega}{dR} + \Omega\right)_{R_0}, \tag{1.38}$$

where $v_c(R) = \Omega R$ is the circular velocity at radius R in the disk of our Galaxy, and R_0 is the distance between the Sun and the galactic center. A represents the local shear or deviation from rigid rotation and B the local vorticity of angular momentum gradient in the disk. (In the case of $v_c = const$, $A + B = -\frac{dv_c}{dR} = 0$ and $A - B = \frac{v_0}{R_0}$.)
So the circular frequency at R_0 can be written as $\Omega_0 = (A - B)$. With Eq. 1.21 and 1.38 the value κ_0, for the solar neighbourhood is given by

$$\kappa_0^2 = -4B(A - B) = -4B\Omega_0. \tag{1.39}$$

For $A = 14.8 \pm 0.8\,\mathrm{km\,s^{-1}\,kpc^{-1}}$ and $B = -12.4 \pm 0.6\,\mathrm{km\,s^{-1}\,kpc^{-1}}$ (Feast and Whitelock, 1997); then $\kappa_0 \simeq 36 \pm 10\,\mathrm{km\,s^{-1}\,kpc^{-1}}$ and

$$\frac{\kappa_0}{\Omega_0} \simeq 2\sqrt{\frac{-B}{A - B}} = 1.3 \pm 0.2. \tag{1.40}$$

Consequently the Sun makes about 1.3 oscillations in the radial direction in the time it takes to complete an orbit around the galactic center. Hence the orbit does not close on itself in an inertial frame, but forms a rosette figure.
In the solar neighbourhood the ratio $\frac{A_x}{A_y}$ (Eq. 1.33) takes a value of $\simeq 0.7$ (Binney and Tremaine, 1994). A star out of this region travels around the epicycle in a retrograde direction, with a period of $2\pi/\kappa$ (time for one cycle $\sim 170\,\mathrm{Myr}$), the guiding center rotates on a prograde orbit with $2\pi/\Omega$.
Consider the motion of a star that moves on an epicycle orbit, as viewed from the guiding center of its orbit. At different times in the orbit the observer's proper motion (see App. D.4 in the Appendix) measurements yield the maximum values κA_x and κA_y of the velocities $\dot{x} = \frac{\partial}{\partial t}(A_x \cos(\kappa t + \psi))$ and $\dot{y} = \frac{\partial}{\partial t}(-A_y \sin(\kappa t + \psi))$. Information about the stellar epicycles can be gained by averaging the results from many stars whose orbits differ only in their epicycle phase ψ.
The Sun's position on the epicycle can be defined as well when we know its velocity with respect to that of the *LSR*. The **peculiar velocities** (Eq. 1.35,1.36,1.36) of the Sun display that it moves faster than the *LSR* velocity and this means that it is located at the inner side of an epicycle. It is on the way to reach its orbit pericenter.

Young Stars as Tracers

All information we have about stars more distant than the Sun has been deduced by observing their electro-magnetic radiation, mainly in the ultraviolet, visible, and infrared parts of the spectrum. The hottest stars are the bluest, and their spectra show absorption lines of highly ionized atoms; cool stars emit most of their light at red or infrared wavelengths and have absorption lines of neutral atoms or molecules. The sequence *O B A F G K M* distinguishes between different types of stars. It is a classification by its temperatures and compositions extracted from spectral lines. Adding luminosity and radii this sequence can be extended. Within this diagram most of the stars lie on a "S" shaped band called the Main Sequence (see App. C.2). It describes somehow the generalised time evolution of a star as starting from hot big cloud of H and He toward a colder, smaller and less luminous star consisting of various heavier molecules.

The stellar mass almost entirely determines the stellar structure and ultimate fate, the chemical composition plays a minor role. Stellar masses cover a huge range. Values between $0.8\,\mathrm{M_\odot}$ and $120\,\mathrm{M_\odot}$ are known (Sparke and Gallagher, 2000, Table1.1). The time in which such stars have a stable life on the Main Sequence (*MS*) (Sparke and Gallagher, 2000, p. 10) ranges from $25\,\mathrm{Gyr}$ for the low mass stars down to $2.6\,\mathrm{Myr}$ for the high mass stars.

O and *B* stars in the solar neighbourhood have been traditionally used as probes of galactic structure and kinematics. Their intrinsic brightness allows their observations to great distances from the Sun, and due to their youth (massive stars have a $\tau_{\mathrm{M.S.}} \sim 10^6\,\mathrm{yr}$), their motions can be expected to hold important clues to the processes that formed them. O and B stars are not randomly distributed on the sky but instead are concentrated in loose groups, the OB Associations (*OBA*). Motion and location are similar for stars belonging to the same association. Their velocity dispersion is only a few kilometers per second and so *OBA* membership studies can be done by velocity analysis. de Zeeuw et al. (1999) present a comprehensive census of the stellar content of the *OBA*s within $1\,\mathrm{kpc}$ from the Sun based on Hipparcos data.

Substructures near the Sun

The local medium, within a few hundred parsecs, is dominated by a substructure called the Gould's Belt (*GB*).
It was Sir John Herschel (1847) to first note that the brightest naked-eye stars were not regularly distributed on both sides of the MW's great circle, but showed a secondary concentration towards a major circle tilted about 20° to the MW. Systematic work on this local feature was carried out by Benjamin Gould (1879), after whom this feature is named. This local system is traced by young stars and OBAs, HI, molecular clouds and dust (Poppel, 1997).

Torra et al. (2000) examined the local velocity field by using a large sample of nearby *O* and *B* stars from the Hipparcos catalogue and found that approximately 60% of the stars younger than 60 Myr belong to the GB. Perrot and Grenier (2003)
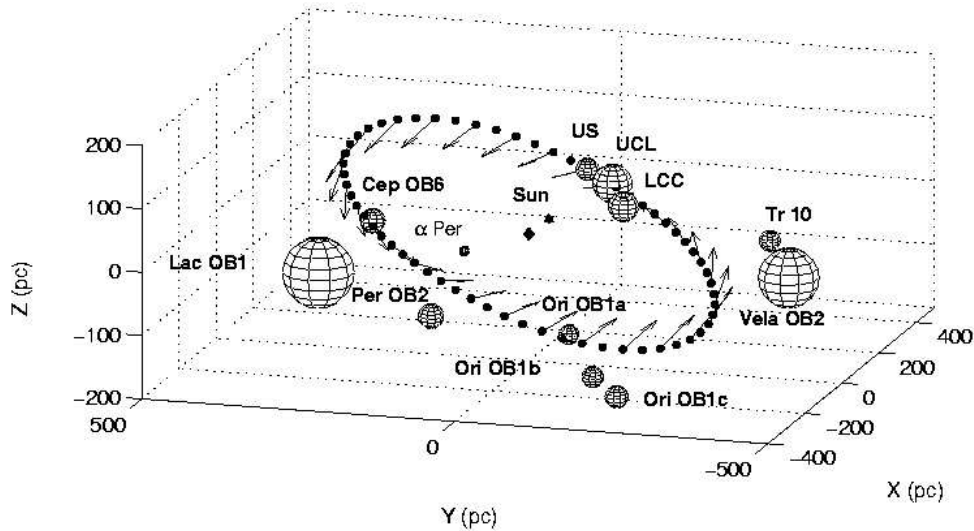

Figure 1.9: 3*D* view of the Belt rim and its velocity field (wrt the OBAs that are marked as spheres with a radius equal to their size (de Zeeuw et al., 1999). The diamond and the star note the Belt's center and the Sun, respectively. (Perrot and Grenier, 2003, Fig. 6)

modeled in 3*D* the dynamical evolution of the GB and compared it to the spatial and velocity distributions of all *HI* and H_2 clouds found within a few hundred parsecs from the Sun and to the Hipparcos distances of the nearby OBAs.

The best fit to the data yields values for the current Belt's semi-axes of 373 ± 5 pc and 233 ± 5 pc, and an inclination of $17.2° \pm 0.5°$. These characteristics are consistent with earlier results, but a different orientation of the Belt has been found because of the presence of new molecular clouds and the revised distance information: the Belt's center currently lies 104 ± 4 pc away from the Sun, towards the galactic longitude $l = 180.4° \pm 2.0°$, and the ascending node longitude is $\Omega_G = 296.1° \pm 2.0°$. Torra et al. (2000) reasoned in their work, that the GB extends up to 600 pc from the Sun with an inclination with respect to the galactic plane of $i_G = 16 - 22°$ and the ascending node placed at $\Omega_G = 275 - 295°$.

Age analysis of the Belt is rather uncertain. The dynamical time scale worked out by Perrot and Grenier (2003) is 20 to 30 Myr and the stellar age determination done by Torra et al. (2000) yields 30 to 60 Myrs ; a factor of 2 difference.

The motion of young nearby stars deviates considerably from the general field of galactic rotation (Torra et al., 2000). Analyses correspond to an overall expansion of the local system of the earliest stars. Years ago Campbell (1913) recognized this

as the main kinematic characteristic of the GB. In Fig. 1.9 the velocity field (wrt LSR) outlines the Belt's expansion. The simulated GB rim from Perrot and Grenier coincides with most of the nearby OBAs, but the mean velocities of the associations do not seem to be related to the Belt's expansion.

Lindblad et al. (1997) mention that the GB moves away from the GC at $\sim 5\,\mathrm{km\,s^{-1}}$ and it expands at a rate of about $\sim 12\,\mathrm{km\,s^{-1}\,kpc^{-1}}$. In 2004, Bobylev analysed the space velocities of nearby, young GB stars by assuming the existence of a single kinematic center; $(l_{GB} = 128°, R_{GB} = 150\,\mathrm{pc})$. The velocities they found for a sample with stars younger than $60\,\mathrm{Myr}$ was $-6\,\mathrm{km\,s^{-1}}$ for the rotation (whose direction coincides with the galactic rotation) and $4\,\mathrm{km\,s^{-1}}$ for the expansion.

Torra et al. worked out that stars belonging to $Soc - Cen$ or $Ori\ OB1$ complexes, the two most dominant associations of the GB, are not primarily responsible for the ring peculiarities. A sample with or without these stars made no significant difference in their Belt analysis.

Several models have been presented in order to explain the origin of the GB: it has been interpreted as a local effect of the spiral arm (Lindblad et al., 1997), as energetic events on the galactic disk (Elmegreen, 1982), as expanding stellar groups (Blaauw, 1952), as the interpretation of the local gas kinematics in terms of an expanding ring (Moreno et al., 1999), and also as a supercloud which was initially moving almost ballistically in the galactic field until an encounter with a major spiral arm started a braking process (Olano, 2001). Another scenario is from Comeron (1993), the impact of a high velocity cloud on the galactic disk.

Kinematics in the Solar Neighbourhood

Dehnen (1998) worked out the velocity distribution in u and v directions, by intering these components from Hipparcos data for 3527 main-sequence stars with $B - V > 0.6$ and 2491 mainly late-type non-main-sequence stars, high-velocity stars excluded, in the solar neighbourhood.

Fig. 1.10 shows the distribution of a bi-modality which has become known as the **u-anomaly** (see also Raboud et al., 1998) especially for the late-type stars. (u, v) denote the stars velocity components with respect to the LSR. The anomaly consists of an additional peak around $(u, v) = (-40, -20)\,\mathrm{km\,s^{-1}}$. The respective stars are lagging behind the mean rotation and have an outward radial motion with respect to the LSR.

Recently Alcobé and Cubarsi (2005) published a full space motion analysis of a HIPPARCOS catalogue stellar sample. $13'678$ stars are included which are maximally $300\,\mathrm{pc}$ remote from the Sun. They discriminate differentiated statistical behaviours that are associated with stellar populations in the solar neighbourhood (see Fig. B.1 in the Appendix).
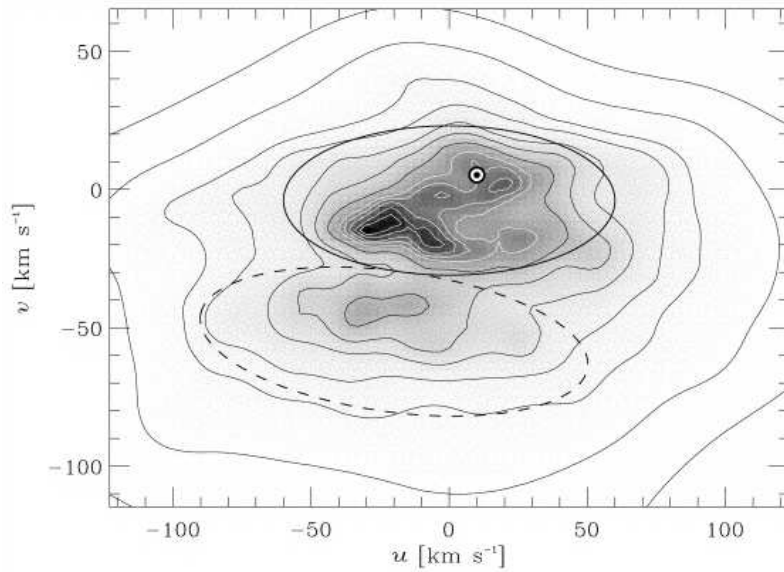
Figure 1.10: Distribution in u and v velocity space from HIPPARCOS data. The circled dot indicates the solar velocity. Samples of early-type stars contribute almost exclusively to the low-velocity region (solid ellipse), which contains the most prominent moving groups. The region of intermediate velocities (dashed ellipse) is mainly represented by late-type stars, of which $\sim 15\%$ fall into this region. Gray scales are linear in the velocity distribution and the contours contain, from inside out, $2, 6, 12, 21, 33, 50, 68, 80, 90, 95, 99$, and 99.9% of all stars. The 1σ uncertainty in the contour lines is about $3\,\mathrm{km\,s^{-1}}$. (see Dehnen (2000); Fig.9)

1.3.3   Orbital Resonance Effects

The solar neighbourhood shows irregularities which can perhaps be explained by resonant phenomena produced by the main substructures of our Galaxy. Both the spiral arms *and/or* the bar could be responsible for such effects.

Lindblad Resonances

Lindblad Resonances[4] are defined by the intersection of a pattern speed Ω_p and combinations of the natural frequencies Ω and κ. Fig. 1.11 shows the **Resonance Diagram** of a MW model (mod1-BA). The used potential is the same as the *Standard model 20* from Bissantz et al. (2003) but with a halo modification, see Chap. 5. These kind of models for the orbit analysis are used within this thesis. Red lines rep-
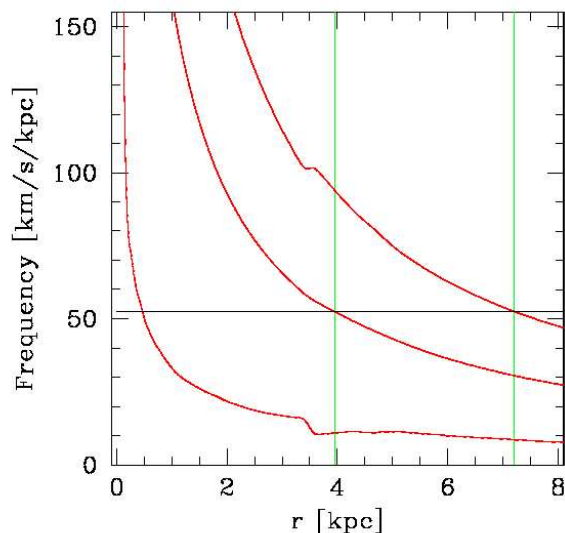

Figure 1.11: Resonance diagram for *mod1_BA*. Angular frequencies are shown in red. The black line corresponds to the bar's pattern speed. Intersections define the Lindblad Resonances as described in the text.

resent the angular frequencies. $\Omega(R) \pm \frac{1}{2}\kappa(R)$ are the higher and lower ones, $\Omega(R)$ is plotted in the middle. The pattern speed of the bar is shown by the straight black line crossing the frequencies. The innermost intersections define the **Inner Lindblad Resonance** (ILR) and the outermost the **Outer Lindblad Resonance** (OLR). The middle intersection, where $\Omega(R) = \Omega_p$ is called the **Co-Rotation** (CR), here the underlying stellar velocity field is equal to that of the bar.

---

[4]They are called Lindblad resonances, after the swedish astronomer Bertil Lindblad ($1895 - 1965$).

The resonance condition is usually written as

$$\Omega_p = \Omega(R) - \frac{n}{m}\kappa(R). \tag{1.41}$$

Since this condition makes reference to circular velocities and epicycle frequencies, the entire concept is always related to the linear regime, where the epicycle approximation or some analogue is valid. In this sense, every resonance corresponds to a certain radius where Eq. 1.41 is fulfilled for some (n, m) values.

When viewed in the frame co-rotating the bar (see Chap. 5), the resonance condition means that the corresponding epicycle orbit is closed. A particle will have completed m cycles of its radial oscillation while having circled n times around the center.

Since in the outer regions of the Galaxy $\Omega(R)$ will always be a decreasing function of R, orbits further out than CR will appear retrograde in the co-rotating frame. Most resonances come in pairs, with one prograde member inside the CR radius, and one retrograde outside. These pairs correspond to positive and negative sign of a certain n. An overview of the most important resonances is shown in Tab. 1.4.

	n	m	
CR	0		Co-Rotation
OLR	-1	2	Outer Lindblad Resonance
ILR (IILR,OILR)	+1	2	Inner Lindblad Resonance depending on $(\Omega_p, \Omega, \kappa, n, m)$ more than 1 ILR-intersection can occur

Table 1.4: Special cases

A bar potential has a multipole order of 2 given by its symmetry, and therefore these resonances are supposedly the most significant.

Bar Effects

There is strong observational evidence and dynamical ground, that bars in galaxies are confined to regions within the radius R_{CR} of the co-rotation resonance. So this radius can be seen as an upper limit for the bar-length. Nonetheless a bar influences the outer parts of its host galaxy, most obviously by resonant phenomena.

Using linear perturbation theory for near-circular orbits (Binney and Tremaine, 1994), one finds that closed orbits in a barred potential are elongated either parallel or perpendicular to the bar. The orientation changes at each of the fundamental resonances: inside the ILR orbits are anti-aligned (so-called x2 orbits), between the ILR and the CR they are aligned (x1 orbits), while between the CR and the OLR the orbits are again anti-aligned (x1(2)), until they align again beyond the OLR (x1(1)).

The situation at the OLR is sketched in Fig. 1.12, which shows two closed orbits (solid curves) just inside and outside the OLR as they appear in a frame of reference
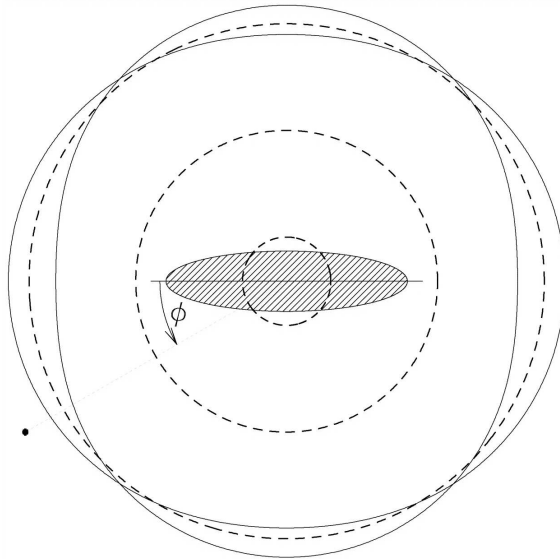
Figure 1.12: Closed orbits (solid curves) just inside and outside the OLR of a rotating central bar (hatched ellipse). The dashed circles depict the positions of the ILR, CR, and OLR for circular orbit's. Note the change of the orbits orientation at the OLR, resulting in the crossing of closed orbits at four azimuths. The dot at the lower left presents a possible position of the Sun. (Dehnen, 2000, Fig.1).

co-rotating with the bar. In this frame, the orbits near the OLR rotate counter-clockwise for a clockwise-rotating bar, like the situation is in our MW. Thus, at bar angles φ (In Fig. 1.12; $\Phi \equiv \varphi$.); between $0 - 45°$, the closed orbits inside the OLR move slightly outward, while those outside the OLR move inward. Clearly, if all disk stars moved on closed orbits, the stellar kinematics would deviate from that of a nonbarred galaxy only at positions very close to the OLR, where the closed orbits are significantly non-circular. In particular, at azimuths where the closed orbits from either side of the OLR cross, one would expect two stellar streams, one moving inward and the other outward.

Fux (2001) and Dehnen (2000) found that if the Sun is just outside the OLR such influence could explain the *u-anomaly* (see Fig. 1.10).

Dehnen showed the evidence that for positions up to 2 kpc outside the OLR radius and at bar angles of $\sim 10-70°$, such features took the form of a bimodality between the dominant mode of low-velocity stars centered on the LSR and a secondary mode of stars predominantly moving outward and rotating more slowly than the LSR.

The bimodality present in the locally observed Fig. 1.10 is indeed very similar to those emerging from the simulations presented in Dehnen (2000).

By using direct orbit integrations, Mühlbauer and Dehnen (2003) studied the kinematic response of the outer stellar disk to the presence of a central bar, similar to
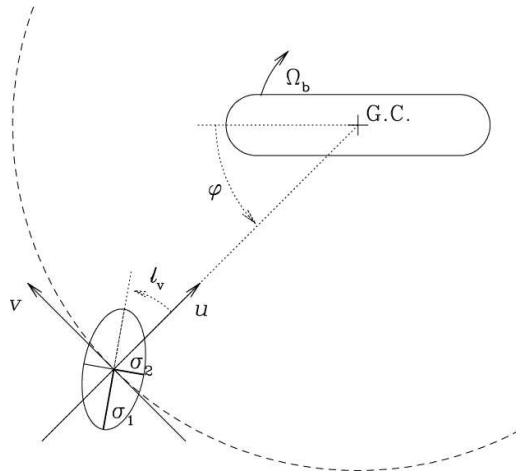
Figure 1.13: Geometry of the rotation of the galaxy and definition of coordinate system. Note that positive values of radial velocity u are taken to point inwards and that azimuth angle φ is measured from the bar major axis in the mathematically positive sense, opposing to the direction of bar rotation in the MW (*modulo* 180°). Also shown is a velocity dispersion ellipsoid with its principal components σ_1 and σ_2 and a (positive) vertex deviation ℓ_v (Mühlbauer and Dehnen, 2003, Fig.1).

the situation in the MW. They found that the bar's OLR causes significant perturbations of the velocity moments. With increasing velocity dispersion, the radius of these perturbations is shifted outwards, beyond the nominal position of the OLR, but also the disk becomes less responsive. Following Dehnen (2000) in assuming that the OLR occurs just inside the solar circle and that the Sun lags the bar major axis by $\sim 20°$ (e.g. Bissantz and Gerhard, 2002), they found

1. no significant radial motion of the LSR,

2. a vertex deviation of $\ell_v \sim 10°$ and

3. a lower ratio σ_2^2/σ_1^2 of the principal components of the velocity-dispersion tensor compared to an unperturbed disk. (For the coordinate system see Fig. 1.13.)

All of these are consistent with the observations of the solar neighbourhood kinematics. Thus it seems that at least the lowest-order deviations of the local-disk kinematics from simple expectations based on axisymmetric equilibrium can be attributed entirely to the influence of the galactic bar. Generally they found that these deviations are largest near the OLR, the apparent radius of which, however, may be shifted outwards by $10 - 20\%$ due to the non-circularity of the orbits in a warm stellar disk.

Radial motions $\bar{u}$ of standards of rest can be seen to occur quite frequently (see Fig. 1.14), and can reach magnitudes of the order of about $0.02v_0$, corresponding
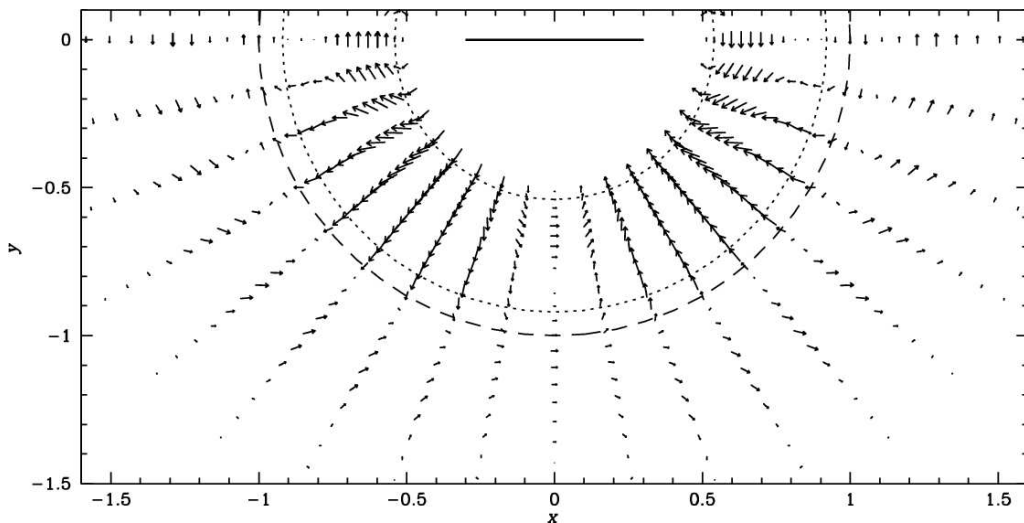
Figure 1.14: Bar-induced deviations of the mean velocity from the unperturbed state up to $m = 2$ for $\sigma_0 = 0.2v_0$. The bar is aligned with the horizontal axis and is supposed to rotate clockwise. The solar circle is dashed, dotted circles are CR and OLR. x and y axis are normalized to $R_\odot$, the solar circle (Mühlbauer and Dehnen, 2003, Fig.8).

to about $5\,\mathrm{km\,s^{-1}}$ for the MW. Because of the $\sin 2\varphi$ dependence, these would be maximal at $\varphi = 45°$, which is quite near the proposed position of the Sun ($\varphi_0 \approx 30°$; see Tab. 1.1). In its radial dependence however, $\bar{u}$ swings through zero shortly outside of the OLR, and it may well be that the Sun just meets that point. So they cannot give a definite prediction for the bar-induced radial motion of the Sun's LSR, not even for its sign, except that it should be very small (at most a few $\mathrm{km\,s^{-1}}$). This is consistent with a measurement[5] of $\bar{u} = 1.5 \pm 2.2\,\mathrm{km\,s^{-1}}$ for the mean radial motion of a sample of halo subdwarfs with respect to the LSR (Gould (2003)& its erratum 2004).

Spiral Arm Effects

Quillen and Minchev (2005) explain the *u-anomaly* with the effect of spiral arms. Clumps in the solar neighbourhood's stellar velocity distribution could be caused by spiral density waves. In the solar neighbourhood, stellar velocities corresponding to orbits that are nearly closed in the frame rotating with a spiral pattern represent likely regions for stellar concentrations. Via particle integration Quillen and Minchev

---

[5]Gould (2003)/Gould (2004) calculated the stellar halo parameters out of 4588 subdwarfs. He claims, that the bulk halo motion relative to the LSR are not far from the movement of the Sun relative to the LSR. So all his velocity-ellipsoid parameters are within their errors consistent with zero, or more precisely mentioned: $V_1 = 1.5 \pm 2.2\,\mathrm{km\,s^{-1}}$ and $V_3 = 0.3 \pm 2.4\,\mathrm{km\,s^{-1}}$; (radial/outward,vertical/upward)

showed that orbits can intersect the solar neighbourhood when they are excited by Lindblad resonances with a spiral pattern. They found that a two-armed spiral density wave with pattern speed placing the Sun near the 4 : 1 ILR can cause two families of nearly closed orbits in the solar neighbourhood. One family corresponds to square-shaped orbits aligned so that their peaks lie on top of, and support, the two dominant stellar arms. The second family corresponds to orbits 45° out of phase with the other family. Such a spiral density pattern could account for two major clumps in the solar neighbourhood's velocity distribution. The Pleiades/Hyades moving group corresponds to the first family of orbits, and the Coma Berenices moving group corresponds to the second family. Quillen and Minchev's model requires a spiral pattern speed of approximately 0.66 ± 0.03 times the angular rotation rate of the Sun, which is $18.1 \pm 0.8 \, \mathrm{km \, s^{-1} \, kpc^{-1}}$.

Chapter 2

The OB Star Sample

The goal of this section is to identify a sample of OB stars with complete phase space information, for kinematic analysis in later sections, and to investigate the characteristics of this sample such as completeness, errors, etc.
A detailed description of catalogues and coordinate transformations used is given in App. D.

2.1   Basic Sample

We begin with the 10'533 O and B stars in the Hipparcos catalogue (Perryman et al., 1997) which are listed with detailed spectral type (hereafter sample B10). The spectral classification information given in the Hipparcos catalogue (spectral type plus luminosity class) is taken from various Hipparcos-external sources (see Perryman et al., 1997), notably the Michigan Spectral Survey in the southern sky (Houk and Smith-Moore, 1988) and the SIMBAD data base.

We use trigonometric distances for these stars from the Hipparcos catalogue, and photometric distances from Drimmel (2000). The trigonometric parallaxes are given in the catalogue for all stars, even if the value given is not significant or negative (i.e., the true parallax is smaller than its error), but they will be used only when sufficiently accurate; see below.

The photometric distances for the stars with complete spectral classification are taken from Drimmel (2000); they are calculated using the absolute magnitudes and colors for the different stellar types from Schmidt-Kaler (1982). For the stars without luminosity classification (hereafter, *nonLC stars*), photometric distances are based on reddenings and estimated absorptions (Smart et al., 1997); these distances are much less accurate. In addition, the nonLC stars are predominantly in the North, because of the use of the more complete Michigan Spectral Survey in the South. Thus including these stars would result in distance errors that are systematically larger in the North. For these reasons we exclude the 3291 nonLC OB stars from our sample.

For some stars, errors in B-V and the cosmic scatter in $(B-V)_0$ can result in

formally negative values of the measured B-V, and thus in negative values for the absorption A_V used in the photometric parallax determination. We also exclude the 241 stars with such non-physical data, leaving 7001 OB stars in the sample (LB10 hereafter).

Radial velocities for these stars are taken from the General catalogue of mean radial velocities III/213 of 36′145 stars (Barbier-Brossat and Figon, 2000, hereafter BB00), using HIP = HIC as a matching criterion. The resulting sample (basic sample RB10) is composed of 3380 OB stars with complete phase-space information: Positions *(Galactic coordinates l,b; heliocentric distances)*, space motions *(radial velocities; proper motions)*. Further data about these stars *(spectral types; luminosity classes; magnitudes)* are also retained. Figure 2.1 shows the positions and velocities of the stars from this sample that fall in an $8\,\mathrm{kpc} \times 8\,\mathrm{kpc}$ square around the Sun.

2.2 Errors for Observed and Inferred Quantities

2.2.1 Position (α, δ)

The Hipparcos errors for the observed positions (α, δ) are negligible for this work.

2.2.2 Distances

We use the trigonometric distances from Hipparcos as long as the error given is at most 20%. If the parallax error exceeds 20% or the value given is negative or zero, we use the photometric distances. The maximum distance of OB stars with parallax errors $\leq 20\%$ is around 440 pc. Thus in our basic sample, 1017 stars have distances given by parallax measurements and 2353 have distances determined from spectroscopic parallaxes.

The errors of photometric distance determinations are difficult to determine. Some papers use global errors of $20 - 40\%$ (Russeil, 2003). We use the photometric distances from Drimmel (2000) along with their estimated errors for the absolute magnitude,

$$\sigma_M = 0.5 + max[0, (m - 6.5)/6] - M/12. \tag{2.1}$$

Here the term depending on apparent magnitude m can be interpreted as a result of the higher occurrence of classification errors at fainter magnitudes, and the term depending on absolute magnitude M can be seen as an increasing cosmic error and/or uncertainty for the more luminous stars. Errors for the stars with $D \leq 4\,\mathrm{kpc}$ in the basic sample computed from Eq. 2.1 are shown in the top panel of Figure 2.2, along with a curve showing the mean dependence on distance.

The logarithmic dependence of the distance modulus $m - M = 5\lg(D) - 5 + A_V$ on distance leads to an asymmetric distribution of distance errors; for $\Delta M = \pm\sigma_M$ we have $\Delta \lg(D) = \mp\sigma_M/5$ or

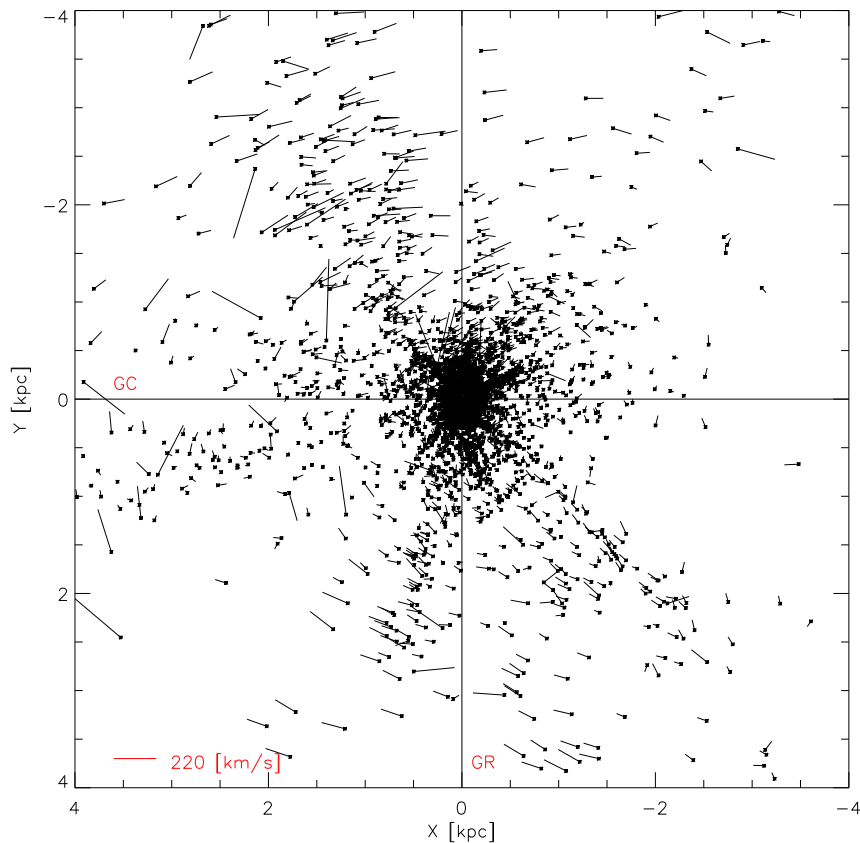$$\Delta D_\pm = D \times \left(10^{\mp\sigma_M/5} - 1\right). \tag{2.2}$$

Figure 2.1: Heliocentric positions and velocities projected onto the Galactic plane for the OB stars in the Basic Sample RB10 (3305 of 3380 stars fall within the plot). The plot shows an $8\,\mathrm{kpc} \times 8\,\mathrm{kpc}$ square around the Sun, which is located at the origin of the coordinate system in the figure. The Galactic Center (GC) is located in the direction of the positive X-axis, at (8 kpc, 0). The direction of Galactic rotation (GR) is downwards in this plot, along positive Y. The small *–symbols indicate the projected positions of the stars, the lines indicate the directions and amplitudes of their velocities relative to the Sun. The length of the bar in the lower left corner corresponds to a velocity of $220\,\mathrm{km\,s^{-1}}$. Due to differential Galactic rotation, the OB stars as a whole appear to "fly" from the lower right corner around the Sun to the upper right corner.

Distance errors determined from this equation for the stars in the basic sample RB10 are shown in the second panel of Figure 2.2. Both the points for the individual stars and the curves for the mean dependence on distance clearly show the asymmetry between the near and far sides implied by Eq. 2.2. Differentiating the distance modulus gives

$$\frac{\partial(m-M)}{\partial D} = \frac{5}{\ln 10}\frac{1}{D},\tag{2.3}$$

so for small σ_M and σ_D one has in linear approximation

$$\sigma_D = \frac{\ln(10)}{5}\sigma_M D.\tag{2.4}$$

The approximation $\Delta D = \sigma_D$ is also shown in Figure 2.2; it is intermediate between the curves from Eq. 2.2. All three curves show an approximately linear increase with distance.

2.2.3 Proper Motions and Velocities

Proper motions and their errors are taken directly from the the Hipparcos catalogue. Heliocentric radial velocities come from the catalogue of Barbier-Brossat and Figon (2000), which also lists errors for most of these radial velocities. Some radial velocity errors are given only in terms of letter codes, which translate into estimated values in multiples of $5\,\mathrm{km\,s^{-1}}$. 217 stars in our sample have no radial velocity errors given in the catalogue. For these stars we use a constant error $\sigma_{RV} = 8\,\mathrm{km\,s^{-1}}$, corresponding to the mean error computed for the stars with catalogue errors, which is independent of distance. The stars without error listed in the catalogue have no bias with respect to their directions or distances.

Torra et al. (2000) used another sample of O and B stars from the Hipparcos catalogue, with distances up to heliocentric 1.5 kpc and a cut in the radial velocity error of $10\,\mathrm{km\,s^{-1}}$. Then the resulting mean radial velocity error in their sample is $3\,\mathrm{km\,s^{-1}}$ (see their Fig. 9). We have not made such a cut, because for stars beyond $\sim 800\,\mathrm{pc}$, the proper motion errors dominate.

From radial velocities, proper motions, and distances we calculate velocities U, V, W relative to the Sun's velocity, where positive U is inwards along the direction Sun–Galactic Center, positive V is along the direction of Galactic rotation, and positive W is upwards from the Galactic plane. The bottom two panels of Figure 2.2 show the errors in (U, V) obtained by standard error propagation of the catalogue errors for the proper motions and radial velocities and the estimates (2.4) for the distance errors. Mean error curves computed as before are also shown. These mean errors rise from about $5\,\mathrm{km\,s^{-1}}$ within a few hundred pc of the Sun to $18\,\mathrm{km\,s^{-1}}$ and $14\,\mathrm{km\,s^{-1}}$ in U and V at $2\,\mathrm{kpc}$ distance, respectively.
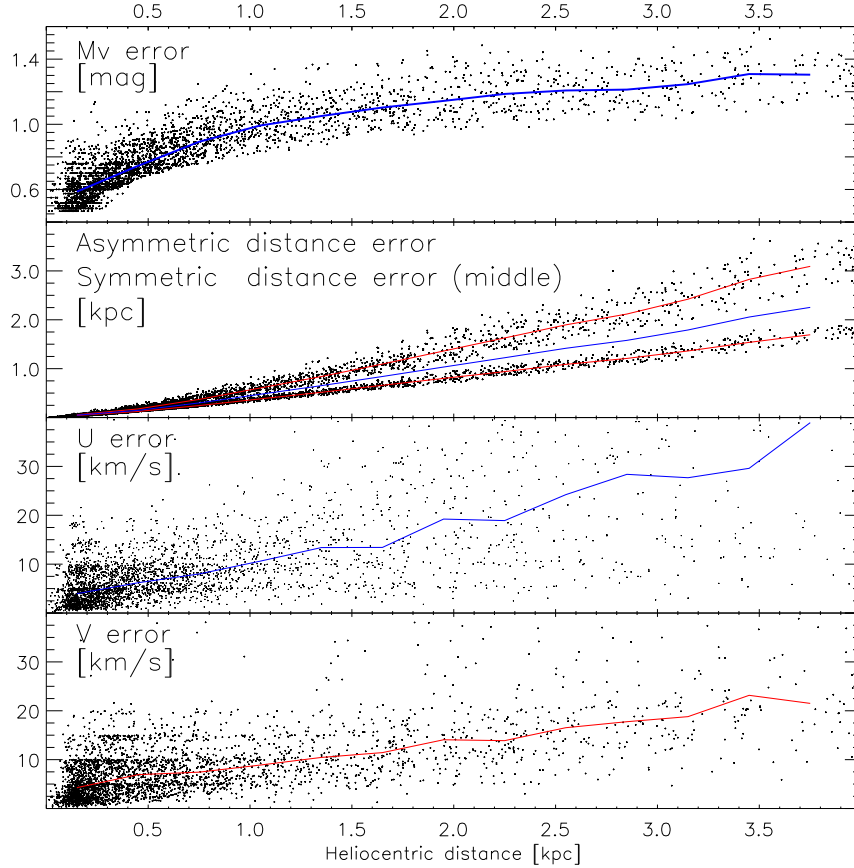
Figure 2.2: Errors in the absolute magnitudes, distances, and inferred U, V velocities of the 3276 stars in the basic sample with $D \leq 4\,$kpc, versus their heliocentric distances (dots). The top panel shows the absolute magnitude errors estimated from Eq. 2.1; the thick blue line shows a mean value, determined in each distance bin as the arithmetic mean of the $\pm 25\%$ stars around the median error for all stars in the bin. The second panel shows individual derived distance errors corresponding to $1\sigma_M$ magnitude errors towards the near and far sides [lower and upper distributions of points and red lines, cf. Eq. 2.2], as well as the symmetric linear estimate from Eq. 2.4 (middle blue curve). Curves for the mean errors are computed similarly as for the magnitude errors. The bottom two panels show the derived errors in the two in-plane velocities U, V, obtained by standard error propagation of the catalogue errors for proper motions and radial velocities, and the estimates (2.4) for the distance errors. The mean error curves computed as before are also shown.

2.3 Completeness

In this Subsection we discuss the completeness of our sample, particularly in view of possible kinematic biases. The simplest and surest way to ensure an unbiased sample is to examine only the complete magnitude range of the catalogue, so this is discussed first.

2.3.1 Magnitude Limited Samples

According to Mignard (1997); Perryman et al. (1997), the completeness of the Hipparcos catalogue depends on latitude and spectral type and varies from $m_V = 7.3$ near the galactic plane to $m_V = 9.0$ in the polar regions. Comparing with the Tycho catalogue, which is 99.9% complete to $m_V = 10.0$ (Egret and Fabricius, 1997), 59 (857) Tycho stars with m_V brighter than 7.0 (7.5) were found missing in the Hipparcos catalogue (Drimmel, 2000; Smart et al., 1999), suggesting that the Hipparcos catalogue is 99.5% (97%) complete to these magnitude limits. These authors used the classical approach of examining the log of the number of sample stars in successive apparent magnitude bins, to investigate the completeness of the Hipparcos OB star sample with full spectral classification, $\pi < 2\text{mas}$, and $|b| < 30\,\text{deg}$. From comparing with a straight line fitted to the (essentially complete) magnitude range 5.0...7.0, they estimated that this sample is approximately 98% (96%) complete to $m_V = 7.6$ (8.0). Here we follow a similar approach for the samples used in the remainder of this work.

Figure 2.3 shows histograms of the log of the number of stars in bins of apparent magnitude, for the B10 sample, a subsample of OB stars of type B3 and earlier (B3, ages less than approximately 60 Myr), and the subsample of OB stars of type B6 and later (B6+, main sequence lifetimes greater than approximately 150 Myr). The first two histograms do not include stars nearer than 600 pc, in order to avoid effects of local OB associations in the Gould belt. Most stars in the B6+ sample are closer than this distance, so for this sample this is not practical. For each of these samples, we fit a straight line to the magnitude range indicated on the plot and interpret the fall of the logarithmic counts at faint magnitudes as the onset of sample incompleteness. From these plots we estimate magnitude limits (where the number of stars in the bin is half that implied by the fit) between $m_{V,\text{lim}} = 8.0$ to 8.2. Down to $m_{V,\text{lim}}$, these samples are about 80% complete. Completeness values estimated from the figures down to other apparent magnitude cutoffs are given in Table 2.1.

It should be noted that there is some uncertainty to these values. Varying the fitted magnitude range by ± 0.5 mag and the bin sizes by ± 0.1mag can change the completenesses so determined by up to 7%. Also, including the stars nearer than 600 pc makes the slope of the fitted line shallower, thus increases the completeness at fixed magnitude and pushes the completeness magnitude to fainter values. The values given in Table 2.1 for the B10 and B3 samples are therefore lower limits.
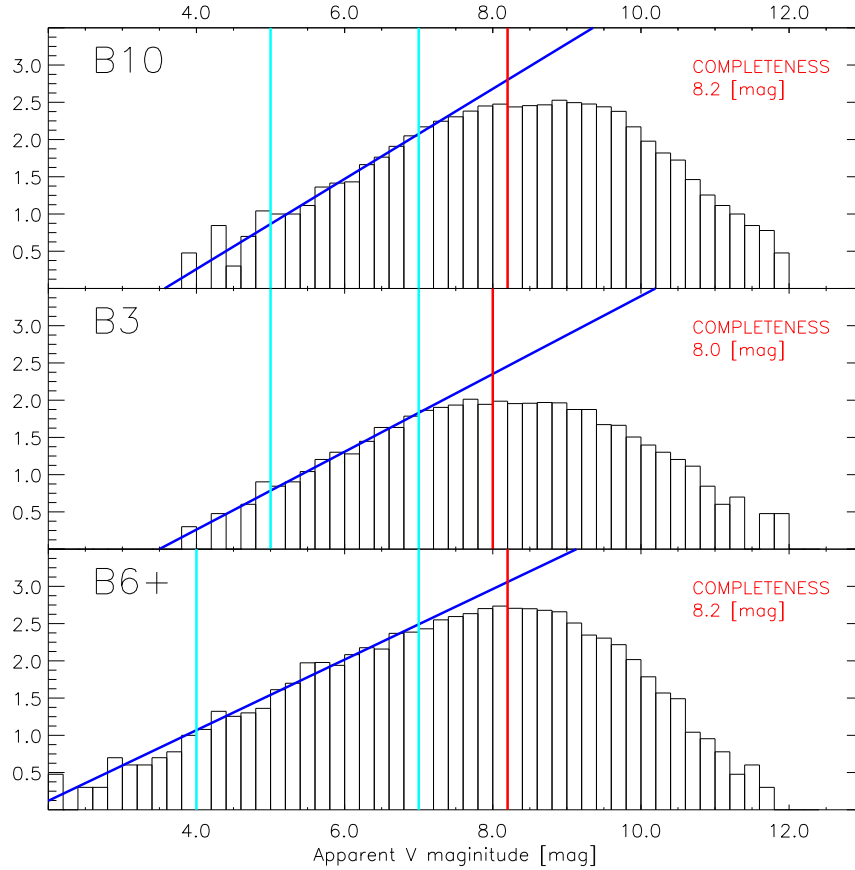
Figure 2.3: The log of the number density per apparent magnitude bin, $0.2[mag]$, for three samples of OB stars. The top panel is for all stars in the $B10$ sample with distances $D > 600$ pc. The second panel is for all stars of type $B3$ and earlier, again with $D > 600$ pc (sample $B3$). The bottom panel is for an older star sample ($B6+$) with types $B6$ and later; here there are no distance restrictions because almost all of these stars are near the Sun. For all three samples, the deviation of the logarithmic counts from the straight line, fitted to the magnitude range $m_V = 5$ to 7 mag for $B10$ and $B3$, and $m_V = 4$ to 7 mag for $B6+$, gives an estimate of where incompleteness starts. The $B10$ sample is comparable with the sample studied in Smart et al. (1999). The red lines illustrate the respective magnitude limits (where the number of stars in the bin is half that implied by the fit). Estimated completenesses for several values of apparent magnitude are given in Table 2.1.

m_V			7.0	7.4	7.8	8.0	8.2	8.4
B10	0.61	4553	103.3	102.7	92.9	86.8	**78.9**	68.8
B3	0.52	1542	98.6	94.7	84.3	**75.8**	67.7	59.2
B6+	0.47	7015	99.0	92.5	84.1	79.5	**74.3**	67.5
	slope	N(sample)						

Table 2.1: Cumulative completeness of the three samples, down to various magnitude limits, estimated by comparing the number of stars in the respective histograms shown in Fig.2.3 with the corresponding fitted slope. Columns give: (1) the sample; for $B10$ and $B3$ stars closer than $D \leq 600$ pc are excluded to avoid irregularities produced by local feature effects. In the older sample $B6+$ this is not feasible because almost all these stars are located near the sun; (2) the fitted slope; for a uniform distribution of stars the *log* of the cumulative counts should increase linearly with a slope of 0.6, see Smart et al. (1999); (3) the number of stars in the sample histograms in Fig.2.3; (4-9) cumulative completeness down to magnitude m_V. The bin-wise completeness is 50% at the limiting magnitude, $m_V = 8.0$[mag] for sample $B3$ and 8.2[mag] for samples $B10$ and $B6+$; cumulative completenesses for the limiting magnitudes are given in bold face.

2.3.2 Subsamples with Radial Velocities

Figures 2.4–2.5 show the fraction of stars in the B3, B6+, and B10 samples with complete luminosity class information and with radial velocity from BB00, as well as the radial velocity completeness, both differential in bins of apparent magnitude and cumulative from the bright end down to a given magnitude. As radial velocity completeness we take the fraction of LC stars with measured radial velocity, assuming that the luminosity classification is uncorrelated with the availability of a radial velocity measurement. One sees that the B3 sample is the most complete, with 90% of the stars down to $m_{V,\mathrm{lim}} = 8.0$ having radial velocities, whereas the older B6+ sample is only $\sim 45\%$ complete down to its $m_{V,\mathrm{lim}} = 8.2$, and the B10 sample $\sim 60\%$ complete down to $m_{V,\mathrm{lim}} = 8.2$. Figure 2.6 shows that the B3 sample does not have a large kinematic bias, as some earlier samples had (Binney et al., 1997b): around 90% of the stars with the smallest proper motions in this sample have a radial velocity measurement.

To summarize this section: the B3 sample can be considered complete down to a limiting magnitude of $m_V = 8.0$, and down to this limiting magnitude, it is 90% complete in radial velocities, both overall and differentially even for the lowest proper motion stars. We will thus use this sample restricted to $m_V \leq 8.0$ (hereafter, RB3-8.0) to obtain a kinematically unbiased sample. A second sample will be obtained from the B10 sample without magnitude limit. The results based on this sample will be compared with those from the B3 sample to check for possible effects of

kinematic bias. First, however, some further cuts are needed, as described in the next Subsection.
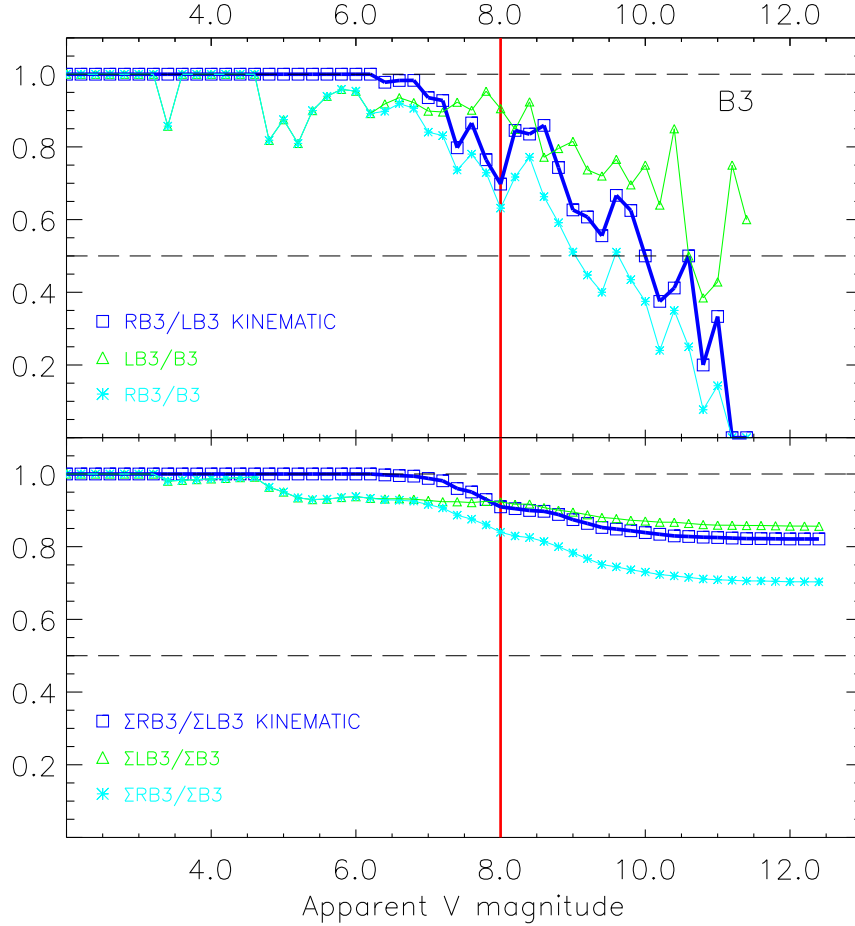

Figure 2.4: Radial velocity completeness of the B3 sample, per bin (upper panel) and cumulative (lower panel). The blue squares and thick dark blue lines show the fraction of B3 sample stars with full luminosity classification (sample LB3) that have also radial velocities (sample RB3). The bin-wise and cumulative ratios RB3/LB3 and ΣRB3/ΣLB3 quantify the purely kinematic aspect of the subsample (in)completeness. The green triangles and green lines show the fraction of all stars of type B3 and earlier in the Hipparcos catalogue that have complete spectral classification, LB3/B3 and ΣLB3/ΣB3, and the light-blue stars and thin lines show the fraction of all stars of type B3 and earlier in the Hipparcos catalogue that have complete spectral classification *and* radial velocities, RB3/B3 and ΣRB3/ΣB3. The vertical red line shows the completeness magnitude from Fig. 2.3.
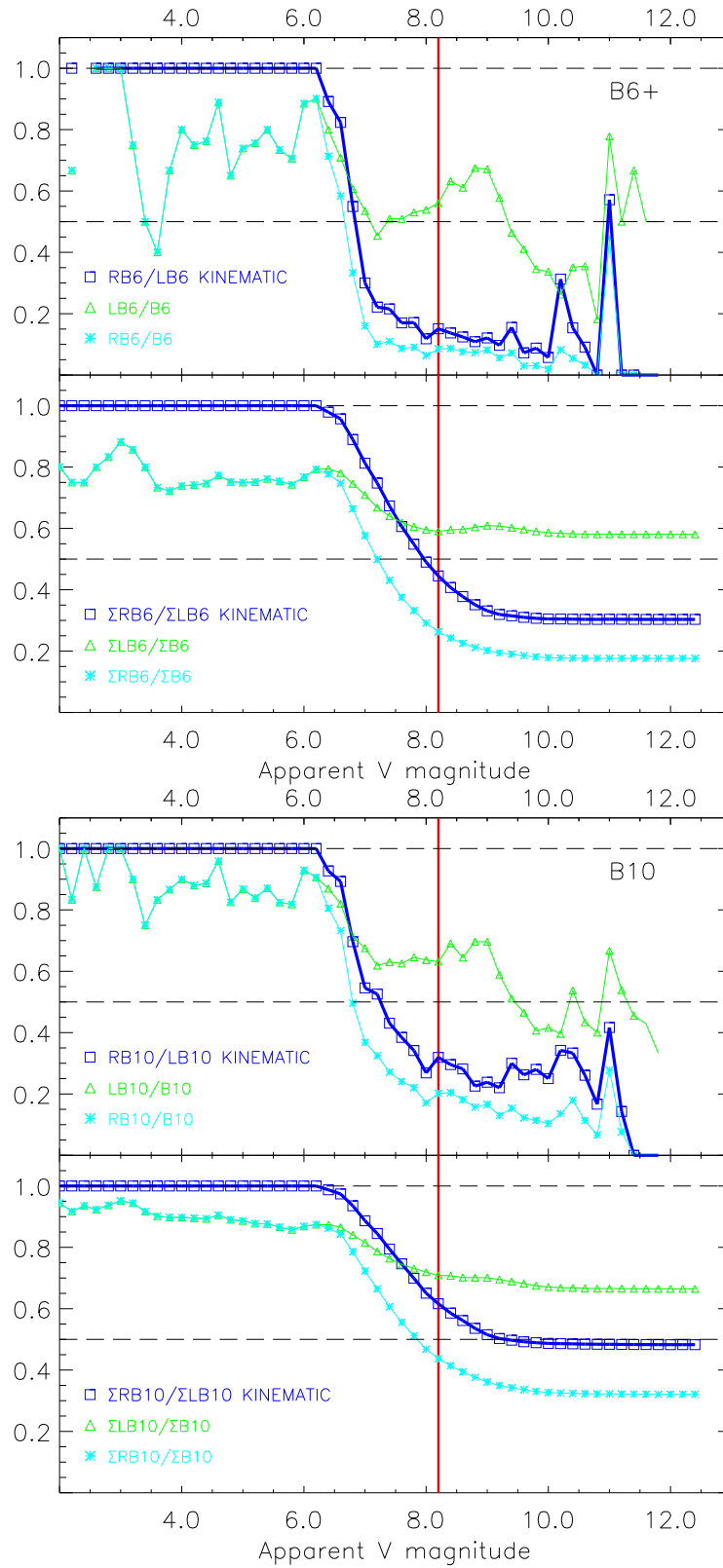
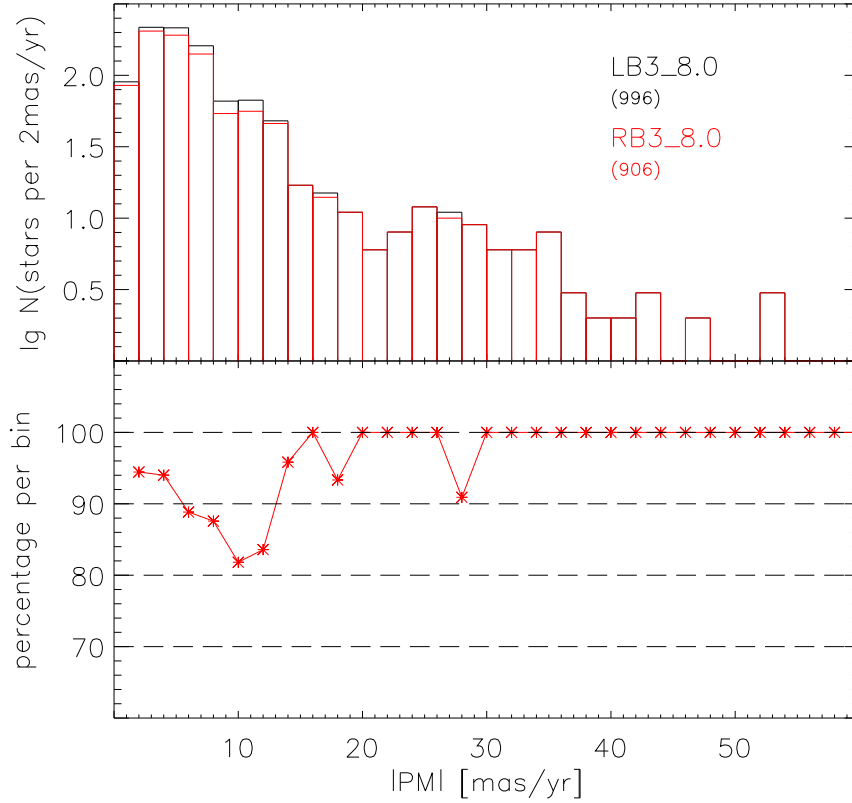Figure 2.5: Same as Fig. 2.4 but for the B6+ sample in the upper panel and B10 sample in the lower.

Figure 2.6: Upper panel: number of stars versus measured proper motion for the *B*3 sample, in 2[mas/yr] bins. Upper, black histogram: stars with full luminosity classification (LB3), down to the limiting magnitude $m_{V,\text{lim}} = 8.0$. Lower, red histogram: all of these stars with radial velocity measurement (RB3-8.0). The numbers in brackets are the corresponding sample sizes. Lower panel: ratio of both histograms. Notice the absence of large kinematic bias.

43

2.4 Final Sample Selection

In this Subsection we define the subsamples used for the kinematic study of this paper. Our aim is to understand the large-scale velocity field of OB stars in the Galactic disk near the Sun, as an approximation to the velocity field of the gas from which they formed. Thus here we remove runaway stars and members of prominent OB associations in the Gould belt. The kinematics of the former reflects star-star interactions, whereas the velocities of the latter may be due to local dynamical features. Then we implement a random procedure to construct a spatially nearly homogeneous sample of OB star tracers for the young star velocity field near the Sun.

2.4.1 Position Cuts and Velocity

OB stars may acquire large random velocities either by being ejected from binaries or by interactions with other stars in their natal star clusters. Typically, stars with random velocities greater than $20 - 40 \, \text{km s}^{-1}$ relative to the local standard of rest (LSR) are deemed to be runaway stars. There are some that even reach random velocities of $\sim 200 \, \text{km s}^{-1}$ (e.g., Dray et al., 2005). As the directions of these velocities will also be random, many OB stars with large distances from the Galactic plane are likely to be runaway stars and to have a broad distribution of velocities.

Figures 2.7 and 2.8 shows that this is indeed the case: this figure presents the U velocity distributions of OB stars in different bins of height $|z|$ above the Galactic plane. Stars close to the plane ($|z| \leq 100 \, \text{pc}$) have a nearly Gaussian U-velocity distribution, while stars far from the plane ($|z| > 400 \, \text{pc}$) have an essentially uniform distribution. At intermediate heights the velocity distribution is a superposition of these two distributions; in the range $100 \, \text{pc} \leq |z| \leq 200 \, \text{pc}$ the Gaussian still dominates, while for $200 \, \text{pc} \leq |z| \leq 400 \, \text{pc}$ the uniform distribution contributes a comparable number of stars. Plots of V- and W-distributions look very similar, so in order to exclude runaway stars from the sample, we will henceforth use only stars with $|z| \leq 200 \, \text{pc}$. Furthermore, we also exclude stars with large heliocentric velocities at small $|z|$. While these heliocentric velocities increase with distance also due to differential rotation, the stars with the largest velocities are again likely to be runaway stars. Having inspected the distribution, we choose a practical approach: after fitting a straight line to the distribution of absolute velocities to obtain the mean $V_{\text{abs}}(D)$, we exclude all stars that have V_{abs} outside the range $V_{\text{abs}}(D) \pm y$, where $y = [(15/2)D/(\text{kpc}) + 30] \, \text{km s}^{-1}$, (see Fig. 2.9).

2.4.2 Gould Belt and OB Associations

Many of the young stars near the Sun as well as nearby HI and H_2 gas appear to be organized in a disk- or ring-like structure called the Gould belt (see Sec. 1.3.2
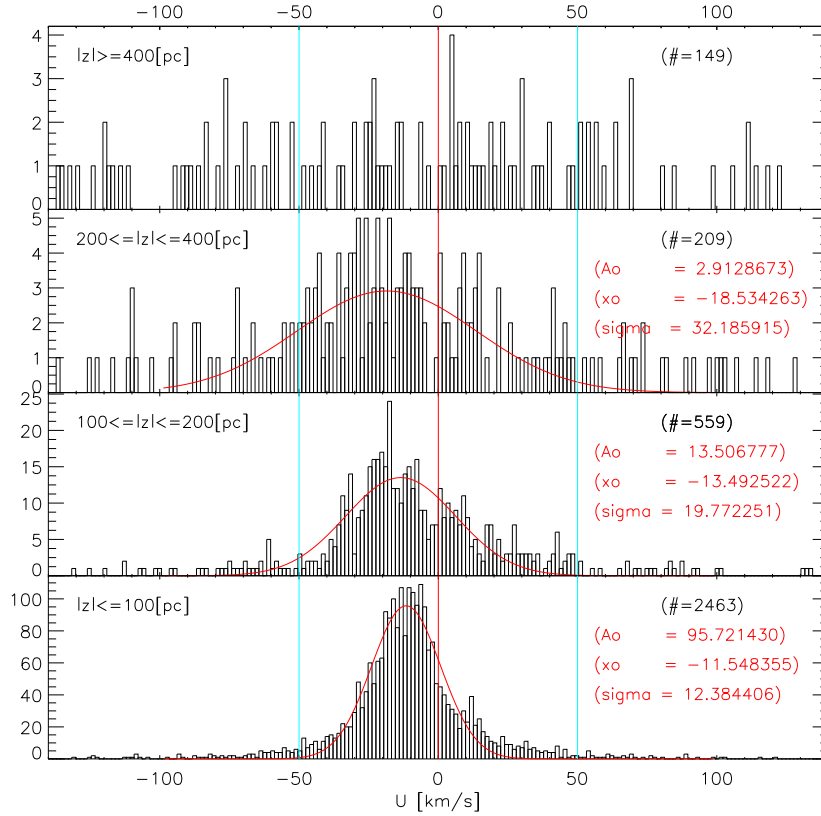
Figure 2.7: Distribution of U velocities for the 3380 stars of the RB10 sample, divided in 4 bins of different height above/below the Galactic plane, $|z|$[pc]. The number of stars in each slice is indicated in the plot. Light blue lines are drawn at ± 50[km/s] to help compare the different distributions, and the red curves show Gaussian fits.

"*Substructures near the Sun*" for a review). The distribution and dynamics of the gas can be described by an expanding cylindrical shell model sheared by Galactic differential rotation, with center ~ 100 pc outwards from the Sun, a height of some 60 pc, semi-major axes 350 pc $\times$ 230 pc, inclined by ~ 17 deg with respect to the Galactic plane. Many of the local OB associations are located on the Belt rim, and the inclination inferred from the OB stars is very similar to that inferred from the gas. The origin of this structure is still not well-understood, but it is a nearby region of intense star formation over the last $30 - 40$ Myr whose dynamics has perturbed also the kinematics of the nearby young stars formed from it. For our purposes, we wish to reduce the influence of the Gould Belt stars on the larger-scale velocity field near the Sun, as much as possible. We have therefore removed 164 stars from our RB10 sample that can be identified as members of the OB associations identified by de Zeeuw et al. (1999), see Figure 2.10, and correspondingly, 43 stars from the RB3-8.0 sample.
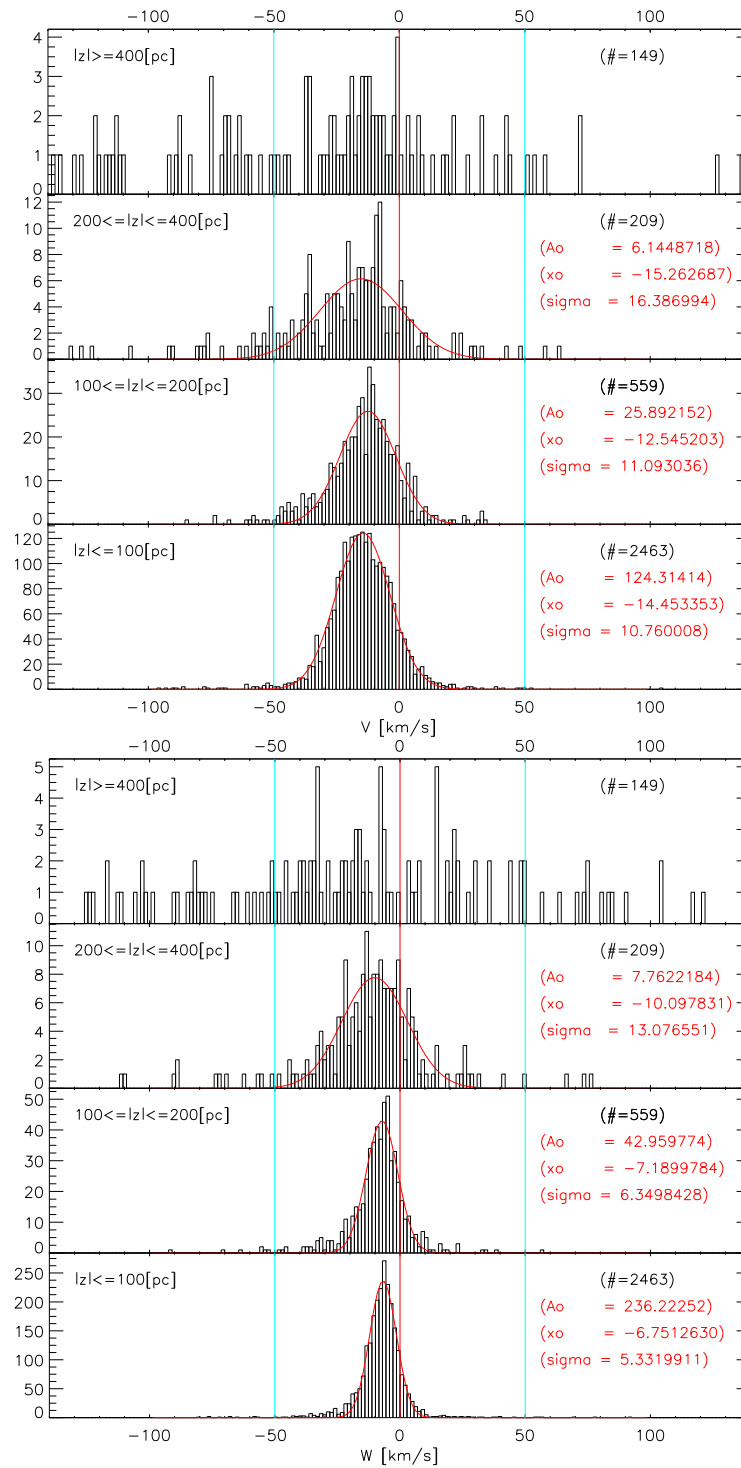
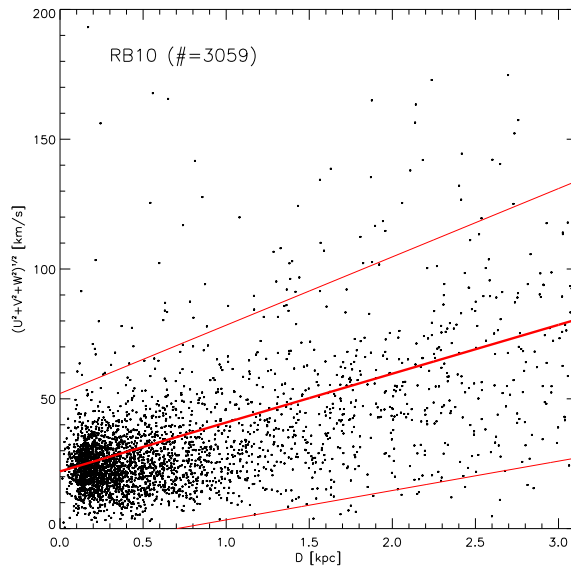Figure 2.8: Upper: Same as Fig. 2.7 but for the distribution of *V* velocities. Lower: Distribution of *W* velocities.

46

Figure 2.9: The velocity amplitude of 3059 RB10 stars out of the ± 2 kpc square region are plotted against their Sun distance D. In the panel are only the candidates with velocities slower ± 200 km s^{-1} plotted, some can reach values higher ± 400 km s^{-1}. The thick middle line is a linear χ^2-fit over all data. (Noticeable by the slight shift upward.) The two border lines show the Runaway star limits given by $y = [(15/2)D/(\text{kpc}) + 30]$ km s^{-1}

2.4.3 Distance Distribution

Most of the later-type OB stars are relatively close to the Sun. Thus in the region of interest, ~ 2 kpc around the Sun, the distance distribution for the RB10 sample stars is very non-uniform. For an analysis of the velocity field, on the other hand, it is advantageous to work with a sample of tracers with an approximately uniform spatial distribution. Also, the fitting algorithm employed here can handle only samples of $\lesssim 800$ stars. We have therefore employed the following random procedure to trim the RB10 sample to a manageable, more uniformly distributed, final sample (hereafter: FB10). We choose a number of rings with radii r_i centered on the Sun, and sort all stars into the annuli between these rings. In each annulus, only those stars are kept for which the modulo function $mod(n, z_i) = 0$. Here we use the Hipparcos-numbers as the modulo function input n to ensure the randomness of the procedure. The Hipparcos (HIP) numbers reflect the right ascension of the stars, so this choice also ensures that in a given ring, stars are selected in an approximately uniform way. We vary the free parameters r_i, z_i in this procedure until the distribution of stars becomes as uniform as possible. Fig. 2.10 shows the positions and velocities of the stars chosen in this way to remain in the FB10 sample, and Figure 2.11 shows that indeed their distance distribution becomes that of a uniform distribution out to $r_u \sim 1$ kpc, falling off only at greater distances. Samples with
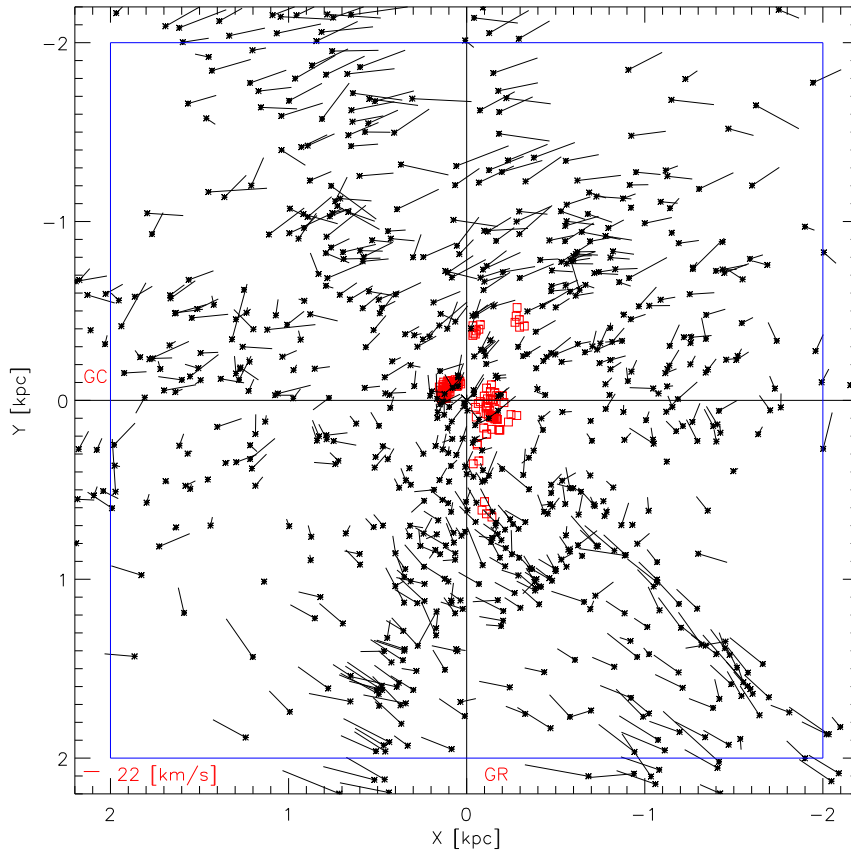
Figure 2.10: Positions and velocities projected onto a $\pm 2.2[kpc]$ square region of the Galactic plane around the Sun, for the stars in the homogenized FB10 sample. This sample contains 728 stars of the 3204 stars in this square in the RB10 sample. The reduction from the RB10 sample to the FB10 sample was done in four steps, (1) taking out 93 runaway stars, (2) taking out 203 stars with $|z| > 200\,\text{kpc}$, (3) taking out 164 stars in OB associations, and (4) using the modulo function approach described in the text to homogenize the distribution in an unbiased way. Red squares indicate where the OB-Associations were located before we excluded them. Some stars belong to more than one of the subgroups taken out in (1)-(3). For reference, the red line shown in the lower left corner corresponds to a velocity of 22 [km/s]. The plotted square is the area within which we fit the velocity with the WW-algorithm. The blue square is the area within which we plot below streamlines through the velocity field; this is slightly smaller to reduce boundary problems. Nonetheless, there remain areas near the border of the blue square where there are no stars. In these regions the WW-algorithm will extrapolate the velocity field, so it cannot be trusted as well there as in areas where there are stars.

larger r_u would be possible only at the price of keeping smaller numbers of stars. For the RB3-8.0 sample no such modulo reduction is used. After removing runaway
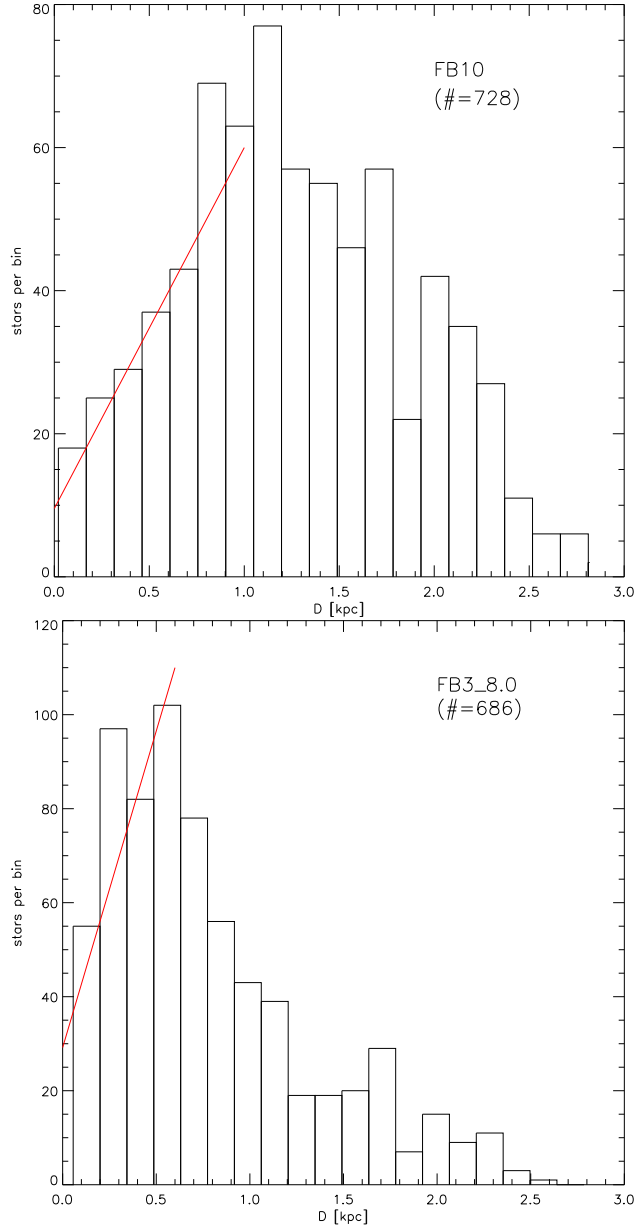
Figure 2.11: Upper: Distance distribution of the stars in the $\pm 2.2[kpc]$ square region from the homogenized FB10 sample, in bins of distance from the Sun. The red line shows a slope of $2 * \pi$ applicable for a homogeneous distribution. For this sample size this can be achieved out to $D \sim 1$ kpc. Beyond $D \sim 1.5$ kpc the number of observed stars decreases too rapidly for this to be possible. Lower: Same as the upper plot, but for the FB3-8.0 sample.

stars, stars at $|z| > 200$ pc, and members of OB associations the trimmed RB3-8.0 sample (hereafter, FB3 sample) is already down to $\lesssim 700$ stars. For this sample, $r_u \sim 600$ pc, (see the lower panel in Fig. 2.11).

49

The FB3 sample of early OB stars (magnitude limited, highly complete, but limited in number and not ideal in spatial coverage) and the FB10 sample of all OB stars (not magnitude limited, strongly incomplete, but larger and with somewhat better spatial coverage) are our best tracers for the Galactic disk velocity field; they will be analyzed in Chap. 4.

Chapter 3

Fitting the Velocity Field

The goal of this work is to relate the velocities of the OB stars in our sample to the average velocity field in the Galaxy near the Sun. Specifically, we assume that the velocities of the Galactic OB stars can be thought of as superpositions of a mean velocity field, that descends from the velocity field of the gas from which these stars were born, with individual velocities whose directions relative to the mean field are randomly distributed. These individual velocities will be due to a variety of dynamical processes occuring at or after the birth of these stars. Our goal is to recover the mean velocity field by fitting a smooth velocity field to the in-plane velocities of all our sample stars.

3.1   Smoothing Algorithm

For this task we use the non-parametric smoothing algorithm and software of Wahba and Wendelberger (1980, hereafter WW-algorithm)), originally developed for analyzing meteorological data. We fit a two-dimensional surface to the data points for each of the in-plane velocity components U, V, as a function of position X, Y relative to the Sun, and thus derive a smoothed velocity field $\{\overline{U}, \overline{V}\}(X, Y)$. Now let $\Phi(\vec{X})$ denote either of $\{\overline{U}, \overline{V}\}(X, Y)$. The WW-algorithm uses thin plate splines to represent a smooth solution $\Phi(\vec{X})$ that minimizes the quantity:

$$\frac{1}{N} \sum_{i=1}^{N} [\Phi(\vec{X_i}) - \Phi_i]^2 \sigma_i^{-2} +$$

$$\lambda \int_{-\infty}^{\infty} \left(\left[\frac{\partial^2 \Phi}{\partial X^2}\right]^2 + 2\left[\frac{\partial^2 \Phi}{\partial X \partial Y}\right]^2 + \left[\frac{\partial^2 \Phi}{\partial Y^2}\right]^2 \right) dX dY. \tag{3.1}$$

where Φ_i, $i = 1...N$ are observations of $\Phi(\vec{X}) + \Delta\Phi(\vec{X})$ at the positions $\vec{X_i}$, with $\Phi(\vec{X})$ representing the mean value and $\Delta\Phi(\vec{X})$ the random component of the velocity components U, V.

In fitting smooth fields to the velocities $U(X, Y)$ and $V(X, Y)$, individual stars are weighted (cf. Eq. 3.1) by their σ_1 velocity errors, which include errors of the proper motions and radial velocities and uncertainties in the distances; see Section. 2.2. The positions of the stars, on the other hand, are kept fixed as determined from their nominal distances. The uncertainties in the fitted solutions that arise from the distance errors are evaluated independently by Monte Carlo simulations.

The degree of smoothness is controlled by the parameter λ; in the following, we use $\Lambda = \log(N\lambda)$. When Λ takes a small value, the derivatives of $\Phi(\vec{X})$ must be large before they influence the fit, so the deviations between the fit and the data will be minimized, and the algorithm will try to fit a very noisy model $\Phi(\vec{X})$ nearly going through all data points. The converse happens when Λ takes a large value, when the fit will try to mainly minimize the derivatives, so $\Phi(\vec{X})$ will be nearly a plane. Intermediate between these two extremes there is a range of Λ for which the algorithm finds a reasonably smooth solution that is also a good representation of the true underlying field. The WW-algorithm includes a cross-validation procedure to determine a suitable value of Λ, but for the sparse data typical in astronomical problems this is usually not very accurate, and the suitable range of Λ must generally be found by Monte Carlo simulations, taking into account the spacing and observational errors of the various data points.

3.2 Monte Carlo Models

For testing the WW-algorithm and adjusting the smoothing parameter Λ, and for understanding the results of applying the algorithm to the OB star data, we will analyse simulated data sets. The general idea is to draw Monte Carlo realizations from a known velocity field and random velocity distribution, so that the resulting artificial data sets closely resemble the OB star samples under investigation. In the first set of simulations, we determine the confidence with which we can recover the original velocity field from these artificial data, as a function of the smoothing parameter Λ. This allows us to determine the optimal value of Λ.

As our standard values for the galactocentric distance and circular velocity of the LSR at the position of the Sun we take

$$R_0 \quad = \quad 8.0 \, \text{kpc}, \tag{3.2}$$
$$V_{c,0} \quad = \quad 220 \, \text{km s}^{-1}, \tag{3.3}$$

but we will explore other values as well. As a realistic velocity field for the solar neighbourhood, we take the often-used ansatz for the circular velocity curve

$$V_c(R) = V_{c,0} * \left(\frac{R}{R_0} \right)^{\alpha}. \tag{3.4}$$

Measurements of the velocity dispersions of nearby stars imply a gently falling rotation curve; we use the ratio $\sigma_\phi/\sigma_R = 0.65$ appropriate for both the bluest and reddest stars (Binney and Merrifield, 1998, Table 10.2, §10.3), so that $\alpha = -0.155$.

A Monte Carlo simulation referring to a sample S with N_S stars is set up as follows. We first pick the positions of N_S stars, either at the exact positions of the sample stars (MCS simulation), or randomly from a homogeneous distribution in the square around the Sun covered by the sample (MCH simulation). Then for each Monte Carlo star at position (X, Y) from the Sun we assign velocities as follows:

1. We compute its position (R, ϕ) with respect to the Galactic Center, and determine the circular velocity according to Eq. 3.4.

2. We define local epicycle axes (x, y), with x radially outwards from the Galactic Center and y along the direction of Galactic rotation; note that these become $x = -X$ and $y = Y$ when the guiding center is at the position of the Sun. From the corresponding radial and tangential velocity dispersions at the position of the star, σ_x and σ_y, we draw epicycle velocities v_x and v_y randomly from Gaussian distributions with dispersion σ_x for v_x and σ_y for v_y.

3. From v_x and v_y we determine the star's epicycle phase $\beta \equiv \kappa t + \psi$, according to

$$\frac{v_x}{v_y} = \frac{\kappa(R_g)}{2\Omega(R_g)} \tan \beta, \qquad (3.5)$$

where κ, Ω are the epicyclic and circular frequencies, and for the moment we take the star's guiding center radius as $R_g = R$.
According to the Epicycle Theory introduced in Sec. 1.3.1.

4. From β and the epicycle equations

$$
\begin{aligned}
x &= A_x \cos(\kappa t + \psi) & (3.6) \\
y &= -A_y \sin(\kappa t + \psi) & (3.7) \\
v_x &= -A_x \kappa \sin(\kappa t + \psi) & (3.8) \\
v_y &= -A_y \kappa \cos(\kappa t + \psi) & (3.9)
\end{aligned}
$$

we determine the epicycle displacements (x, y) by which the star is shifted from its guiding center position.

5. Now we shift the star's guiding center by $(-x, -y)$ and compute the new circular velocity, κ, and Ω. For the same velocities (v_x, v_y) we get a slightly modified β and (x, y), which take the star to a smaller $(\Delta x, \Delta y)$ from it's assigned position (X, Y). This iteration is repeated 4 times, when the star is within maximally $4\,\mathrm{pc}$ of its assigned position (X, Y), and is given the circular velocity at its improved guiding center plus random epicycle velocities corresponding to the velocity dispersions at (X, Y) and a random phase.

6. From these velocities, we finally determine the velocities (U, V) relative to the Sun by transforming into the LSR system and by adding the peculiar velocities

of the Sun in the LSR derived from Hipparcos data (Dehnen, 1998),

$$u_o = 10.0 \text{ km s}^{-1}, \tag{3.10}$$

$$v_o = 5.2 \text{ km s}^{-1}, \tag{3.11}$$

$$w_o = 7.2 \text{ km s}^{-1}. \tag{3.12}$$

Figure 3.1 shows positions and velocities for such an MCS simulation with 742 MC stars. The positions are those of the observed stars in an earlier version of the FB10 sample. The velocities are assigned using the rotation field (3.4) and epicycle dispersions

$$\sigma_x = 14.35^{+0.49}_{-0.4} \text{ km s}^{-1} \tag{3.13}$$

$$\sigma_y/\sigma_x = 0.65^{+0.07}_{-0.06} \tag{3.14}$$

appropriate for solar neighbourhood OB stars (see Binney and Merrifield, 1998; Dehnen, 1998, p.632, Table 10.2). (Here we have ignored the vertex deviation $l_v = 30.2^{+4.7}_{-5.3}$deg of these stars.) The velocity field fitted to the stellar velocities by the WW-algorithm is also shown; it clearly gives a good representation of the mean stellar velocities.

3.2.1 Including Observational Errors

The most important errors in the phase-space coordinates of the Galactic OB stars come from uncertainties in their distances (Sect. 2.2 and Fig. 2.2), but also the proper motion errors can be significant. Below we therefore use MC simulations to assess the effects of these errors, which can be included in the scheme described above as follows. Again, we first assign the (now, apparent) position of a MC star, (X', Y'). Then we draw a Gaussian distributed random value for the error in the distance modulus, using the distance-dependent dispersion from Fig. 2.2. We then convert to an (asymmetric) distance error ΔD, and compute the "true" distance D and position (X, Y) of the MC star. Using the approximate "true" guiding center R_g, circular velocity, κ, etc., at R_g, we place the star on a random-phase position on its epicycle, and iterate until its position is close to (X, Y). Then we compute heliocentric velocities (U, V) appropriate for this star at (X, Y), and convert them to radial velocity and proper motions. Now the MC star is moved back to the apparent, "wrong", distance D' and position (X', Y'), while keeping its radial velocity and proper motions unchanged. Finally, we add Gaussian random observational errors to the radial velocity and proper motions, using the standard deviations of the observed star at the same apparent position (MCS simulation) or the observed star nearest in apparent distance (MCH simulation). Repeating this procedure for many stars generates a MC sample which closely mimicks the observed samples including the effects of errors.
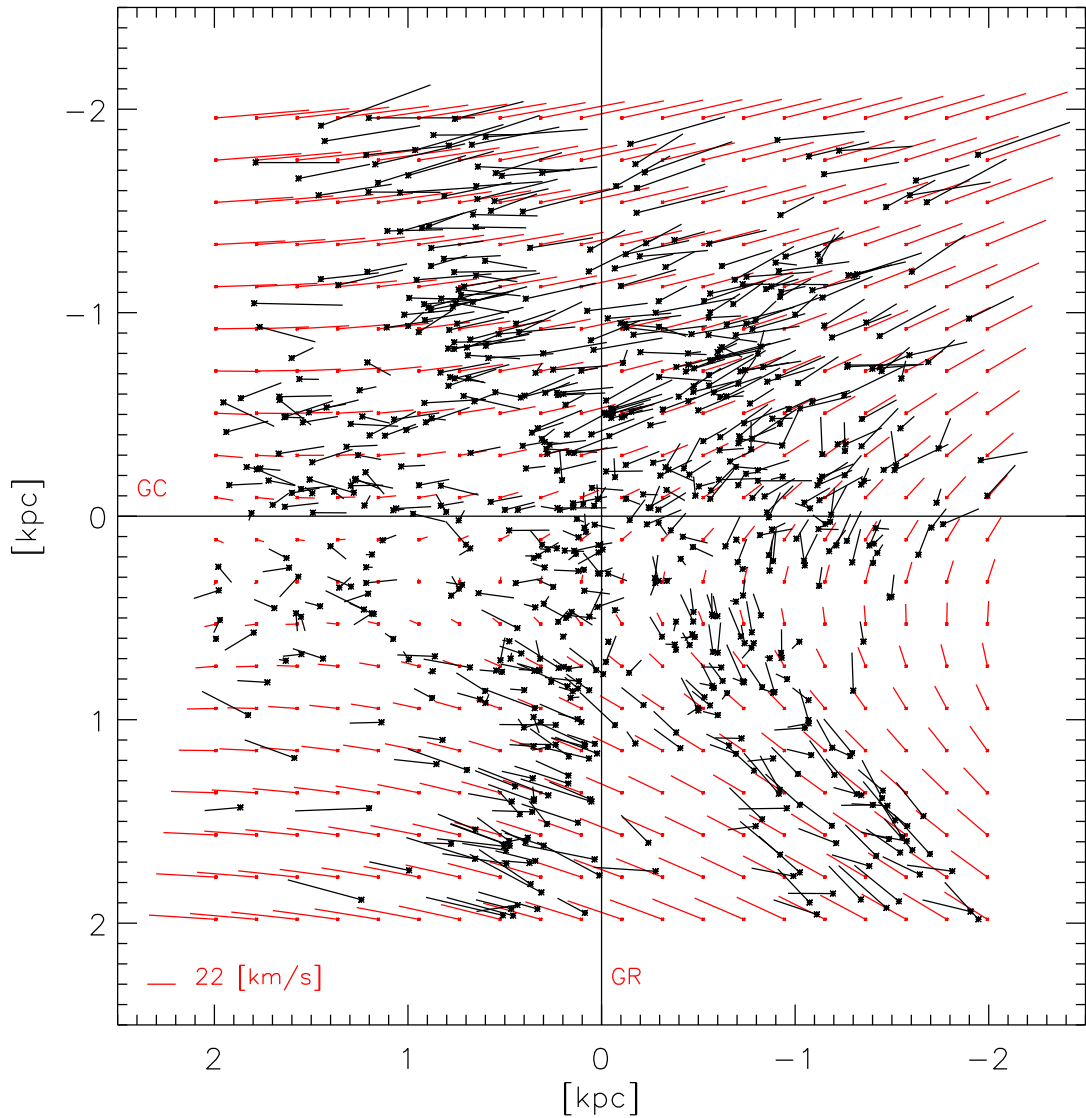
Figure 3.1: Simulation of a sample of 742 stars with a circular orbit velocity field. The positions of the stars are as in the corresponding observed sample, while the velocities are chosen randomly according to the rotation velocity field of Eq. 3.4 and epicycle velocity dispersions as in (Eq. 3.13, 3.14); see Sect. 3.2 (black crosses and lines). The red dots and lines show the velocity field fitted to the simulated stars.
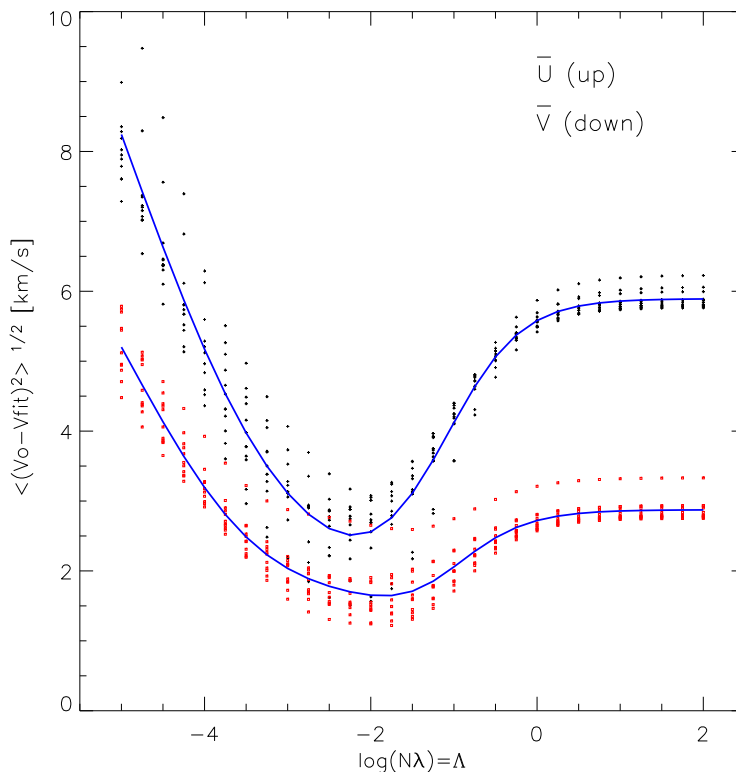
Figure 3.2: *RMS* deviations of fitted Monte Carlo models from underlying circular rotation field, for a sample of 742 stars. Upper curve and sequence of points: *RMS* deviation of fitted mean velocity $\overline{U}$. Lower curve and sequence of points: of fitted mean velocity $\overline{V}$. Each point in this diagram corresponds to one of the 11 random MC models, fitted with a Λ value in the range [-5.0,2.0]. The solid lines follow the mean over the points, as a function of Λ. $\Lambda = -2$ is near the minimum deviation for both velocity components.

3.2.2   Determining Λ

To determine the smoothing parameter Λ in the WW-algorithm, we use 11 MC models as in Fig. 3.1, all for the same sample of 742 stars. For each model, we fit the two velocity components $U(X, Y)$, $V(X, Y)$ independently with the WW-algorithm, for Λ values in the range [-5.0,2.0] in steps of 0.25. The *RMS* deviations of the resulting mean velocity fields from the underlying circular rotation field are plotted in Figure 3.2, as a function of Λ. One sees that the best fits are obtained for $\Lambda \simeq -2$, when the *RMS* deviations in $\overline{U}$ and $\overline{V}$ are $3\,\mathrm{km\,s^{-1}}$ and $2\,\mathrm{km\,s^{-1}}$, respectively. The exact value of Λ is not critical for the fit; e.g., for Λ in the range [-3.0,-1.0] the *RMS* deviations are less than $4\,\mathrm{km\,s^{-1}}$, much smaller than the deviations in the observed samples. Thus we will use $\Lambda \simeq -2$ throughout.

Chapter 4

Results

4.1 The Non-Circular Velocity Field Around the Sun

The upper panel in Fig. 4.1 shows the velocity field fitted with $\Lambda = -2$ in a ± 2.2 kpc square, using the stars in the FB10 sample. A comparison shows that the velocities of the individual stars (black stars and lines) and the vectors representing the fitted velocity field (short red lines) delineate the same basic flow around the Sun as for the circular velocity field shown in Fig. 3.1, but also that there are some noticeable differences. In particular, the streamlines are more curved around the solar position in the two left quadrants of Fig. 4.1 (upper panel) than in the corresponding part of Fig. 3.1.

To make these differences more intuitive, we convert the velocity field of Fig. 4.1 (upper panel) to the Galactic Center reference frame, by subtracting the solar motion in the LSR [eqs. (3.10-3.12)] and adding the LSR rotation for an assumed position of the Sun at $R_0 = 8$ kpc. We then determine streamlines by integrating through the converted velocity field. These streamlines are shown in Fig. 4.1 (lower panel) along with circular flow lines through the same starting points on the upper boundary of a ± 2 kpc square embedded in the fit area. The differences between both sets of streamlines are clearly visible. They are in the sense that the streamlines derived from the OB star velocities are more elongated than those expected from circular orbits, especially for radii $R < R_\odot$. These elongated flowlines reach their minimum galactocentric radii at points that are located approximately on the line that connects the Sun with the Galactic Center.

For a more quantitative analysis of the deviations from a circular velocity field, we draw circles of Galactocentric radii 6.5 kpc, 7.25 kpc, 8.0 kpc, 8.75 kpc, 9.5 kpc through the $(\pm 2 \text{ kpc})^2$ region around the Sun. Along each circle we parametrize position by the angle Ψ_{GC} as seen from the Galactic Center, with the Sun at $\Psi_{\text{GC}} = 0$ and positive Ψ_{GC} along the direction of rotation. Then we decompose the velocity field into radial v_{rad} and tangential v_{phi} velocity components as seen from the Galactic
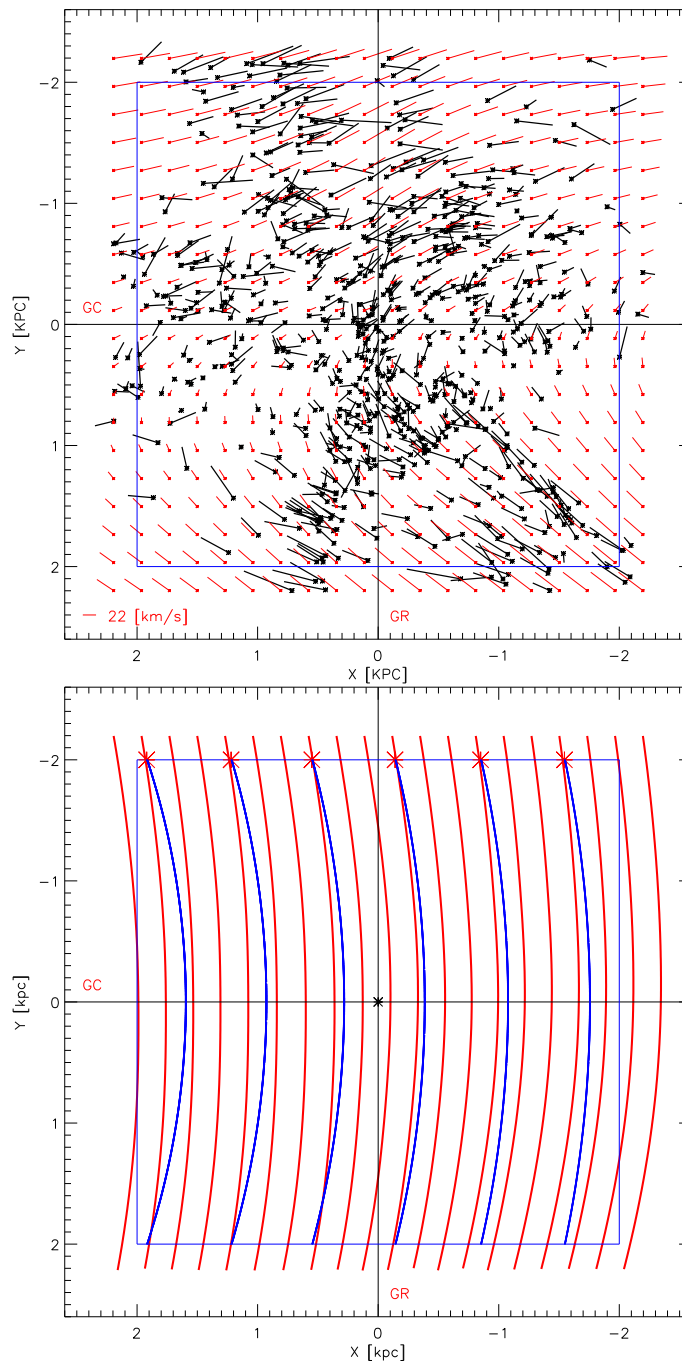
Figure 4.1: Upper: Velocities of the 728 stars from the FB10 sample that fall into a
±2.2 kpc square region around the Sun. The fitted velocity field is shown by the red
lines. The directions of Galactic Rotation (GR) and towards the Galactic Center
(GC) are indicated on the plot; a velocity of 22[km/s] is shown by the bar in the
lower left corner. Lower: Streamlines integrated through the fitted velocity field
in in the left panel, starting at the starred points along the upper side of the blue
square of size ±2.0 kpc by ±2.0 kpc. The direction of motion along these streamlines
is from top to bottom. For reference, the blue lines show circular flow lines with the
same starting points.

Center, and determine v_{rad}, v_{phi} as a function of Ψ_{GC} along each of the five circles. The resulting curves are shown in Figure 4.2. For reference, a circular velocity field with $v_{phi} = V_{c,0}$ would appear as a horizontal line in both panels of Fig. 4.2 (with $v_{rad} = 0$ and $v_{phi} = V_{c,0}$, respectively).
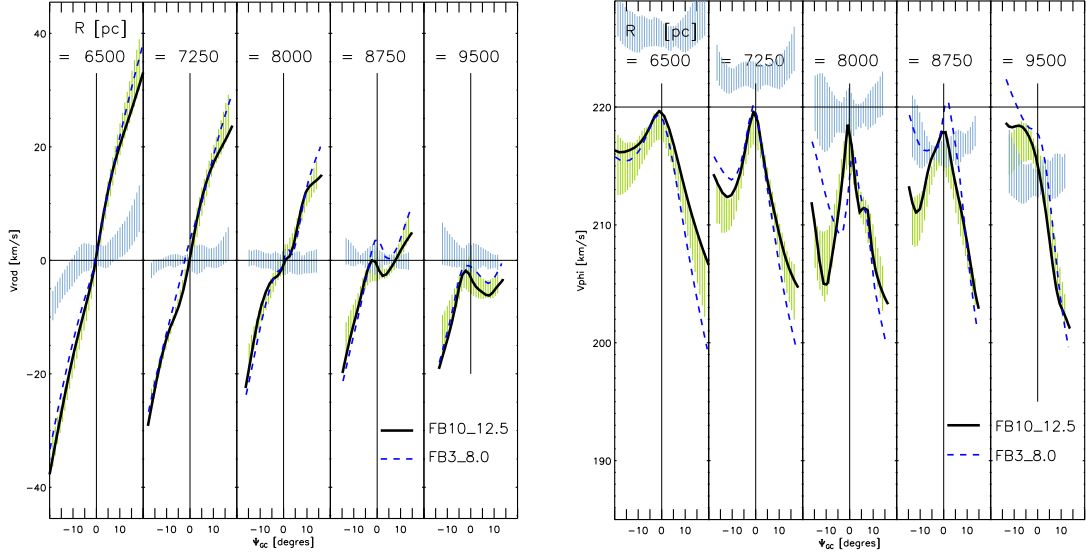

Figure 4.2: Left: Radial velocity component v_{rad} for the velocity fields fitted to the FB10 (full line) and FB3 (dashed) samples, along circles in the Galactic plane. Radii for the circles are given at the top of the figure, assuming $R_0 = 8$ kpc. Position on the circles is parametrized by the angle Ψ_{GC} as seen from the GC; see also Fig. 4.1. Positive values of v_{rad} point away from the GC. The green hatched area shows the range of values obtained from MC simulations, with simulation stars on the exact positions and with the underlying velocity field of the observed FB10 sample stars, and with randomly chosen epicycle phases and observational errors, including distance modulus errors. In each bin, the range from the central 14/20 such simulations (70%, $\simeq 1\sigma$ uncertainty) is shown. The blue hatched area gives the 1σ range of values obtained from MC simulations based on the positions of the FB10 sample but with a circular velocity field. Right: Same, but tangential velocity component v_{phi}. The rotation curve of the assumed circular velocity field has exponent -0.155; the negative slope can be easily seen in the v_{phi}-plot.

We must next assess how significant these deviations from circular streamlines are. This is not trivial because of the complicated way in which errors in the measured velocities, and especially in the distances of the sample stars, influence the solutions for the fitted velocity field. We have thus performed MC simulations of star samples generated with the technique described in Section 3.2.1, which closely mimic the effect of epicycle motions and errors on the observed samples. As model velocity field we have used both a circular velocity field and the elongated velocity field that results from the FB10 sample (Fig. 4.1, lower panel). Both velocity fields we sample either by a distribution of tracer stars at the exact positions of the FB10

sample stars (MCS simulation) or by a homogeneous random distribution of an equal number of stars (MCH simulation). An illustration of a MCH simulation with an underlying circular velocity field and the characteristics of FB10-stars is given in Fig. 4.3.
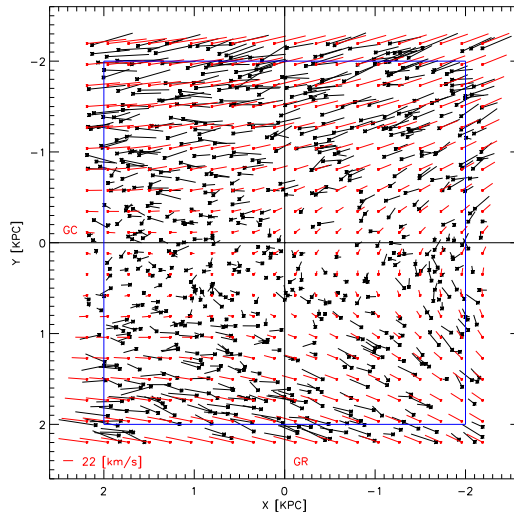

Figure 4.3: MCH-simulation. The characteristics of the observed FB10 sample stars is conserved. The spatial distribution is homogeneous in the ± 2.2 kpc square around the Sun. Errors are chosen randomly according to the stars as described above. Black stars and lines mimic the velocities and star positions out of the simulation and the red dots and lines show the velocity field fitted to the simulated stars.

For each combination, we perform 20 simulations of sample generation and velocity field fit, and determine the mean bias and scatter of the fitted solutions. Fig. 4.4 represent the residuals velocities between the velocity fields obtained from the fit to the simulated stars and the model velocity fields used to generate the simulation data sets. 4 MC-sets are analysed for the two samples FB10 and FB3. In the follow FBX counts for FB10 or FB3, depending the chosen sample. The results of these MC simulations are recapitulated in Fig. 4.4.
From top to the bottom:

1. **Vc_MCS**: an underlying circular model velocity field and stars at exacte positions of the chosen sample.

2. **Vc_MCH**: a circular velocity field and a homogenous random distribution of tracer stars

3. **fO_MCH**: a fitted "elliptical" model velocity field as obtained form the real fitted star sample FBX (Fig. 4.1 (lower panel) illustrate the streamlines of the fitted FB10 stars.) and a homogeneous random distribution of tracer stars.

4. **fO_MCS**: an elliptical model velocity field and MC stars at the exact positions of the FBX sample stars.
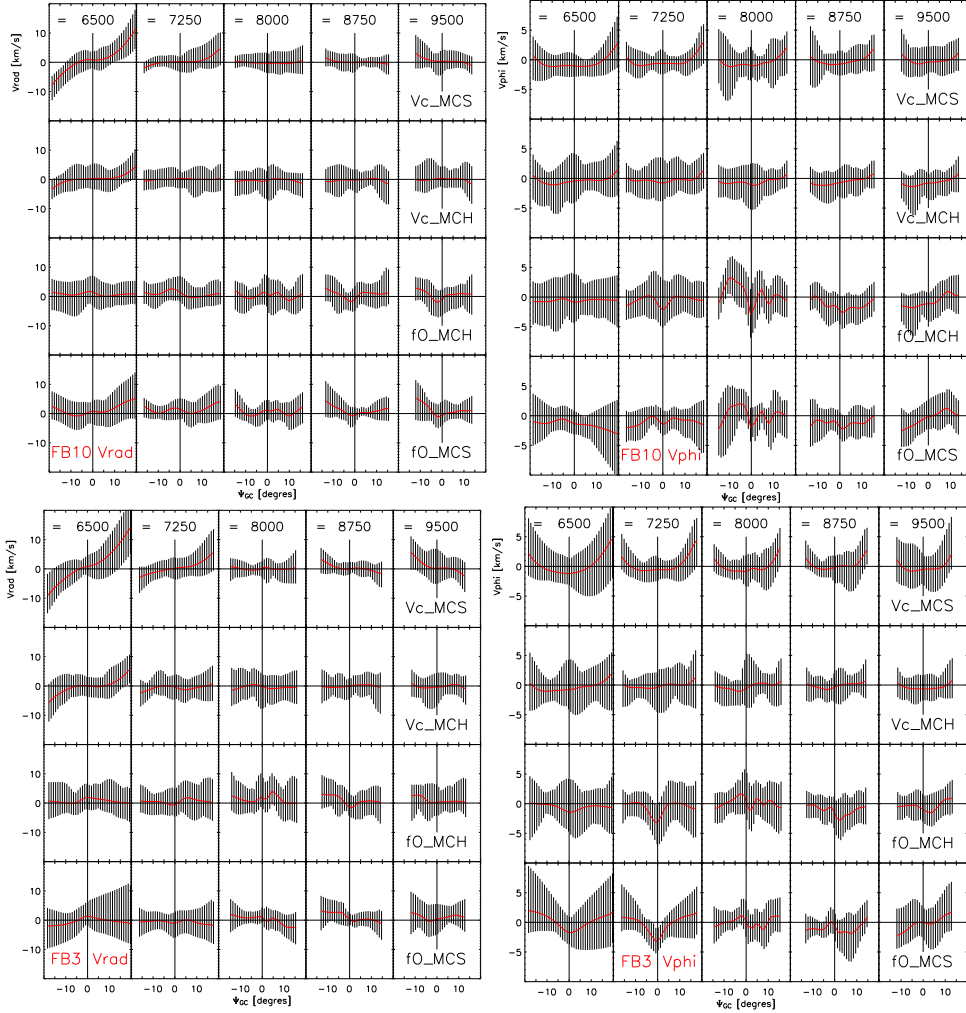

Figure 4.4: In all panels the red line shows the arithmetic mean over 20 simulations, and the gray vertical lines show the total range of values obtained in these simulations. The largest systematic errors $\sim 10\,\mathrm{km\,s^{-1}}$ occur in the top panels, mostly due to lack or sample stars near some boundaries of the $\pm 2.2\,\mathrm{kpc}$ square in which the fits are performed. The typical spread is $\sim 5\,\mathrm{km\,s^{-1}}$. In all panels the fitted basic sample and its component is given in red.

Figure 4.2 shows 1σ error ranges determined from MCS simulations assuming the velocity field obtained from the FB10 sample stars (green hatched regions around the FB10 curves), and also the circular orbit velocity field from Eq. 3.4 (blue hatched regions around $v_{\mathrm{rad}} = 0$ and $v_{\mathrm{phi}} = V_0(R)$, respectively). In both cases the 1σ error range is defined as the range covered by the central 14/20 simulation values of v_{rad} resp v_{phi} in each bin of Ψ_{GC} along the five circles. Error regions based on MCH

simulations are very similar to the ones shown in Figure 4.2. We can now state the main results of our analysis as follows:

1. The mean velocity field fitted to the velocities of OB stars in the local Galactic disk is inconsistent with circular flow lines; the small systematic effect $(0 - 10\,\mathrm{km\,s^{-1}})$ and spread $(\sim 5\,\mathrm{km\,s^{-1}})$ obtained from the MC simulations are too small to explain the inferred non-circular velocities.

2. Inside the solar radius the streamlines are elongated, reaching their minimum galactocentric radii with $v_{\mathrm{rad}} \simeq 0$ and v_{phi} maximal approximately on the line connecting the Sun with the Galactic Center (at $\Psi_{\mathrm{GC}} \simeq 0$).

3. Within the errors, the larger, later type but incomplete FB10 sample and the nearly complete, early-type OB star sample FB3 give the same result. In Section 4.2 below we show that the small differences that are seen in the figure can be traced to the better spatial coverage of the FB10 sample. From now on we will thus mainly use FB10.

4. The modestly falling Galactic rotation curve used for the MC simulations [Eq. 3.4 with $\alpha = -0.155$] is not consistent with the fitted OB star velocity field; see the blue hatched region in the right panel of Fig. 4.2. The maximum v_{phi} velocity on rings decreases by $\sim 3\,\mathrm{km\,s^{-1}}$ from $6.5\,\mathrm{kpc}$ to $9.5\,\mathrm{kpc}$ galactocentric radius. Moreover, because the elongation of the streamlines decreases outwards from $6.5\,\mathrm{kpc}$ to $\gtrsim 8\,\mathrm{kpc}$, the circularly averaged azimuthal velocity may even *increase* with radius in the region probed by the OB stars.

In the following Chap. 4.2, we will show that these results are independent of the fitting geometry, the assumed values of R_0 and $V_{c,0}$, the vertical extent of the sample, etc.

4.2 Model Robustness Tests and Systematic Effects

We have made a number of tests to ensure that the main result shown by the non-circular velocity field in the local Galactic disk, is independent of the (sub)sample used in the analysis, of the assumptions made for the Galactic parameters, and of the technical details of the fitting procedure.

We found that the result is very robust; in particular, it does not depend on

1. the size of the region around the Sun used for the fitting

2. rotation of the region and of the coordinate system in which the fit is made

3. whether we use the nearly complete sample of early-type OB stars, FB3, or the full sample FB10

4. changing subsamples through different modulo functions

5. restricting the sample to lower heights ($|z| < 100\,\mathrm{kpc}$ vs. $|z| < 200\,\mathrm{kpc}$)

6. using only the half of the sample with the better distance estimates

7. the assumed rotation velocity of the LSR

8. the assumed galactocentric solar radius

in the sense that differences to the original sample velocity field in the radial and tangential velocities along circles are consistent within the Monte Carlo errors. In fact, the non-circular nature of the velocity field is slightly accentuated when we use the FB3 sample, or the half sample with the better distances; however, in a way that can be understood in terms of increased systematic errors arising from the less complete spatial coverage. Likewise, in the immediate solar neighbourhood ($\lesssim 150\,\mathrm{pc}$) it is also accentuated if we use only stars with trigonometric distances.

One surprising result is that the line of zero $\mathrm{v_{rad}}$ and maximal $\mathrm{v_{phi}}$ in the fitted velocity field nearly coincides with the line connecting the Galactic Center and the Sun. As Figure 4.5 shows, this is *not* a result of working within the local (X, Y) coordinate system in which the X-axis coincides with the Sun-Galactic Center line. The deviations to the standard FB10 velocity field are small when the fitting coordinate system is rotated with respect to the Sun-Galactic Center line by various angles. The exceptional case (for rotation angle 50 deg) is instructive. The corresponding $\mathrm{v_{rad}}$ and $\mathrm{v_{phi}}$ curves are included in the lower two panels of the figure and the rotated coordinate system superposed on the sample is illustrated in the upper left panel of Fig. 4.5. One sees in how substantial fractions of the positive (left) parts of the circles at $R = 8.0\,\mathrm{kpc}$ and $R = 8.75\,\mathrm{kpc}$ happen to fall in regions without observed OB stars. The velocity field in these regions must be extrapolated from the surrounding regions that do have data points. The extrapolation is done by the WW-algorithm in such a way as to minimize curvature, which in this case leads to large ($\sim 10\,\mathrm{km\,s^{-1}}$) deviations from the standard FB10 velocity field.

In general, samples with poorer spatial coverage lead to larger extrapolation errors, which appear as systematic effects in diagrams such as Fig. 4.5. Similar systematic effects are also seen in the MC results in the $R = 6.5\,\mathrm{kpc}$ frame of the left panel of Fig. 4.2, whereas they are absent in MCH simulations using homogeneous-random samples of stars. See Fig. 4.4 an illustration of the MC error simulations results. We believe that these systematic effects explain the slight accentuation of the non-circular velocity field seen in the FB3 sample velocity field as compared to FB10.

Likewise in the half sample with the better distances (see Fig. 4.6, upper line and middle left panel), the better quality of the distance information appears to be outweighted by the poorer spatial coverage, again leading to a slightly accentuated non-circular velocity field near the boundaries of the fitted region.

Figure 4.6 (lower two panels and the middle right one) illustrates that the fitted velocity field is insensitive to the assumed values for the Galactic constants R_0 and $V_{c,0}$. Decreasing only R_0 for fixed $V_{c,0}$ leads to a slightly accentuated non-circular velocity field, as expected from the changed geometry, but the effect is within the MC errors. On Fig. 4.6 (middle right panel) the spatial dislocation of the circular line is drawn. It shows, that the displacement is only small by varying $R_\odot$ from $7.2, 8.0$ to $8.7\,\mathrm{kpc}$. However, when the angular frequency of the LSR is kept constant while decreasing R_0, the changes in v_{rad} are negligible and the relative changes in v_{phi} are very small (even though the overall amplitude changes, of course).
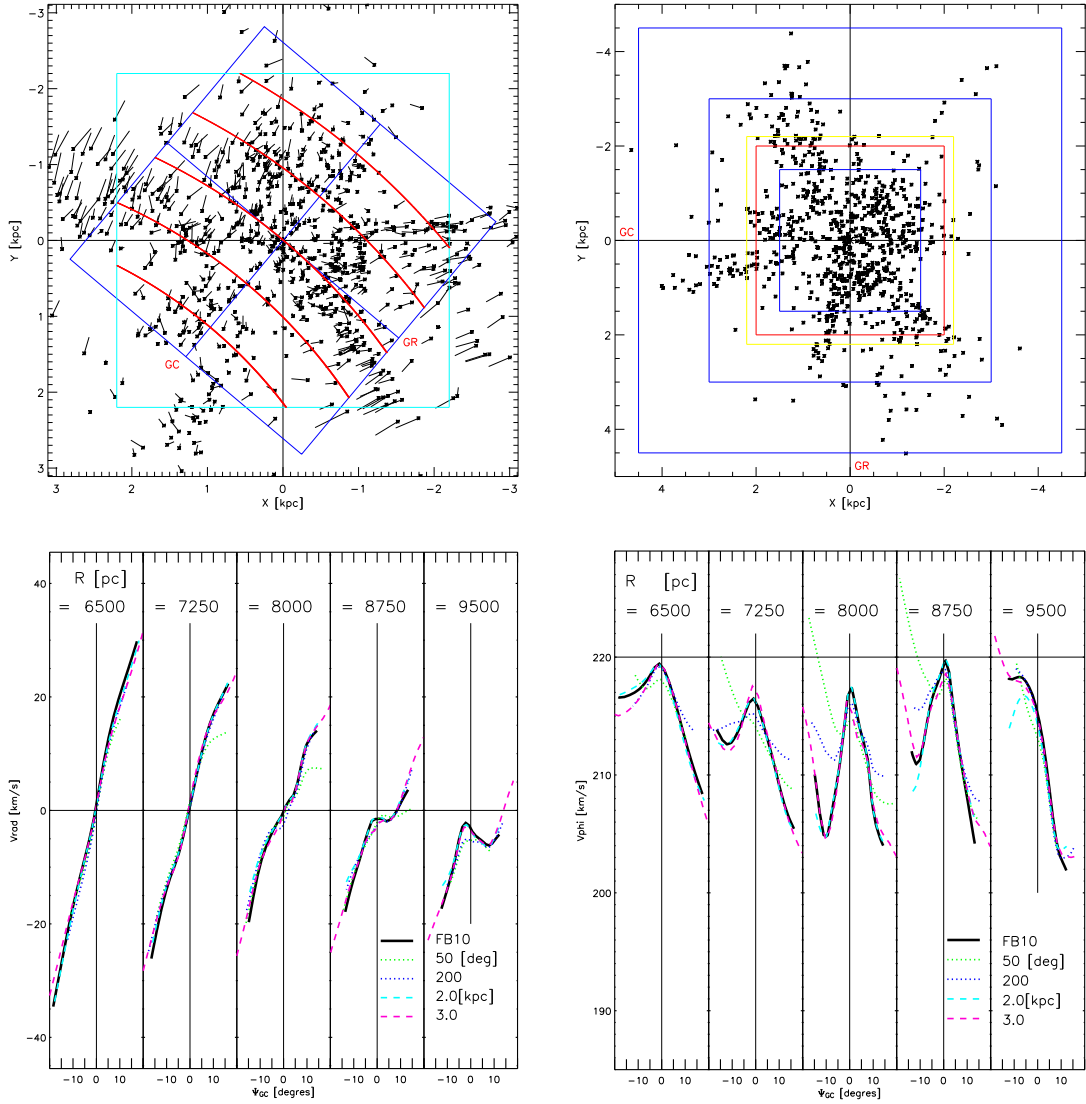
Figure 4.5: Upper left: Geometry of the reference circles in the 50 deg-rotated fit region. The rotated directions to the Galactic Center (GC) and along Galactic rotation (GR) are indicated on the plot. The red lines are the new integrated positions, limited by the turned ± 2.2 kpc star sample (light blue) and the "normally" ± 2.2 kpc square of stars (dark blue). Upper right: Different square sizes for which we fitted the samples; $\pm$ 2.0, 3.0 kpc and ± 2.2 kpc (FB10(1)) samples are represented in in the lower panels. Lower: Influence of enlarging or rotating the fit region around the Sun. Curves show the v_{rad} (left, lower) and v_{phi} dependence on Ψ_{GC} for the FB10(1) sample fitted in squares of varying size around the Sun and in squares rotated with respect to the standard fit area by different angles. Solid line: FB10(1) sample fitted in standard fit area. FB10(1) is similar to the standard FB10, except that a different modulo selection has been used to trim the number of sample stars. Blue- and red-dashed lines: fit area changed to ± 2.0 kpc and ± 3.0 kpc on a side. Dotted lines: fit area rotated with respect to (X, Y) coordinate system by 50 deg, and 200 deg. See text.
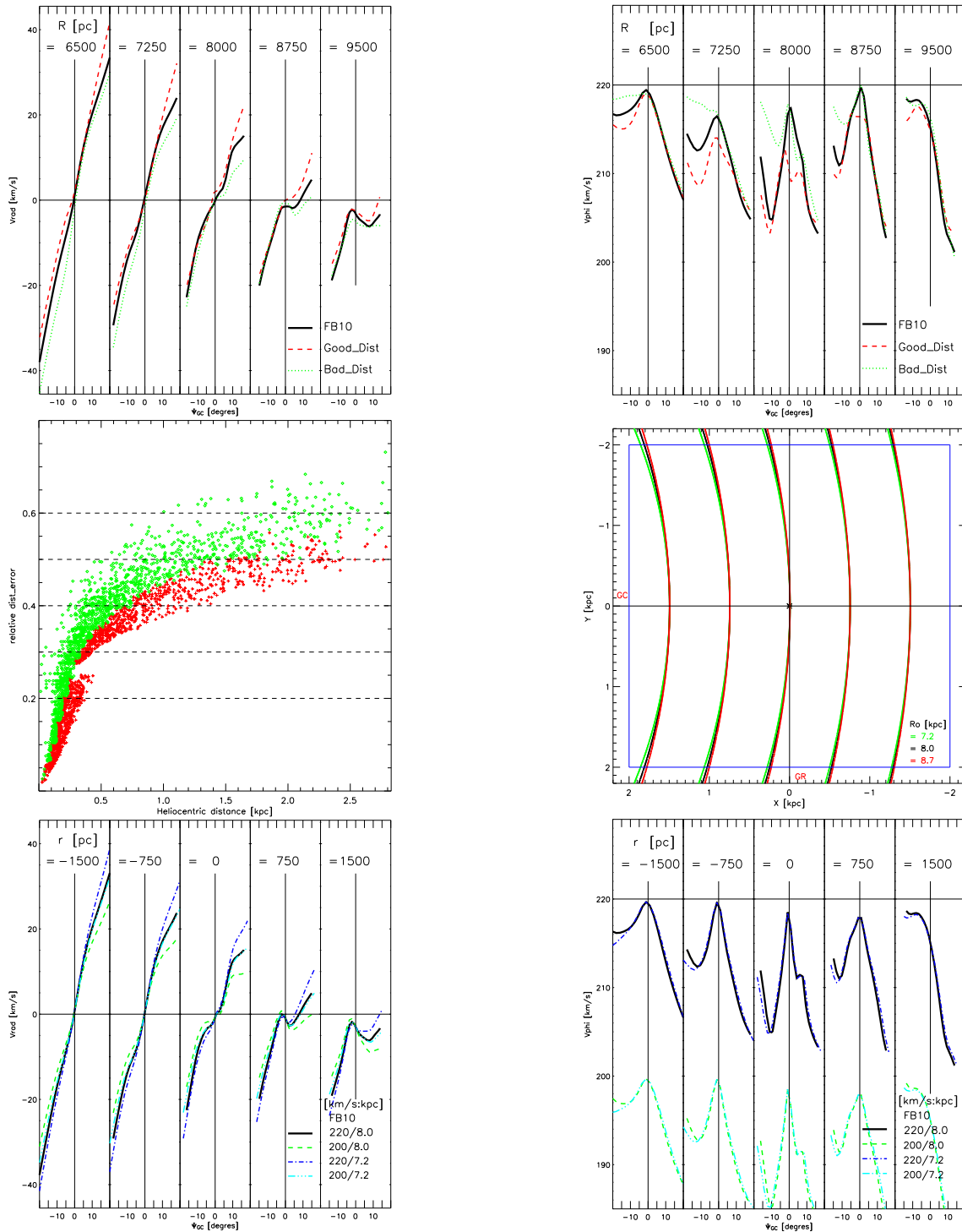
Figure 4.6: Upper: Good to bad Distance test. Middle left: Distance to relative distance error, the colors represent a bin wise splitting of the sample, into a half with smaller (red) distance errors than the bin median and the others (green). The results are represented in the upper panels. Middle right: The different R_0 values make almost no difference in the analyses placement (see text). Lower: Influence of the assumed R_0 and $V_{c,0}$ on the radial velocity component (left) and tangential component (right) of the velocity field.

Chapter 5

Periodic Orbits and Gas Streamlines in a Dynamical Model of the MW

5.1 Orbits in a Rotating Potential

5.1.1 Jacobi Energy E_J

We consider a potential rotating at a constant angular velocity Ω_P[1]. In such a case, energy E and angular momentum L are not conserved. But there is a conserved quantity which expresses the fact that the potential is time-independent in the rotating frame with the known angular velocity. It is the so called **Jacobi integral**:

$$E_J = E - \Omega_P \cdot L. \tag{5.1}$$

The main "modernisation" of this energy is the integration of the *Coriolis force*, and that we talk in terms of an **effective potential**, which is represented by the true potential plus a term for the centrifugal force.

$$\Phi_{eff} = \Phi - \frac{1}{2}(\vec{\Omega}_P \times \vec{r})^2 = \Phi - \frac{1}{2}(\Omega_P^2 R^2). \tag{5.2}$$

The Jacobi energy can be written as

$$E_J = \frac{1}{2}|\dot{\vec{r}}|^2 + \Phi_{eff}, \tag{5.3}$$

where $\dot{\vec{r}}$ is the velocity in the rotating frame.

Figure 5.1 shows an effective potential with a typical *volcano*-shape. Of main interest are the extrema, called **Lagrangian points** in analogy to similar points

---

[1]If the potential describes a MW model with an underlying symmetric mass distribution and a bar feature, then Ω_P represent the pattern speed of the non-axisymmetric feature.
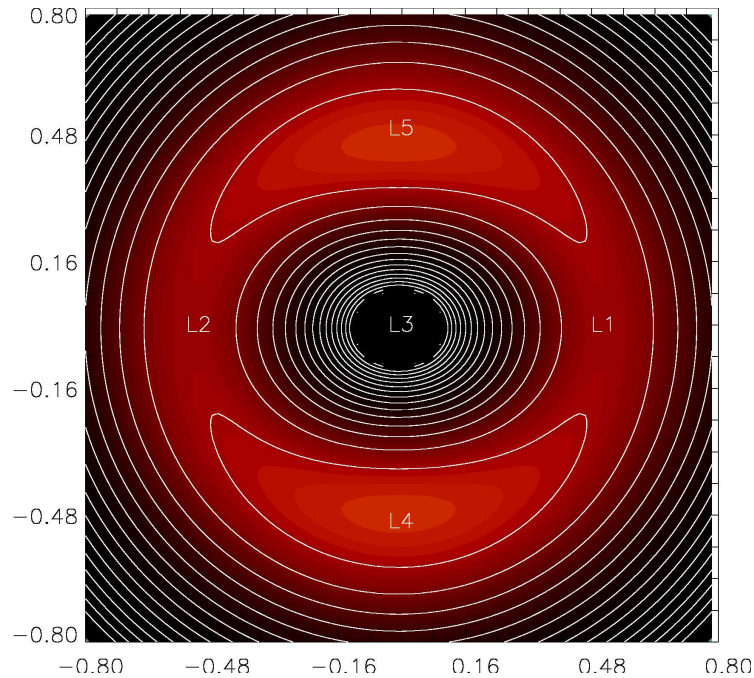
Figure 5.1: Contour plot of an effective bar potential Φ_{eff} in a co-rotating frame, resulting in the typical *volcano*-shape. The Lagrange points are indicated: minima L3; maxima L4, L5 and saddle points L1, L2.

in the theory of the restricted three-body problem. If a particle is located at these positions it would describe a circular orbit co-rotating with the bar. The saddle points L1 and L2, however, are generically unstable, i. e., small radial deviations from these equilibrium positions will become amplified. The minimum L3 at the center is always stable, and stability conditions of the maximum points L4 and L5 depend on the details of the mass distribution. However, in a lot of cases they are indeed stable, especially if the influence of the bar is not too strong.

5.1.2 How to Discover Periodic Orbits?

The shape of the galaxy is determined by allowed orbit families (for a classification see Sec. 5.1.3) and vice versa, therefore orbit analysis is the tool to reveal the nature of the the structure of the galaxy. The exact shape of a stellar orbit depends on a variety of things, including the shape of the galactic potential and the energy and angular momentum of the orbit itself. In general galactic potentials, stellar orbits are not closed, but slowly fill all energetically allowable space as they move through the galaxy.

We compute orbits in a coordinate frame co-rotating with the bar. In this frame, each stellar orbit conserves the Jacobi Energy along its path. Henceforth we will refer to E_J as Energy.
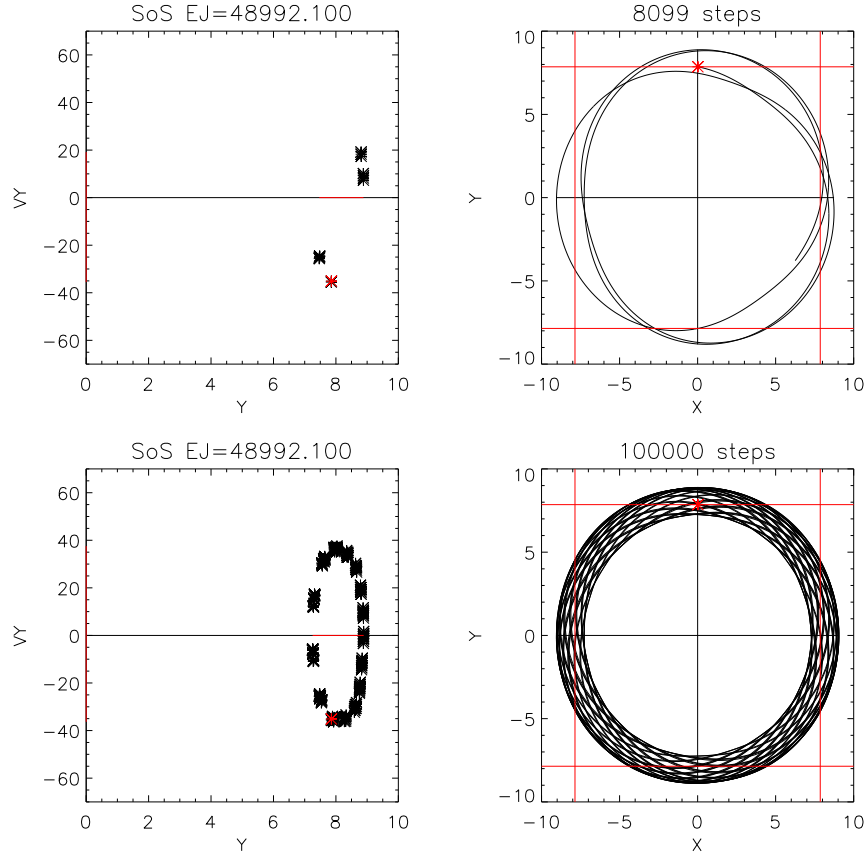
Figure 5.2: Real space path of a loop orbit particle and its corresponding *Surface of Section*. The number on top of the right panels indicates the number of plotted time steps. Represented is a $x1(1)$ loop out of $mod1\_B$. (This kind of model will be described in Sec. 5.4, *Models with different OLR*.)

A strong tool to define such orbits are **Surface of Sections** (*SoS*) which are also called **Poincaré sections**. The idea behind is the following:
To envision the phase space motion of orbits in different potentials there is a 6-dim phase space coordinate system (x, y, z, v_x, v_y, v_z). By introducing the following simplifications the problem gets tractable:

1. Concentration on a motion in a plane,
   $\rightarrow$ 4-dim space: (x, y, v_x, v_y)

2. Since E_J is conserved
   $\rightarrow$ Specification of a given orbit-energy,
   $\rightarrow$ 3 independent variables e. g. $(x, y, v_y; E_J)$

3. Reduced plot
   $\rightarrow$ star-observation only when it crosses the y axis.

69

$$\rightarrow (y, v_y)$$

All this analysis could be done for any choice of corresponding phase space coordinates, but in this chapter we restrict us to use the (y, v_y)-plane.

Fig.5.2 shows an example of an orbit in a rotating frame. Shown in the upper two panels are the SoS (left) and real space location (right) for the first 8'099 integration time steps. The star passed the y-axis four times while conserving its energy along its path. In the SoS we see symbols in black, these are the "y-axis-crossing" informations and the point where the orbit started is given in red. The data memorised by the SoS are the velocity information from the chosen axis v_y and the exact y position where the orbit crossed the axis. The lower panels represent the situation after 100'000 steps. Now the SoS build up a clear ring structure. In the middle of it we find the start conditions for the "wanted" resonant orbit, the theory predicts that there is, in such a peculiar case, an orbit which close itself after one revolution around the GC in the rotating frame. It is called a parent orbit. The advantage of this technique is, that it is much easier to hit start options of an oscillating orbit than it would be for its parent. By iteration, start conditions can be improved step by step.
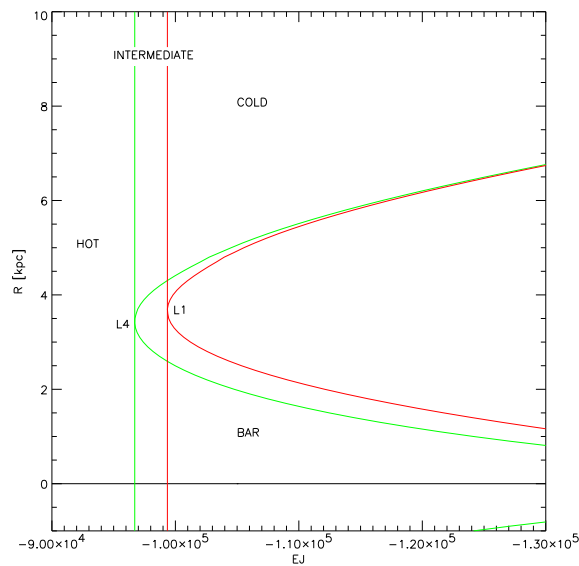
Figure 5.3: Characteristic diagram of mod1_B showing the different regimes of orbits. (This model will be described in more detail in Sec. 5.4, *Models with different OLR.*)

A **characteristic diagram** is a strong tool to represent periodic orbit families. The diagram is built up by the orbit-energies and the specific axis-crossing distance. These two informations fix a periodic orbit in a define potential and its position in the diagram represents also its family membership.
Fig. 5.3 shows the characteristic diagram of mod1_B. The zero-velocity curve (ZVC)

which no orbit can cross are plotted in colors, red is the x-long-bar-axis and green the y-short-bar-axis. These border lines correspond to the case when $E_J = \Phi_{eff}$. The corresponding Lagrange points L1, L4 respectively, are indicated as well, just one as a representer of its axisymmetric partner. There is a slight shift between the two points, so that the co-rotation "region" is not a perfect circle but a ring with a certain width, which is potential-dependent. By drawing vertical lines passing through Lagrange points we define different orbit regimes:

1. Orbits can never be placed inside the region of the solid red (ZVC) line. They can, however, at suitable "shooting"-angles cross inside the region between green and red.

2. Stars with E_J greater than $\Phi_{eff}(L4)$ (green) are free to explore the entire space and are said to belong to the *hot* regime.

3. Stars with $E_J < \Phi_{eff}(L1)$ (red) and $R > R(L1)$ can never penetrate the inner part of the galaxy, and are confined to the outside region. It is called the *cold* regime.

4. The *bar* regime is limited by the radius corresponding to $(L1)$ for stars with $E_J < \Phi_{eff}$.

5.1.3 Orbit Family Classification

Some orbit families are well known and listed in reviews from Athanassoula (1984), Contopoulos and Grosbol (1989), and Sellwood and Wilkinson (1993). The nomenclature used here is taken from Contopoulos and Grosbol and later used by Mühlbauer and Dehnen.

Each orbit family member follows a characteristic behavior. The alignment of orbital elongation with the bar is a main attribute for families. It changes on every fundamental resonance (see section 1.3.3), a behavior akin to the phase reversal of a driven harmonic oscillator as it wanders over a resonance. As a consequence, bars cannot extend beyond the CR region, because the highest populated orbits outside CR are anti-aligned with the bar.

Inside corotation:
The $x1$ orbits are elongated parallel to the bar and are generally thought to support it in self-consistent systems (Contopoulos, 1980). The $x2$ (and $x3$) orbits are elongated perpendicular to the bar and only occur inside the ILRs.

Outside corotation:
At resonances with odd m values (see Tab. 1.4) the main $x1$ family branch off in two orbit families. One is symmetric and one antisymmetric with respect to the bar's minor axis. The resonance with $m = 1$ the so called $(1 : 1)$, creates such a pair of orbit families, which are symmetric reflections of each other. The family which is symmetric with respect to the bar's minor axis is made up of stable orbits. At large

radii, the families develop inner loops, which may penetrate right into the central bar.

$m = 2$ shows a typical change, from orbits inside the OLR $x1(2)$, which antialign with the bar to orbits outside the OLR $x1(1)$, aligning with the bar. The first sub-family $x1(2)$ extends to unstable orbits at larger radii, called $x^*1(2)$.

Around the Lagrange points:

There are families L which are trapped around the (stable) points L4 and L5 on the minor axis of the bar.

In Sec. 5.5 orbits out of different models will be presented. These main families are illustrated in plots. It is interesting to recognise transformations caused by changing the potential or/and the pattern speed of the bar-feature.

5.2 Dynamical Milky Way Models

My thesis is based on a series of models for the MW structure. In the past Englmaier and Gerhard (1999), Bissantz and Gerhard (2002) and Bissantz et al. (2003) evolved and improved these type of models.

The investigation started when the near-IR light distribution in the bulge was mapped with the COBE/DIRBE satellite experiment. An asymmetry between the two sides of the bulge data was found, i.e. the vertical extend of the bulge at positive longitudes was larger than at negative longitudes, which can easily be explained by a tri-axial or bar-like distribution of the bulge (Weiland et al. (1994), Dwek et al. (1995)). For more information see Sec. 1.2.2. Hence, the MW bulge is referred to as "the bar" or "tri-axial bulge" in the literature. Existence of a bar in the MW was first proposed by de Vaucouleurs, and invoked to explain the observed non-circular gas dynamics by Binney et al. (1991).

Unlike distant galaxies, the inner part of the Milky Way is close enough to exhibit perspective effects, i.e. extended objects in the front appear larger than objects in the back. After the necessary corrections for dust absorption (Spergel et al., 1996), the perspective effects combined with symmetry assumptions allow to invert the observed projected light distribution into the underlying 3-dimensional light distribution. In practice, the inversion of noisy data requires the additional assumption of smoothness of the intrinsic light distribution. Binney and Gerhard (1996) developed a modified Richardson-Lucy inversion algorithm with 8-fold symmetry and applied it to the COBE/DIRBE data. They find, that the bar is inclined by about 20° with respect to the Sun with the bar pointing towards us at positive longitudes. A mathematically more complicated approach was taken by Bissantz and Gerhard (2002), allowing for small deviations from symmetry. Inversion of the galactic bulge was shown to be unique by Zhao (2000), if additional independent data is taken into account. Without additional data, there is a degeneracy between bar inclination and axis ratio. In the model of Bissantz and Gerhard (2002) the observed red clump

star distribution along a few lines of sight towards the bulge has been used to break this degeneracy. Red clump stars can be used like standard candles to estimate distances to gain information about the missing third dimension. The result of this study was the 3-dimensional light distribution within the inner galaxy (out to 5 kpc in galactocentric radius).

For a complete mass model of the MW, additional steps are necessary. Bissantz et al. (2003) extended the model beyond the data cube obtained in Bissantz and Gerhard (2002) with a double exponential disk. Assuming a constant mass-to-light ratio and an analytical description of the dark matter component. In addition, a logarithmic spiral arm model for the spiral arms, which has been fitted to the observed spiral arm pattern by Amaral and Lepine (1997), has been included in the model of Bissantz et al. (2003), optionally rotating with a different pattern speed than the bar. The complete mass model has still many free parameters:

- mass-to-light ratio,

- pattern speeds of bar and spiral,

- inclination of bar and spiral pattern with respect to the Sun, and

- dark matter halo parameters.

In order to estimate values for all these parameters gas dynamical models have been used to compare with the observed gas kinematics in the MW. Bissantz et al. used a multipole expansion method developed by Peter Englmaier for calculating the gravitational potential of the rigidly rotating bar and spiral potential. All non-axisymmetric density variations beyond some cutoff radius $R_{cut} = 3.5$ kpc (Bissantz and Gerhard, 2002) have been attributed to the spiral pattern, while density variations inside this radius are considered part of the bulge/bar. This allows separation of bar and spiral pattern as well as experiments with modified relative strength of spiral and bar perturbation. The numerical scheme used for calculating the hydrodynamics was "Smooth Particle Hydrodynamics" (SPH) in 2 dimensions based on a code originally developed by Steinmetz (1996).

The modeling depends to some extend on the assumed solar galactocentric radius $R_\odot$ and LSR velocity $V_\odot$, but we do not treat them as free parameters. Instead we assumed the values $R_\odot = 8$ kpc and $V_\odot = 220$ km s^{-1}, which are in good agreement with resent studies of Reid (1993) and Eisenhauer et al. (2003) for $R_\odot$ and Hipparcos data as analyzed by Feast and Whitelock (1997).

The mass-to-light ratio has to be found iteratively by fitting the gas dynamic model to the observed gas dynamics of the MW for each set of parameters. However, in practice only small variations on the percent level are found between models.

Approximative values for the pattern speed and inclination of the bar have been obtained in Binney and Gerhard (1996) and Englmaier and Gerhard (1996). Bissantz et al. (2003) studied the dependency on the spiral pattern speed and inclination

angle. They found evidence, that the spiral pattern does indeed rotate independent of the bar by looking at the transition region where the gas flow is influenced by both patterns.

The importance of the dark matter halo has been established to be rather low inside the solar radius. Only at around 9 kpc galactocentric distance, the dark matter halo starts to dominate the rotation curve (in preparation: Englmaier & Gerhard 2006).

5.3   Periodic Orbits and Streamline Plots

The models I use are based on gas dynamics in the MW. My fitted streamline plots are made up with an OB stars sample. These stars are young objects, so we make a first assumption, that recently born stars still behave similar to the gas they got born in. They did not had time to degenerate kinematicaly from the material. In a next assumption we suppose, that the gas takes the way of the least resistance, it tries to avoid shocks. So we predict that it moves mainly on simple looking orbits, orbits with no loops and a smoothed shape.

In Sec. 5.4 I worked out four different models and analysed their periodic orbits. The output are orbit plots which I will introduce in the next paragraph. The streamline plot of the OB stars (see Sec. 4.1) will be recapitulated short afterward.

5.3.1   Orbit plots

With the technique described in the preceding sections, my code (*orbit_nox.F*) helps to define closed orbits in a rotating potential. The basic code, which iterates data in surface of section (SOS) as long as it can find a resonant parent (see Fig. 5.2), is basically written by Peter Englmaier who used it for the x1 and x2 orbit search. (For the nomenclature see Sec. 5.1.3 *Orbit Family Classification.*). I modified and developed the code further and adapted it to orbit-search outside the bar and mainly in the co-rotation regions. The used potentials, modified and evaluated by Peter Englmaier) (see Sec. 5.2), are implemented into the code routine.

A descriptive output of the program are the orbit plots. Figure 5.4 illustrates a x1(2) orbit out of the mod0_B model. Detailed informations about the chosen orbit and its model are given in Sec. 5.4.
 In the plot the bar lies on the x-axis. In green the CR and the OLR are sketched. Thiner blue lines are guidelines to the eye helping to define the ellipticity of orbits plotted in black or seldom in red. The guidelines start at 5 kpc and continue in 1 kpc steps up to 9 kpc. The blue square inclined by a 20° angle and at a GC distance of 8 kpc represents the observed field we discussed before. The solar region positioning is just an assumption based on well known values out of the literature.
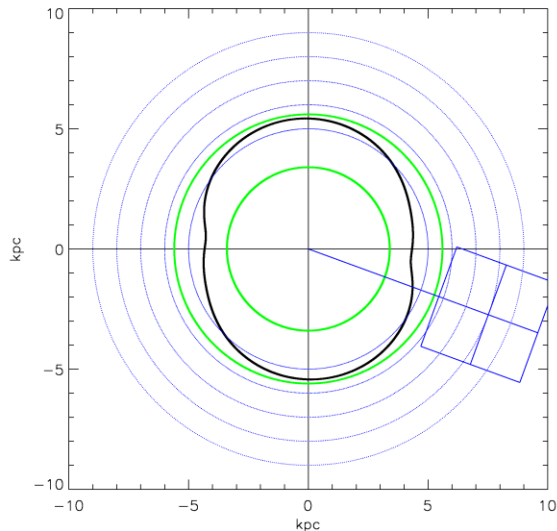
Figure 5.4: An x1(2) orbit out of the *mod0_B* model

The bar turns anti-clockwise and so a prograde rotating orbit is even faster than the bar and turns into the same direction. A retrograde is slightly slower than the bar and so it points into the clockwise direction. It is important to recognise that such an orbit, in an inertial frame, rotates counterclockwise like the bar as well. The x1(2) and almost all my defined orbits near the OLR behave like this. In the characteristic diagrams their direction of rotation *in the rotating frame* is mentiond, a retrograde orbit is signed with a cross, a prograde with a square.

5.3.2 Streamlines of the OB Star Sample

Unfortunately the OB data analysis frame and the periodic orbit output do not have the same orientation. The non-circular OB velocity field around the Sun we fitted in Sec. 5.5 has to be adapted by mirroring along the x axis. I even rotated the sample by 20° to represent a 1*to*1 image out of the orbit plots.

The big star symbols indicate the start position of a star. So the velocity vectors are pointing all into the counter-clockwise direction.

As a reminder: The differences between both sets, the streamlines (red) and the underlying velocity field (blue) are clearly visible. They are in the sense that the streamlines derived from the OB star velocities are more elongated than those expected from circular orbits, especially for radii $R < R_\odot$. These elongated flowlines reach their minimum galactocentric radii at points that are located approximately on the line that connects the Sun with the Galactic Center. At $R > R_\odot$ the streamlines seem to be slightly turned forward.
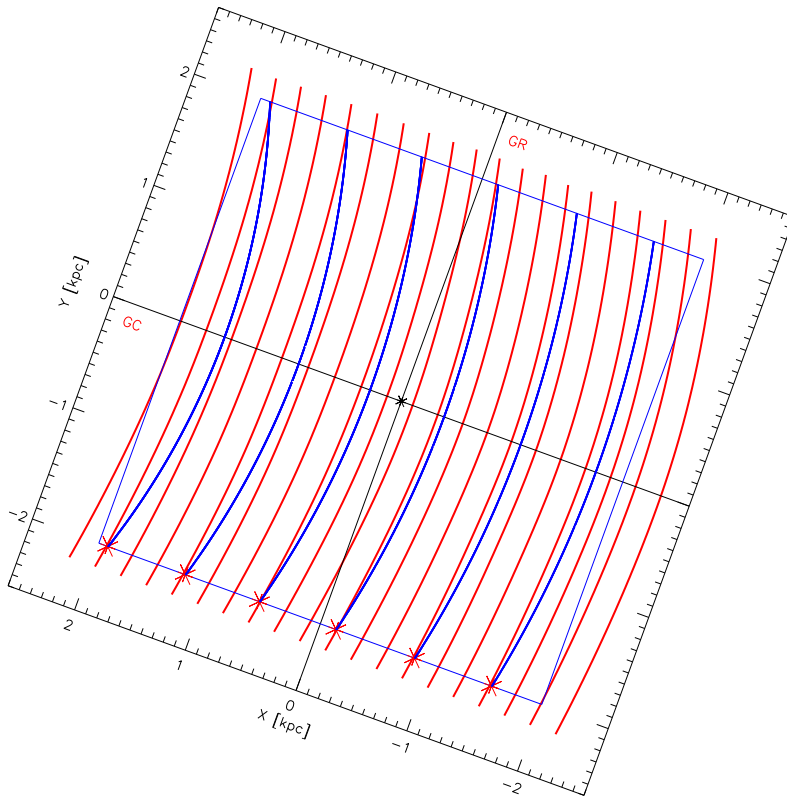
Figure 5.5: The non-circular velocity field of FB10 stars transformed with an axis mirroring ($y \equiv -y$) and a rotation of 20°. The new orientation and inclination shows the field in the same way as the orbit plot. Stars are "flying" from the bottom to the top in the same direction as the bar rotates.

5.4 Models with different OLR

We started our analysis with an improved model out of Bissantz et al. (2003). In Chap. 5.2 the characteristics of such a model are explained. *mod0* does not incorporate a halo, but has a bar (about four times stronger as in Mühlbauer and Dehnen (2003)) and four equal spiral arms. There are two options to adapt the potential into our code. As $R_{cut} = 3.5$ kpc splits the asymmetric potential, it is possible to work with the full potential including bar and arms, or to neglect the arm potential outside this radius.

- *mod0_B* represents a model with a bar and small spiral arm extensions which are inside R_{cut}. (They are at the upper left side of the bar-end[2] and at the lower right side.)

- *mod0_BA* incorporates both bar and arms.

In a next step we shifted the OLR from 5.6 kpc to 7.2 kpc. This value is motivated by the work of Dehnen (2000), in his modeling he predicts $R_{OLR} = 0.9\,R_\odot$ as an upper value. The basic characteristics of the model are the same as before, but by adding a halo component and by a slight shift of Ω_p from 61.4 Gyr^{-1} to 53.74 Gyr^{-1} the resonances are replaced further out. In Fig. 1.11 we can see the resonance diagram of *mod1_BA*. With the same splitting of the potential we create

- *mod1_B*

- *mod1_BA*

The main parameters of the models are shown in Tab. 5.1. In either case we let run

	mod0	mod1
R_{CR}	3.4 kpc	3.9 kpc
R_{OLR}	5.6 kpc	7.2 kpc
Ω_{bar}	61.4 Gyr^{-1}	53.74 Gyr^{-1}

Table 5.1: Parameters of orbital models

the code with a single pattern speed for both asymmetric components $\Omega_{bar} = \Omega_{sp}$.

5.5 Results

The orbit plots are grouped page by page, by its model belonging.
mod0_B fills the first two plot reserved pages, mod0_BA the next one and mod1_B (left) and mod1_BA (right) are sharing the last. Each page is build up in the same

---

[2]The orientation is the same as in Fig. 5.4.

way. In the upper line the model corresponding characteristic diagram is shown, where Orbits found by checking the y-axis are plotted in blue and red is the color for the x-axis candidates (see Sec. 5.1.2). Squares indicate if an orbit turns retrograde in the rotating frame, and crosses signalise a prograde movement. In Fig. 5.6 (upper left panel) mod0_B has its main orbit family names indicated. So it is possible to bring orbit plots (labeled in the upper right corners of the panels) and families into relation. See Sec. 5.1.3 for details about the nomenclature.
Then the following panels show representatives of the corresponding orbit families.

The orbits of our main interest are x1(2) (upper right) and x1(1) (middle left). Around resonances two stable periodic orbit families with different elliptical orientation can exist in the same area, see Fig. 1.12. Our streamline analysis gives justified presumptions that this is the case in the nearby solar neighbourhood.

Our analysis is based on the following assumptions, namely:

- Gas moves on closed periodic orbits.

- OB stars behave similar to the gas they got born in.

Additionally we know by Bissantz et al. (2003), that dynamical models predict that two different pattern speeds for the arm- and the bar-feature ($\Omega_{bar} \sim 60\,\text{Gyr}^{-1}$ and $\Omega_{sp} \sim 20\,\text{Gyr}^{-1}$) reproduce the $l - v$ diagram nicely (see Fig. 1.5 for an explanation of this kind of diagrams and Bissantz et al. (2003) for the explicit data and similar results.). Here we use only *one* pattern speed for both asymmetric features (see Tab. 5.1). Another problem occurs, if in our region of interest a crossing of streamlines is expected (see e. g. Fig. 1.12). In the crossing point the information of two different streams would be smeared out, and with our method of fitting, we would just find one averaged stream out of the two. Dehnen's sample is strongly restricted to the solar neighbourhood. See Sec. 1.3.2 *Kinematics in the Solar Neighbourhood*. There the observed star density is highest and it is possible to make a local u-v diagram statistic. Not so in the outer parts of our FB10 sample. A comparison of our nearby solar region data ($R_\odot < 300\,\text{pc}$) with his results showed the same substructures, as expected as we are using similar data sources. An advantage of our star sample is that the data positioning reaches areas placed further out. Our space coverage is much more comprehensive than Dehnen's. With our method we see $\gtrsim 12\%$ of one cycle. (The main restriction for such an orbit analysis is given by the sample completeness of available observed data.) We made many tests (see Chap. 4) to verify our results. The FB10 streamlines out of the $\pm 2.2\,\text{kpc}$ field give the impression to distinguish between two orbit families (see Sec. 5.3.2).

Our interest is mainly focused on the following questions:

- Do periodic orbit families (out of the gas) in general reproduce the wanted characteristics?

- Under which conditions can we have such orbits in the nearby solar region?

In Fig. 5.6 we see the orbit produced by mod0_B. The upper right and the middle panel show the families x1(2) and x1(1). There we see that the characteristic of our OB streamlines in the inner region ($R < $ R$_\odot$), corresponds to the main characteristic of the x1(2) orbit (elongated part parallel to the bar's minor axis). But there are still many not confirming aspects. One are the dents[3] along the x-axis and a second one is the wrong inclination[4] corresponding to the observed field.
Another family seams interesting (Also mentioned in Dehnen (2000) as possible representatives.); the 1:1 orbits. They could help to explain the forward shift of OB streamlines with $R > $ R$_\odot$. See Fig. 5.7 upper left panel, the downward shifted orbit. But our main interest belongs to the x1(1) and x1(2) families. When we look closer to the innermost orbits (Fig. 5.6, the two lower panels) out of these two groups, we can see a slight deviation from the bar symmetry along the x-axis. These slight turns can be explained by the small arm extensions included in the R_{cut} region. And also the dents of the x1(2) orbit can be explained by the influence of mass in the nearby region.
Going a step further in modeling and including the arms, we see in mod0_BA that these mass effects are even stronger and also the declination of the innermost x1(1) orbit is more extended. It turns upward corresponding the arm potential in this region. In Figure 5.7 these aspects are highlighted in red. It is to recognise, that in mod0_BA new families, which reflect symmetries of higher order than the mod0_B orbits are found (Fig. 5.7, lower right panel).
With mod1_B and mod1_BA we want to implement this knowledge. First we shift the OLR outward to bring the main families closer to the solar region. mod1 has its OLR at 7.2 kpc and so the x1(1) and x1(2) families reaches the FB10 region. We see dents do not exist anymore in the x1(2) family (compare Fig. 5.6 upper right panel and Fig. 5.9 lower left), the mass disturbances have less influence. The x1(2) orbits are elongated perpendicular to the bar's major axis and look smoothed. The x1(1) are parallel orientated to the bar as expected. An effect much more important can be seen in the middle panels of Fig. 5.9. Here we represent the x1(1) orbits for mod1 once with arms (right, mod1_BA) and once without (left, mod1_B). It is obvious, that the presence of arms turn the x1(1) orbits into the direction of the Sun. The bar symmetry can be broken. This could in a first step explain the orientation of our OB streamlines, where the elongated flowlines reach their minimum galactocentric radii at points that are located approximately on the line that connects the Sun and the galactic center.

---

[3]Gas prefers smoothed orbits.
[4]Our fitted streamlines are orientated along the Sun-GC line.

I think this result is a small step into the right direction. From Mühlbauer and Dehnen (2003) we know, that the effects produced by a bar alone are two small ($\pm 5\,\mathrm{km\,s^{-1}}$ at maximum). We found in the OB sample much higher velocity values (up to $\pm 30\,\mathrm{km\,s^{-1}}$). And additionally the bar alone predicts orbits, which are bar symmetric, but we found "rotated" ones. So it is obvious that the bar alone can not explain the features found. By including the arms we could get a small step closer to explain the observed data.
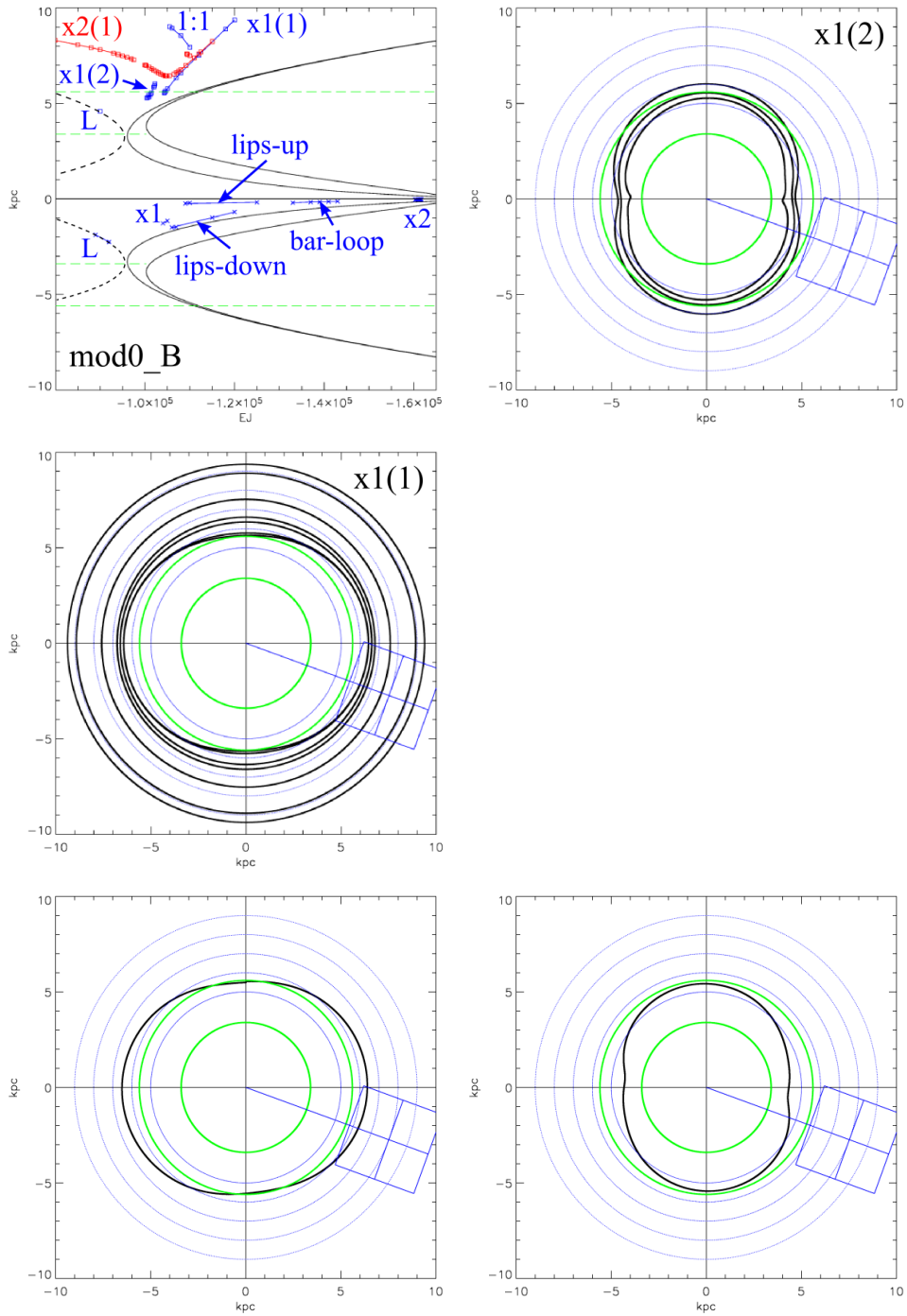
Figure 5.6: Upper left: characteristic diagram of mod0_B Upper right: x1(2) family members Middle: x1(1) family members Lower left: nearest x1(1) to the bar Lower right: nearest x1(2) to the bar

81
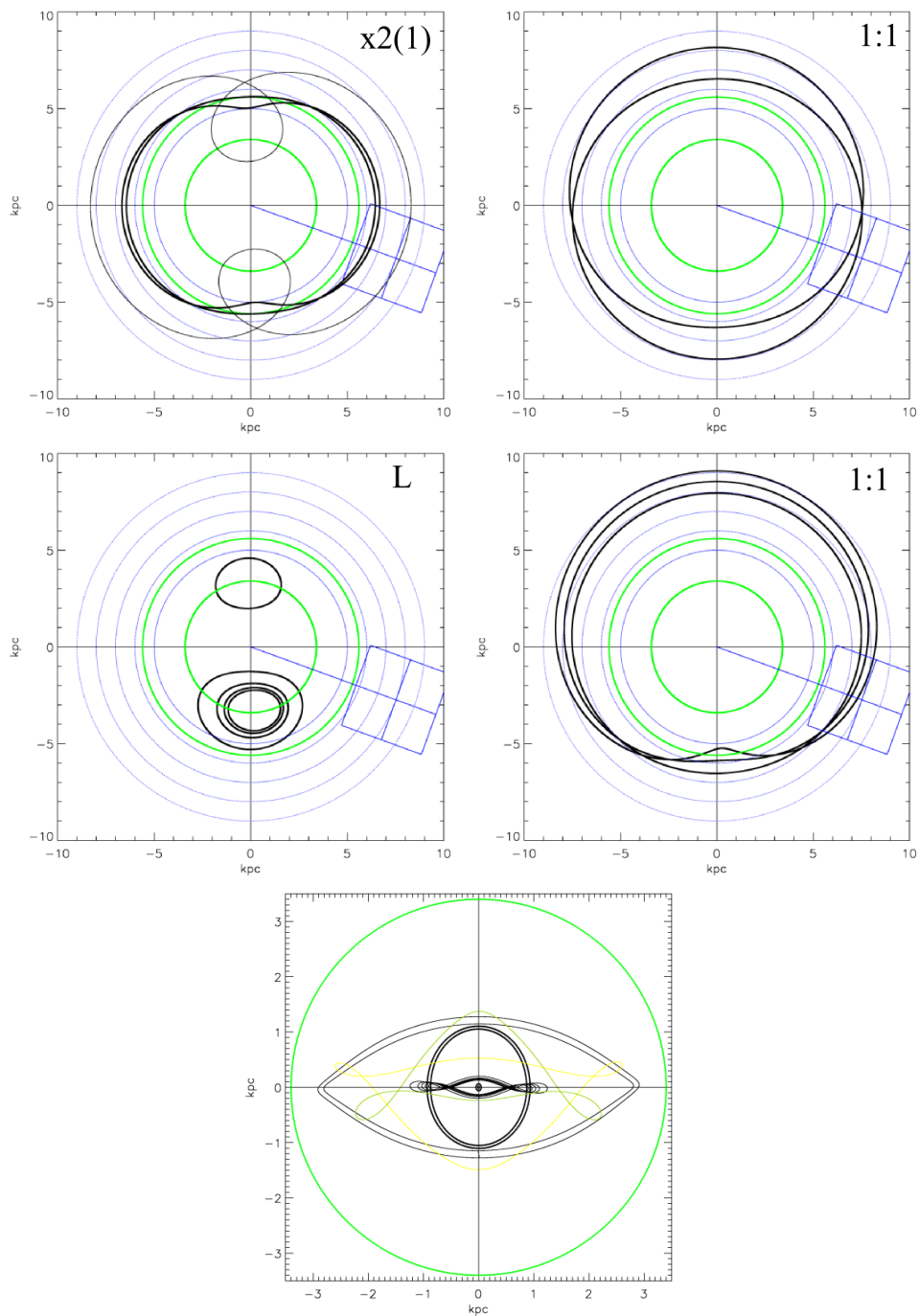
Figure 5.7: Upper left: x2(1) family members Upper right: 1:1 up and down Middle left: Lagrange Middle right: 1:1 Lower left: orbits inside the CR
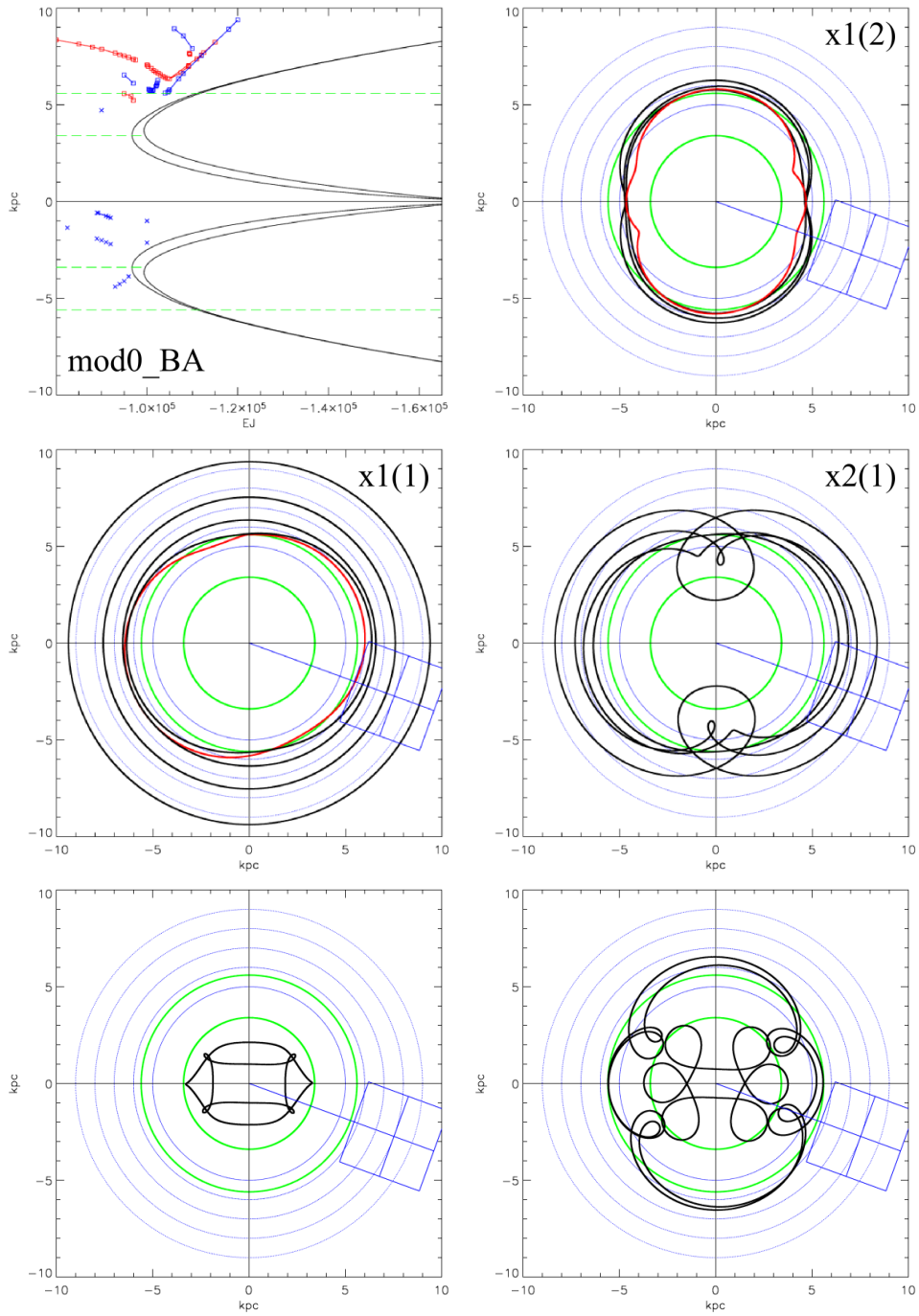
Figure 5.8: Upper left: characteristic diagram of mod0_BA Upper right: x1(2) family members Middle left: x1(1) family members Middle right: x2(1) family members Lower left: orbits inside the CR Lower right: loop orbits
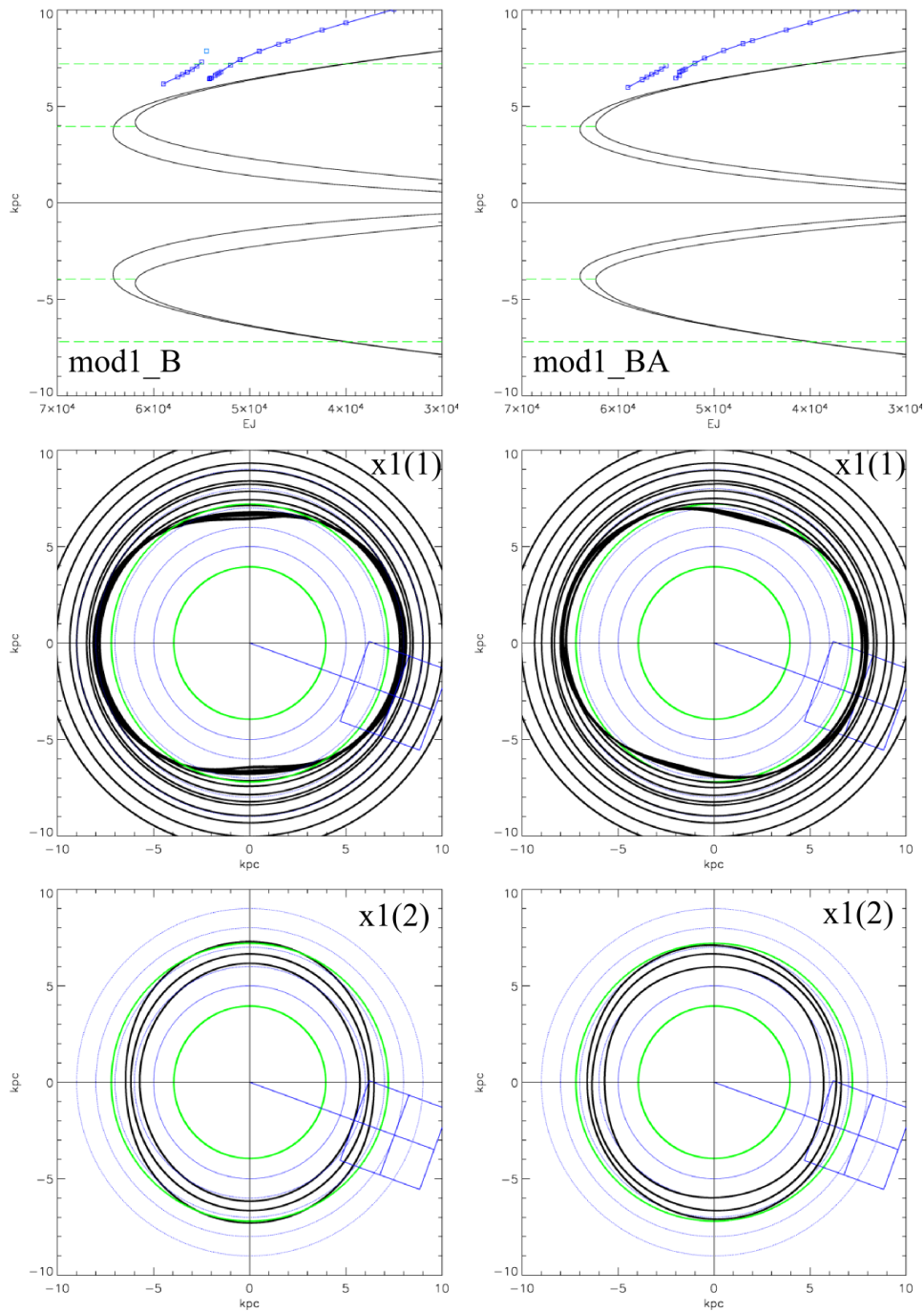
83

Figure 5.9: Upper left: characteristic diagram of mod1_B Upper right: characteristic diagram of mod1_BA Middle left: x1(1) of mod1_B Middle right: x1(1) of mod1_BA Lower left: x1(2) of mod1_B Lower right: X1(2) of mod1_BA

Chapter 6

Conclusions & Outlook

6.1 Conclusions

By analysing a sample of young stars in the nearby galactic disk we could learn something about effects enhanced by the global large-scale structure of our host Galaxy. Our main interest was the bar as an asymmetric feature.

Hydrodynamic modeling of the inner Galaxy suggests that the radius of the outer Lindblad resonance (OLR) of the Galactic bar lies in the vicinity of the Sun, (Dehnen, 2000). The question, how this resonance affects the nearby Galactic disk is of main interest: Is it possible to identify the resonance in the velocity distribution of observed stars in the solar neighbourhood? With detailed simulations Dehnen found out, that the influence of the bar is restricted to orbits that are nearly in resonance with it. This influence is strongest for the outer Lindblad resonance (OLR).

Dehnen's sample is strongly restricted to the solar neighbourhood. See Sec. 1.3.2 *Kinematics in the Solar Neighbourhood*. There the observed star density is highest and it is possible to make a local u-v diagram statistic.
We worked out a sample of young OB stars, which masks a $\pm 2.2\,\mathrm{kpc}$ square around the Sun. The stars do have complete phase space information. The size of our analysed area is as big that a star with an orbit passing nearby the Sun would spend more than 12% of its cycle on our field. So the space coverage of our FB10 sample is much more comprehensive than Dehnen's.
The main restriction for such an orbit analysis is given by the sample completeness. We made many tests (see Chap. 4) to verify our results and trust them. The noncircularity of the FB10 streamlines, within the error estimations, is well established. The OB streamlines are more elongated than those expected from circular orbits, especially for radii $R < \mathrm{R}_\odot$. These elongated flow-lines reach their minimum galactocentric radii at points that are located approximately on the line that connects the Sun with the Galactic Center. At $R > \mathrm{R}_\odot$ the streamlines seem to be slightly turned forward.

Our streamline result inspired us to research orbit families in asymmetric potentials with a higher ranking interest in regions, where more than one orbit family could be expected.

Motivated by Dehnen (2000) and Mühlbauer and Dehnen (2003) we tested the influence of bar resonance effects in a MW model. Known theories predict that there is a x1(1) and a x1(2) family crossing the OLR from each side resulting in an area hosting two different orbit families. Tests with the potential of the well established MW model from Bissantz et al. (2003) show, that the characteristic of our non-circular velocity field could be reproduced by the x1(2) family and the less prominent feature for $R > R_\odot$ streamlines by a family called 1:1. But the "desired" gas streamlines of the model were not positioned close enough to the Sun's observed field. Shifting the OLR by adding a halo component to the potential and with a slight reduction from the pattern speed, provoked an intersection between the wanted orbit families and the analysed OB star field. The ellipticity of the x1(2) orbits is prominent, for a better agreement with the observations we have to shift the OLR even further out, what we plan to do. But still the orientation of the orbits points along the major axis of the bar. To break this symmetry we added an arm potential and let it rotate with the same pattern speed as the bar. Our modeling showed that an inclination of the orbit families x1(1), as we see it in the observed field, can be reproduced by this technique.

We learnt that the bar alone can not explain the strong non-circular streamlines. Even before, Mühlbauer and Dehnen (2003) found that the radial motions of standards of rest can be seen to occur quite frequently, but can only reach magnitudes in the order of about $0.02\times$ the tangential component, corresponding to about $\pm 5\,\mathrm{km\,s^{-1}}$ for the Milky Way.
We used a four time stronger bar potential than they did, but also we had radial velocities not exceeding $\pm 10\,\mathrm{km\,s^{-1}}$. The OB stars demand huger values. For $R < R_\odot$ we found v_{rad} up to $\pm 30\,\mathrm{km\,s^{-1}}$. Additionally, a bar alone can not break the bar oriented symmetry to change the inclination of the periodic orbits. We could do that only with the help of a spiral arm potential. Interesting is, that the spiral arm potential used in the mod1_BA reproduces exactly the wanted orbit rotation of around 20°. Bissantz et al. (2003) used well established arm positions, by changing the potential from mod0 to mod1 we added only an additional halo component, but left the arm potential unchanged. So we expect, that another family in the same region would experience a comparable rotation.

6.2 Outlook

Dehnen (1998) and Famaey et al. (2005) found that structure in the velocity distribution depends on the type of star or stellar population investigated. We worked out a young OB star sample, but this could be done with different stellar types as well.

I already collected a Cepheids sample and an Open Cluster set. These candidates can not be called young, so the argument of "still behave like the gas" would not work anymore, but we could compare the different aspects of their velocity fields which would be interesting too.

In the Milky Way, as well as in many barred galaxies, the bar is not the only deviation from a smooth axisymmetric background. Most prominently, spiral arm structure and an elliptic (or oval) disk and/or halo add further non-axisymmetric perturbations. Simulations show that arm and bar features do not have the same pattern speeds (Bissantz et al., 2003).

In a next analysis we want to include these aspects as well. The presence of more than one perturbation can influence the stellar dynamics (Quillen and Minchev, 2005). For example, if the solar neighbourhood is affected by more than the bar, i. e., also by spirals, then stars at velocities between moving groups might be on chaotic orbits (Quillen, 2003), a factor that could cause a relatively large increase in their velocity dispersion with time.

(Quillen and Minchev, 2005) analysed resonance effects produced by arms. Their pattern speed is $\sim 18\,\mathrm{Gyr}^{-1}$. They expect that the closed orbits considered in their paper weakly oscillate or are weakly perturbed at the frequency of a Galactic bar. Only stars velocities associated with the Hercules stream that are influenced by the bar's OLR_{bar} should be strongly affected. Stars at lower velocities should be distant and so unaffected by the OLR_{bar}.

Further modeling with our method can perhaps help to find additional information about similar effects.

Appendices

A List of Spiral Arm Models

TABLE 2
15 Studies of the Spiral Arms in the Milky Way (Mid-2003 to Early 2005)

Reference	Pitch Angle (deg)	Number of Spiral Arms	Arm Shape[a]	Interarm Separation[b] (kpc)	Relative Weight[c]	Data Used
Russeil et al. (2005), Table 2	...	4	Log	...	2	Hα gas
Vallée (2005), Fig. 1	12	4	Log	2.5	1	Pulsar RM
Sewilo et al. (2004), Fig. 2	12	4	Log	3.3	2	Radio H ɪɪ regions
Könyves et al. (2004), Fig. 3	15	>2	...	4.0	2	Far-IR dust loops
Luna et al. (2004), Fig. 1a	12	4	Log	2.4	2	CO gas
Gómez & Cox (2004), Fig. 7	13	4	Log	2.9	1	Thermal gas
De Simone et al. (2004), Table 2	15	2	...	...	1	Optical stellar velocity
McClure-Griffiths et al. (2004), Fig. 3	12	4	Log	3.1	1	H ɪ gas density
Paladini et al. (2004), Fig. 12	14	4	Log	2.8	3	Radio H ɪɪ regions
Drimmel et al. (2003), Fig. 1	12	4	Log	3.7	1	Near-IR dust extinction
Cordes & Lazio (2003b), Fig. 9	15	4	Log	2.7	3	Thermal electrons
Melnik (2003), Fig. 3	5	2	Ring	1.8	1	OB associations
Negueruela & Marco (2003), Fig. 7	12	4	Log	...	2	O and B stars
Bissantz et al. (2003), Fig. 5	16	4	Log	...	2	Near-IR flux and gas
Watson et al. (2003), Fig. 3	12	4	Log	3.3	3	UC H ɪɪ regions
Median value	12	4	Log	2.9	...	
Unweighted mean (all data)	12.6	3.7	...	2.95	...	
Selected mean (only weight 2 and weight 3 data)	13.5	4.0	...	3.08	...	
Standard deviation of the mean	±0.7	±0.2	...	0.2	...	

[a] For the arm shape, the azimuthal angle φ follows a function of the radius r, $f(r)$.
[b] Distance between the Perseus arm and Sagittarius arm, going through the Sun's location.
[c] Relative weight 3 is best.

Figure A.1: Publication list of Spiral Arm studies analysed by Vallée (2005) (Table 2) he regarded publications between mid-2003 up to early 2005.
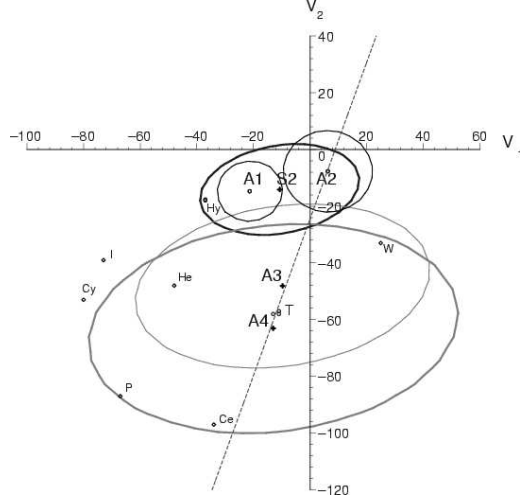
B Velocity Ellipsoids Analysis

Figure B.1: Projection of velocity ellipsoids, (V_1 points towards the GC, V_2 into the galactic rotation direction) radial heliocentric velocities for discrete populations obtained from local HIPPARCOS subsamples. Old disk stars were not obtained as a discrete stellar component, but as a broad wing of the young-disk population A_2. All together with early-type stars, A_1, they make up the thin disk component S_2. The subcomponent A_3 contains some old thin disk stars and a larger number of thick disk stars, that becomes the thick disk when wider local samples are considered. Notice that the populations A_1, A_2, A_3 and A_4, as well as the increasing thick disk populations T, obtained from sampling parameters $|\vec{V}| >= 145\,\mathrm{km\,s^{-1}}$, can be clearly fitted by a straight line. This fact is suggesting that all the local populations, except the early-type stars A_1, are moving in the same direction with respect to the thick disk component. They are dominated by a common differential galactic movement, mainly, but not only, in rotation. Some moving groups are also displayed so that they may be associated with any of the obtained major populations. The displayed moving groups are Hyades (Hy), Wolf 630 (W), ε Indi (I), ζ Herculis (He), 61 Cygni (Cy), σ Puppis (P), η Cephei (Ce). Other moving groups composed of young disk stars, like Pleiades and Sirius (not displayed) belong to the subcomponents A_1 and A_2, within the thin disk component S_2. In particular, the subcomponent A_1 may clearly be identified with the expanding local Gould's Belt structure (Alcobé and Cubarsi, 2005, Fig. 7).

C Spectral Characterisation

Two important laws were discovered during the 19th century relating to light and temperature. Wien's law (Wilhelm Wien 1893) stating that the wavelength (or color) of maximum intensity of a radiating solid is inversely proportional to its temperature

$$\lambda_{max} = \frac{2.898 \cdot 10^6 \, \text{nm K}}{T} \tag{7.1}$$

And the Stefan-Boltzmann law (1884) describing the relation between the total energy E radiated per unit surface area of a black body in unit time and its temperature T

$$E = \sigma T^4 \tag{7.2}$$

where $\sigma = 5.67 \cdot 10^{-8} \, \text{J s}^{-1} \, \text{m}^{-2} \, \text{K}^{-4}$ is the Stefan-Boltzmann constant. The luminosity L for a star with radius R is then given by $L = 4\pi R^2 \sigma T^4$. Knowing L and T, R can be easily calculated.

A first classification of stars was done 1866 by father Pietro Angelo Secchi which observed by eye prism spectra of about 4000 stars and divided those into four broad classes with common absorption features.

1. White - absorption lines mostly hydrogen

2. Yellow (sun-like) - strong calcium lines, weaker hydrogen

3. Red - many bunched bands, few hydrogen lines

4. Deep red - again, numerous bunched lines

In the late 1870's E.C. Pickering at Harvard observed about 220000 stars by prism photography and further refined Secchi's categories with the help of hired women acting as "computers" to analyse the spectra.

1. White - A,B,C,D

2. Yellow - E,F,G,H,I,J,K,L

3. Red - M

4. Deep red - N

The problem was that there was a class of stars which did not fit into the picture, showing very weak signs of lines but being blue-violet in color, therefore very hot. These stars were assigned the classification "O".

In 1901 Annie Jump Cannon, a supervisor of these hired women, noticed that the stellar temperature was the principle distinguishing feature among the different spectra. Most classes were thrown out as redundant, and within a few years one
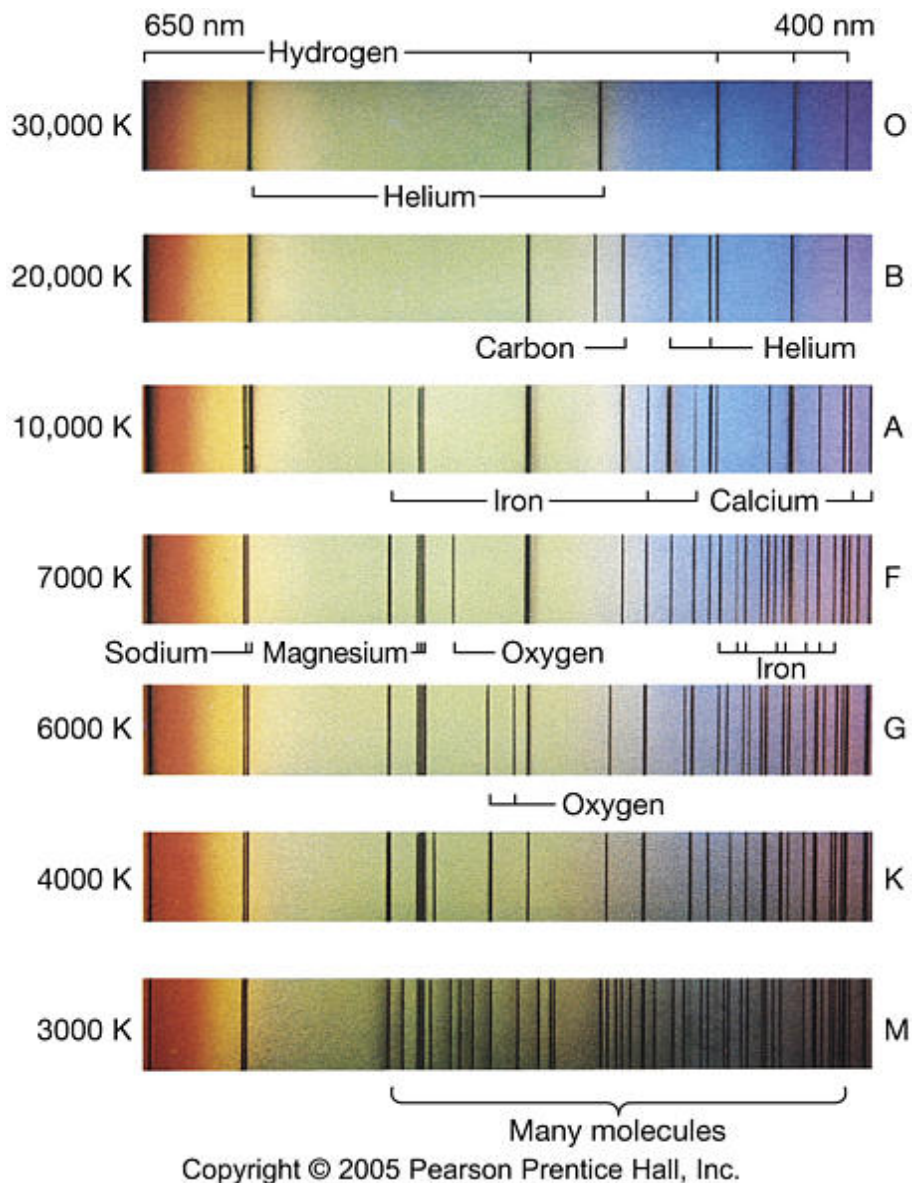
Figure C.1: Classification of the star types by its spectral lines and temperatures after Cannon. See text for the history how it evolved.

was left with the 7 primary classes we recognize today, namely **O B A F G K M**. Fig. C.1 shows representative spectral lines of each class.

More information can be gained by studying the relationship between the spectral class (color, temperature) and the luminosity (absolute magnitude), from which many properties (radius, mass, distance) about the star may be derived, knowing its brightness (apparent magnitude). Color and brightness are easy accessible observables, to get the luminosity one has to put in at least one of the three not so easy

to access values of radius, mass or distance. Nevertheless in 1913 this very useful relation was published by the american astronomer Henry Norris Russell. Since this had been suggested earlier by the German astronomer Hertzsprung, the diagram is known today as the Hertzsprung-Russell (HRD) (see Fig. C.2). Basically, the HRD shows that for the great majority of stars, the hotter the star is the more luminous it is. These stars fall along an s-shaped curve known as the main sequence. There are some stars, however, which are cool but luminous while others are hot with low luminosity. The Stefan-Boltzmann law above implies that the cool, bright stars must have very large diameters (hence the name, red giants), while the hot dim stars must have very small diameters and are therefore called white dwarfs.
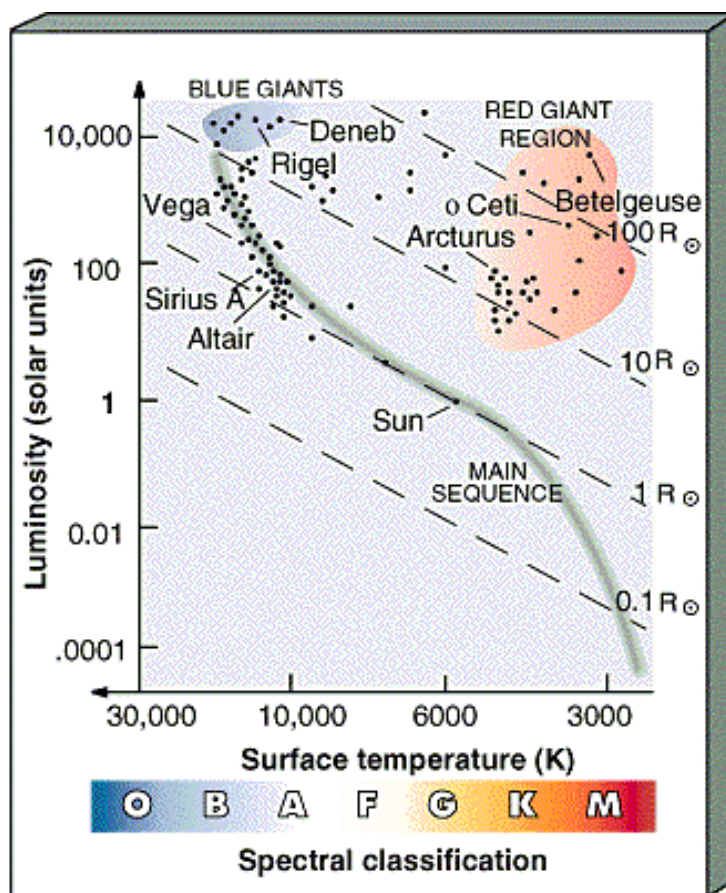

Figure C.2: Hertzsprung-Russel diagram ($http$: $//physics.uoregon.edu/\ jimbrau/BrauImNew/Chap17/FG17\_10.jpg$)
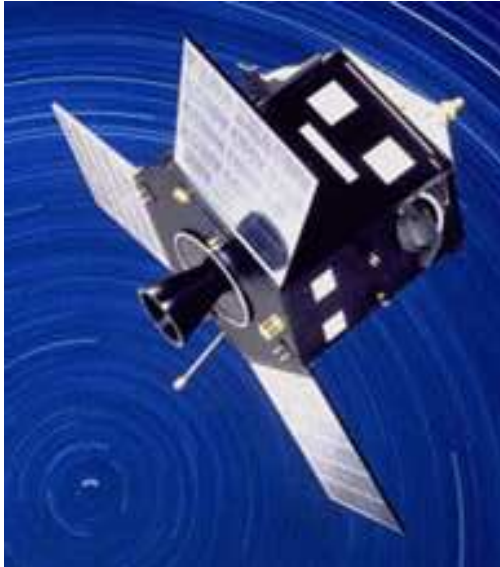
D Data & Catalogue

Figure D.1: An artist's conception of the Hipparcos satellite. ©ESA.

D.1 Hipparcos Satellite Mission

The Hipparcos satellite returned high quality scientific data from November 1989 to March 1993. The scientific goal of ESA's Hipparcos space astrometry project was to provide *positions*, *proper motions*, and *direct distance estimates* for more than 100′000 stars in the solar neighbourhood, in order to determine their physical properties, and to place theoretical studies of stellar structure and evolution, and studies of galactic structure and kinematics, on a more secure observational footing.

The available observing time could be used in an optimum manner, because of the continuous ecliptic-based scanning of the satellite. As a result of this high efficiency these datasets are of reasonably homogeneous sky density and uniform astrometric accuracy. The Hipparcos satellite had two viewing directions, separated by a large and suitable angle. This resulted in a rigid connection between quasi-instantaneous one-dimensional observations in different parts of the sky. So the determination of *trigonometric parallaxes* is absolute, with a high accuracy. Median astrometric standard errors (in position, parallax, and annual proper motion) are in the range $0.7 - 0.9$ mas for stars brighter than 9 mag (For more detailed information see Perryman et al., 1997).

Two catalogues have been the primary products of this mission: the **TYCHO** and the **HIPPARCOS catalogue**.

The Hipparcos catalogue, was completed in August 1996, and published in June 1997 (ESA 1997). Table D.1 represents a summary of its main astrometric and photometric properties.

Measurement period	$1989.85 - 1993.21$
Catalogue epoch	$J1991.25$
Reference system	$ICRS$
coincident with ICRS	$\pm 0.6\,\mathrm{mas}$
deviation from inertial[1]	$\pm 0.25\,\mathrm{mas}$
Number of entries	$118'218$
with associated astrometry	$117'955$
with associated photometry	$118'204$
Mean sky density	$\sim 3\ \mathrm{stars}\ deg^{-2}$
Limiting magnitude	$V \sim 12.4$
Magnitude completeness[2]	$V = 7.3 - 9.0$
Median σ_α at $J1991.25$[3]	$0.77\,\mathrm{mas}$
Median σ_δ at $J1991.25$[3]	$0.64\,\mathrm{mas}$
Median σ_π[3]	$0.97\,\mathrm{mas}$
Median $\sigma_{\sigma_\alpha \cos\delta}$[3]	$0.88\,\mathrm{mas\,yr^{-1}}$
Median σ_δ[3]	$0.74\,\mathrm{mas\,yr^{-1}}$
10% better than[4]	$0.47 - 0.66\,\mathrm{mas}$
Smallest errors[4]	$0.27 - 0.38\,\mathrm{mas}$
Distance $< 10\%(\sigma_\pi/\pi < 0.1)$	$20'853$
Distance $< 20\%(\sigma_\pi/\pi < 0.2)$	$49'399$
External errors/standard errors[5]	$\sim 1.0 - 1.2$
Systematic errors in astrometry[5]	$< 0.1\,\mathrm{mas}$

Table D.1: ICRS is the International Celestial Reference System (see also App. D.3. [1] about all 3 axes; [2] depending on galactic latitude and spectral type. [3] for $H_p \leq 9$ mag; [4] on each of the five astrometric parameters; [5] estimated from various investigations (Perryman et al., 1997, Table 1&2)

    The Tycho catalogue can be considered as an extension of the Hipparcos catalogue that is more complete at magnitudes $8 - 11$ but less accurate in data, see Fig. D.2.

The goal of the Tycho experiment on board the ESA Hipparcos space astrometry satellite was to provide astrometric and two-color photometric measurements of the brightest stars on the sky. The measurements were obtained with the Hipparcos star mapper, a system of aperiodic slits in the focal plane of the Hipparcos telescope designed primarily for determining the satellite attitude by observation of stars with known positions.

The astrometric accuracy varies strongly with magnitude, but the median uncertainties of Tycho positions and proper motions are a factor of 30 worse than those in the

Hipparcos catalogue. The large proper motion uncertainties make Tycho unsuitable for precise astrometric work.

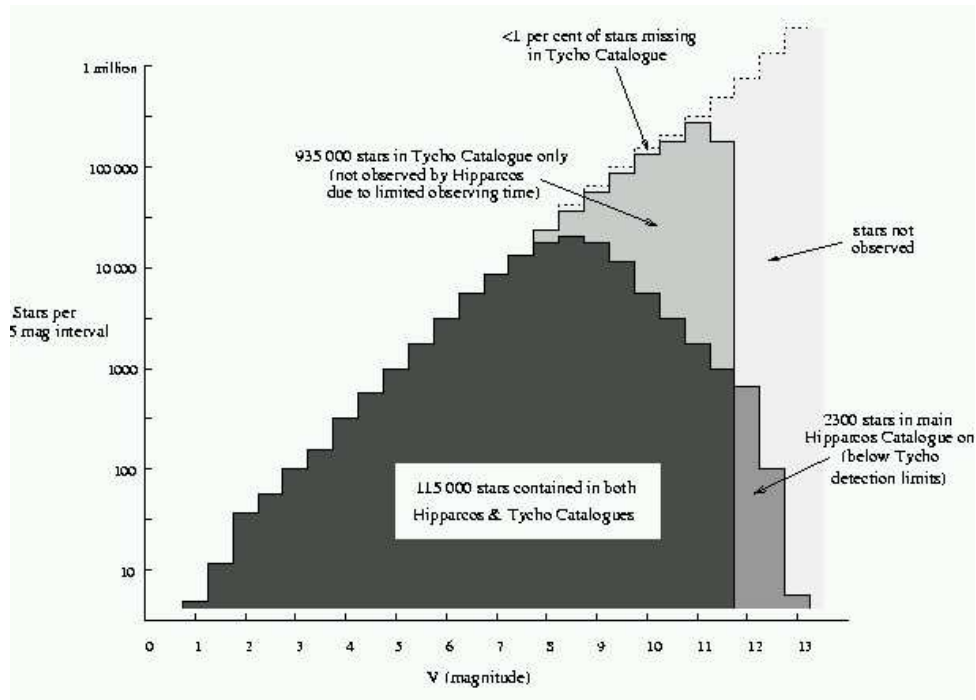A comparison of the completeness of these two catalogues is shown in Fig. D.2.

Figure D.2: Overlap and completeness of the 118′218 entries of the main Hipparcos catalogue and the Tycho catalogue. The former is largely complete to around $V = 7.3 - 9.0$ mag, depending on galactic latitude and spectral type. Other stars, with a roughly constant density over the celestial sphere, are included down to the observability limit of around $V = 12.5$ mag. The Tycho catalogue is largely complete to around $V = 10.5$ mag, and contains objects down to the limit of the Tycho observations, at around $V = 11 - 11.5$ mag. Consequently, most Hipparcos entries are contained in the Tycho catalogue, except for some 2300 entries below the Tycho detection threshold ($http : //www.rssd.esa.int/Hipparcos/CATALOGUE\_VOL1/sect1\_01.pdf$, Fig. 1.1.1.)

D.2 Catalogue Général de Vitesses Radiales Moyennes pour les Étoiles Galactiques
Cat. III/213

The Hipparcos catalogue does not include a complete list of radial velocity data. A complementation is **Cat. III/213**, a catalogue of *mean radial velocities* for Galactic stars (Barbier-Brossat and Figon, 1999). It supplements the catalogue WEB (Duflot

et al., 1995, Cat. III/190) with observations published through December 1990.
The catalogue contains new mean velocities for $20'574$ stars, altogether there are
$36'145$ stars presented. Only observations obtained with adequate spectral resolution
and standardised to the IAU or *Cat. III*/21 (Wilson, 1953) velocity systems have
been used.
For star indentification in this work HIC (out of $Cat.III/213$) $\equiv$ HIP (out of the
Hipparcos catalogue) is used as a matching criterion.
($http://www.rssd.esa.int/Hipparcos/CATALOGUE_VOL1/sect2_01.pdf$, p.106)

D.3   The International Celestial Reference System (ICRS)

Using data of different sources it is important to validate the reference systems
of each. Hipparcos and radial velocity data are represented in the International
Celestial Reference System **(ICRS)**. It is a fundamental celestial reference sys-
tem adopted by the International Astronomical Union **(IAU)** for high-precision
positional astronomy. The ICRS, with its origin at the solar system barycen-
ter and space fixed (i.e. kinematically non-rotating) axis directions is meant to
represent the most appropriate coordinate system for expressing reference data
on the positions and motions of celestial objects. (For more detail see: *http :
//aa.usno.navy.mil/faq/docs/ICRS_doc.html*.)
Each measurment depends on where, consequently also at which particular time, the
observation has been done. Different reference systems have to be transformed into
each other, this is problematic for high precision work. The accuracy with which
the motions of the objects are known is an essential factor in such computations. A
reference frame must be implemented at the time of actual observations, a specific
epoch has to be given. The adopted catalogue epoch is J1991.25, close to the mean
central epoch of the observations for each star.
A modern astrometric catalogue contains data on a large number of objects, so
the coordinate system is vastly overdetermined. The quality of the reference frame
defined by a catalogue depends on the extent to which the coordinates of all possi-
ble pairs of objects serve to define the identical equator and right ascension origin,
within the expected random errors. The ICRS is realised at optical wavelengths by
stars in the Hipparcos catalogue of $118'218$ stars, some as faint as visual 12 mag
(Esa, 1997). Only stars with uncomplicated and well-determined proper motions
(e.g., no known binaries) are used for the ICRS realisation.

D.4   Standard Model

The "standard model" of stellar motion has the physical underlying that stars move
through space with a constant velocity vector. Many stars together can represent a
common velocity field, each star is the representer of its position. After smoothing
the field, integrated streamlines can be defined. They can be seen as integral parts
of star orbits.

The five astrometric parameters given in the Hipparcos catalogue describe the instantaneous motion of the star relative to the solar system barycentre, in a plane perpendicular to the line of sight. The sixth parameter needed to completely specify the space motion is the radial velocity.

At some reference epoch, T_0, the stellar motion is then described by the following astrometric parameters:

$\alpha \pm \sigma_\alpha$	°	RA
$\delta \pm \sigma_\delta$	°	DE
$\pi \pm \sigma_\pi$	arcsec	parallax
$\rho \pm \sigma_\rho$	$\mathrm{km\,s^{-1}}$	radial velocity
$\mu_\alpha \pm \sigma_{\mu_\alpha}$	$\mathrm{arcsec\,yr^{-1}}$	proper motion
$\mu_\delta \pm \sigma_{\mu_\delta}$	$\mathrm{arcsec\,yr^{-1}}$	
k	$= 4.74047$	equal the AU expressed in $\mathrm{km\,s^{-1}\,yr}$

(α, δ) are called *right ascension* and *declination*, two angles which describe the position of a line of sight in the 3-dim space. The distance to the observed object is given by π the *trigonometric parallax*, from which the coordinate distance is $\frac{1}{\sin \pi} = d$ or, with sufficient approximation $\frac{1}{\pi} \cong 1\,\mathrm{pc}$ if π is expressed in arcsec. The rate of change of the barycentric coordinate direction expressed as *proper motion* components are $\mu_{\alpha*} = \mu_\alpha \cos \delta$ and μ_δ, in angular measure per unit time ($\mathrm{arcsec\,yr^{-1}}$). The $\cos \delta$ factor, signified by the asterisk in $\mu_{\alpha*}$, relates the rate of change of position in right ascension to great-circle measure. The proper motion is the projection of each star's space motion onto the celestial sphere, expressed as an angular rate in right ascension and declination per unit time. The velocity component along the line of sight is given by the *radial velocity* mainly measured in $\mathrm{km\,s^{-1}}$. k transforms the "AU"-units into "$\mathrm{km\,s^{-1}\,yr}$"-units.

D.5 Coordinate Systems

Coordinate systems are used to specify positions and motions of objects in space. We need 6 linearly independent informations to define a stars attributes. Many different frames are used, depending on their advantages and disadvantages for the task. Transformations from one system into another have to be done.

Equatorial System

One of the most fundamental reference system for observations made is the **equatorial system**. The Earth rotates eastward on its axis once a day, and, as a consequence, the sky appears to rotate westward about the Earth. The rotation axis extensions define the north and south celestial poles (NCP, SCP). The origin of the frame is given by the vernal equinox (VE). By intersecting the celestial equator and the ecliptic (plane defined by the rotation Earth $\leftrightarrow$ Sun) one got two intersection
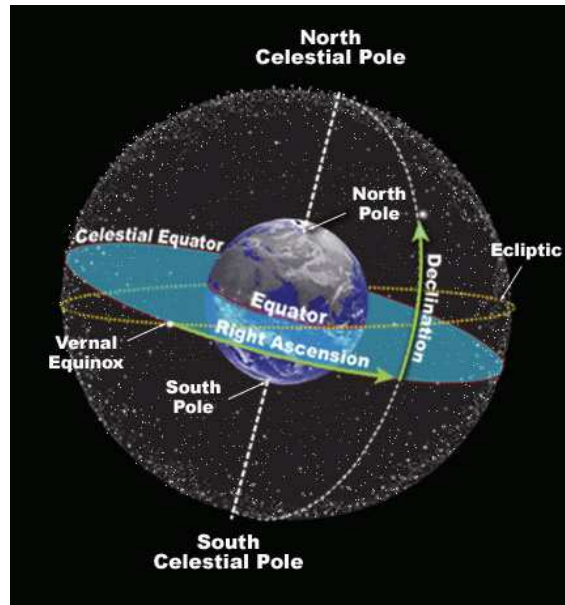
Figure D.3: Equatorial coordinate system

points separated by 180 °. At approximately March 21 the Sun passes VE moving from south to north. The angle between the two planes is $\sim$ 23.5 °.

This reference frame consists of two coordinates as shown in Fig. D.3. The right ascension α of an object is its angular distance measured eastward along the equator. The declination δ is its angular distance north or south of the celestial equator.

With the distance as a third information the object's position can be described.

Galactic Coordinates

The **galactic coordinates** define another reference system. It is useful to set up a galactic system of coordinates that has a direct physical connection with the structure of our Galaxy. The galactic equator is chosen to be the great circle that most closely approximates the plane of the MW. This plane is declined at an angle of $\sim$ 62.87 ° to the celestial equator. The north galactic pole (NGP) is located at $(\alpha_{NGP}, \delta_{NGP})$. It is defined by the line, running trough the Sun and standing perpendicular to the galactic equator, see Fig. D.4.

The galactic longitude l is oriented wrt the galactic center, where a compact radio source ($Sgr\ A^*$) now believed to mark its position. b the galactic latitude is the angle from the galactic equator to the star along the great circle (star↔NGP↔SGP).

Coordinate Transformation

The change from (α, δ) to (l, b) can be realised with the transformation matrix **T** derived below. A combination of 3 rotations around the angles α_{NGP}, δ_{NGP} as seen
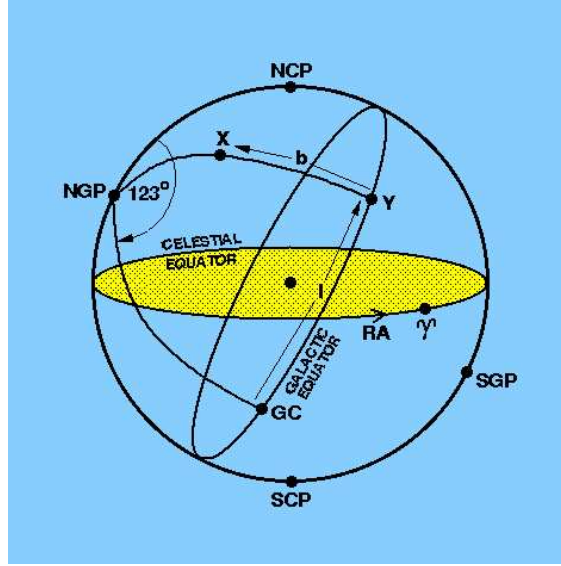
Figure D.4: Galactic coordinate system (l, b). S/NGP south/north galactic poles; S/NCP south/north celestial poles; GC galactic center; RA right ascension; Υ vernal equinox.

before and l_{NCP}, which represents the longitude of the NCP, is needed to perform this task. Table D.2 shows the values determined from the HC.

α_{NGP}	192.85948 °
δ_{NGP}	27.12825 °
l_{NCP}	122.93192 °

Table D.2: See *Transformation of Astrometric Data* (Hipparcos catalogue).

$$\mathbf{T}_1 = \begin{pmatrix} \cos(\alpha_{NGP}) & \sin(\alpha_{NGP}) & 0.0 \\ \sin(\alpha_{NGP}) & -\cos(\alpha_{NGP}) & 0.0 \\ 0.0 & 0.0 & 1.0 \end{pmatrix}$$

$$\mathbf{T}_2 = \begin{pmatrix} -\sin(\delta_{NGP}) & 0.0 & \cos(\delta_{NGP}) \\ 0.0 & -1.0 & 0.0 \\ \cos(\delta_{NGP}) & 0.0 & \sin(\delta_{NGP}) \end{pmatrix}$$

$$\mathbf{T}_3 = \begin{pmatrix} \cos(l_{NCP}) & \sin(l_{NCP}) & 0.0 \\ \sin(l_{NCP}) & -\cos(l_{NCP}) & 0.0 \\ 0.0 & 0.0 & 1.0 \end{pmatrix}$$

$$\boxed{\mathbf{T} = \mathbf{T}_3 * \mathbf{T}_2 * \mathbf{T}_1}$$

$$\begin{pmatrix} \cos(b)\cos(l) \\ \cos(b)\sin(l) \\ \sin(b) \end{pmatrix} = \mathbf{T} \begin{pmatrix} \cos(\delta)\cos(\alpha) \\ \cos(\delta)\sin(\alpha) \\ \sin(\delta) \end{pmatrix} \tag{7.3}$$

The work with models benefits a coordinate systems that supports the structure of our MW. We have chosen a set of right-handed cartesian axes (x, y, z). The xy-plane corresponds to the galactic disk and z points toward the NGP. x is oriented versus the GC and y in the direction of the Sun's rotational movement around the GC. (U, V, W) representing the velocities according to the same axes and orientations. To transform the catalogue data into a set of its corresponding $(X, Y, Z), (U, V, W)$ coordinates we work with the physical values and their uncertainties out of the described catalogue (see Sec. D.4).

Two additional rotations described by the matrix $\mathbf{A}(\alpha, \delta)$ are needed to match the velocity coordinates.

$$\boxed{\mathbf{A} = \mathbf{A}_1 * \mathbf{A}_2}$$

$$\mathbf{A}_1 = \begin{pmatrix} \cos(\alpha) & \sin(\alpha) & 0.0 \\ \sin(\alpha) & -\cos(\alpha) & 0.0 \\ 0.0 & 0.0 & -1.0 \end{pmatrix}$$

$$\mathbf{A}_2 = \begin{pmatrix} \cos(\delta) & 0.0 & -\sin(\delta) \\ 0.0 & -1.0 & 0.0 \\ -\sin(\delta) & 0.0 & -\cos(\delta) \end{pmatrix}$$

Instead of using the trigonometric parallax π in arcsec, we can just switch to the heliocentric star distance d given in pc. The identification is done by $d = 1/\pi$ and $\sigma_d^2 = \sigma_\pi^2/\pi^4$.

The velocity components are then given by

$$\begin{pmatrix} U \\ V \\ W \end{pmatrix} = \mathbf{B} \begin{pmatrix} \rho \\ k\mu_\alpha d \\ k\mu_\delta d \end{pmatrix}$$

where $\mathbf{B} = \mathbf{T} * \mathbf{A}$, and k corresponds to the unit transformer.

The measurement of the velocity components had been taken independently, so we can use the *gaussian error propagation* to define the **velocity errors**. By assuming that $\mathbf{T}$ and $\mathbf{A}$ are both independent of the errors in (U, V, W) and that only $\rho, \mu_\alpha, \mu_\delta, d$ do participate we found

$$\begin{pmatrix} \sigma_U^2 \\ \sigma_V^2 \\ \sigma_W^2 \end{pmatrix} = \mathbf{C} \begin{pmatrix} \sigma\rho^2 \\ k^2[\mu_\alpha^2\sigma_d^2 + d^2\sigma_{\mu_\alpha}^2] \\ k^2[\mu_\delta^2\sigma_d^2 + d^2\sigma_{\mu_\delta}^2] \end{pmatrix} +$$

$$+2\mu_\alpha\mu_\delta k^2\sigma_d^2 \begin{pmatrix} b_{12} * b_{13} \\ b_{22} * b_{23} \\ b_{32} * b_{33} \end{pmatrix}$$

where $\mathbf{C}$ is given by $c_{ij} = b_{ij}^2 \ \forall \ i,j$.

The transformation of the **positional coordinates** (α, δ, d) into (X, Y, Z) via (l, b) is expressed as

$$\begin{pmatrix} X \\ Y \\ Z \end{pmatrix} = \mathbf{d} \begin{pmatrix} \cos(b)\cos(l) \\ \cos(b)\sin(l) \\ \sin(b) \end{pmatrix} = \mathbf{d} * \mathbf{T} \begin{pmatrix} \cos(\delta)\cos(\alpha) \\ \cos(\delta)\sin(\alpha) \\ \sin(\delta) \end{pmatrix}.$$

As $[\cos(\delta)\cos(\alpha), \cos(\delta)\sin(\alpha), \sin(\delta)]$ corresponds to the first column of the matrix $\mathbf{A}$ with $(\mathbf{A}_{*1} = (a_{11}, a_{21}, a_{31})$, positional errors are derived like the velocity errors

$$\begin{pmatrix} \sigma_X^2 \\ \sigma_Y^2 \\ \sigma_Z^2 \end{pmatrix} = \mathbf{C} \begin{pmatrix} \sigma_d^2 \\ d^2\cos^2(\delta)\sigma_\alpha^2 \\ d^2\sigma_\delta^2 \end{pmatrix}.$$

Bibliography

Abadi, M. G., Navarro, J. F., Steinmetz, M., and Eke, V. R.: 2003, Ap J **597**, 21

Alcobé, S. and Cubarsi, R.: 2005, A & A **442**, 929

Amaral, L. H. and Lepine, J. R. D.: 1997, MNRAS **286**, 885

Armandroff, T. E.: 1989a, A J **97**, 1532

Armandroff, T. E.: 1989b, A J **97**, 375

Athanassoula, E.: 1984, Phys. Rep. **114**, 321

Barbier-Brossat, M. and Figon, P.: 1999, *VizieR Online Data Catalog* **3213**, 0

Barbier-Brossat, M. and Figon, P.: 2000, A&AS **142**, 217

Beers, T. C., Chiba, M., Sakamoto, T., Wilhelm, R., Allende Prieto, C., Sommer-Larsen, J., Newberg, H. J., Yanny, B., Marsteller, B., and Pier, J. R.: 2004, in *IAU Symposium*, pp 195–+

Benjamin, R. A., Churchwell, E., Babler, B. L., Indebetouw, R., Meade, M. R., Whitney, B. A., Watson, C., Wolfire, M. G., Wolff, M. J., Ignace, R., Bania, T. M., Bracker, S., Clemens, D. P., Chomiuk, L., Cohen, M., Dickey, J. M., Jackson, J. M., Kobulnicky, H. A., Mercer, E. P., Mathis, J. S., Stolovy, S. R., and Uzpen, B.: 2005, Ap J L **630**, L149

Binney, J.: 1992, ARA&A **30**, 51

Binney, J. and Gerhard, O.: 1996, MNRAS **279**, 1005

Binney, J., Gerhard, O., and Spergel, D.: 1997a, MNRAS **288**, 365

Binney, J., Gerhard, O. E., Stark, A. A., Bally, J., and Uchida, K. I.: 1991, MNRAS **252**, 210

Binney, J. and Merrifield, M.: 1998, *Galactic astronomy*, Princeton, NJ, Princeton University Press,1998, 796 p.

Binney, J. and Tremaine, J. S.: 1994, *Galactic dynamics*, Princeton, NJ, Princeton University Press,1994, 733p .

Binney, J. J., Dehnen, W., Houk, N., Murray, C. A., and Penston, M. J.: 1997b, in *ESA SP-402: Hipparcos - Venice '97*, pp 473–478

Bissantz, N., Englmaier, P., and Gerhard, O.: 2003, MNRAS **340**, 949

Bissantz, N. and Gerhard, O.: 2002, MNRAS **330**, 591

Blaauw, A.: 1952, Bull. Astron. Inst. Netherlands **11**, 414

Blum, R. D., Sellgren, K., and Depoy, D. L.: 1996, A J **112**, 1988

Bobylev, V. V.: 2004, *Astronomy Letters* **30**, 785

Campbell, W. W.: 1913, *Stellar motions, with special reference to motions determined by means of the spectrograph*, New Haven, Yale university press; [etc., etc.] 1913.

Carney, B. W., Latham, D. W., and Laird, J. B.: 1990, A J **99**, 572

Christopher, M. H., Scoville, N. Z., Stolovy, S. R., and Yun, M. S.: 2005, Ap J **622**, 346

Cole, A. A. and Weinberg, M. D.: 2002, Ap J L **574**, L43

Comeron, F.: 1993, PASP **105**, 441

Contopoulos, G.: 1980, A & A **81**, 198

Contopoulos, G. and Grosbol, P.: 1989, A&A Rev. **1**, 261

de Zeeuw, P. T., Hoogerwerf, R., de Bruijne, J. H. J., Brown, A. G. A., and Blaauw, A.: 1999, A J **117**, 354

Debattista, V. P., Gerhard, O., and Sevenster, M. N.: 2002, MNRAS **334**, 355

Dehnen, W.: 1998, A J **115**, 2384

Dehnen, W.: 2000, A J **119**, 800

Dray, L. M., Dale, J. E., Beer, M. E., Napiwotzki, R., and King, A. R.: 2005, MNRAS **364**, 59

Drimmel, R.: 2000, A & A **358**, L13

Duflot, M., Figon, P., and Meyssonnier, N.: 1995, A&AS **114**, 269

Dwek, E., Arendt, R. G., Hauser, M. G., Kelsall, T., Lisse, C. M., Moseley, S. H., Silverberg, R. F., Sodroski, T. J., and Weiland, J. L.: 1995, Ap J **445**, 716

Eggen, O. J.: 1998, A J **115**, 2397

Egret, D. and Fabricius, C.: 1997, in *ESA SP-402: Hipparcos - Venice '97*, pp 31–34

Eisenhauer, F., Schödel, R., Genzel, R., Ott, T., Tecza, M., Abuter, R., Eckart, A., and Alexander, T.: 2003, Ap J L **597**, L121

Elmegreen, B. G.: 1982, Ap J **253**, 655

Englmaier, P. and Gerhard, O.: 1996, in *ASP Conf. Ser. 112: The History of the Milky Way and Its Satellite System*, pp 191–+

Englmaier, P. and Gerhard, O.: 1999, MNRAS **304**, 512

Esa, .: 1997, *VizieR Online Data Catalog* **1239**, 0

Famaey, B., Jorissen, A., Luri, X., Mayor, M., Udry, S., Dejonghe, H., and Turon, C.: 2005, A & A **430**, 165

Feast, M. and Whitelock, P.: 1997, MNRAS **291**, 683

Frei, Z., Guhathakurta, P., Gunn, J. E., and Tyson, J. A.: 1996, A J **111**, 174

Fuhrmann, K.: 2004, *Astronomische Nachrichten* **325**, 3

Fux, R.: 1999, A & A **345**, 787

Fux, R.: 2001, A & A **373**, 511

Genzel, R., Hollenbach, D., and Townes, C. H.: 1994, *Reports of Progress in Physics* **57**, 417

Gerhard, O.: 2002, in *ASP Conf. Ser. 273: The Dynamics, Structure and History of Galaxies: A Workshop in Honour of Professor Ken Freeman*, pp 73–+

Gould, A.: 2003, Ap J **583**, 765

Gould, A.: 2004, Ap J **607**, 653

Gould, B. A.: 1879, *Resultados del Observatorio Nacional Argentino en Cordoba* 1

Hammersley, P. L., Garzón, F., Mahoney, T. J., López-Corredoira, M., and Torres, M. A. P.: 2000, MNRAS **317**, L45

Herschel, J. F. W. B.: 1847, *Results of astronomical observations made during the years 1834, 5, 6, 7, 8, at the Cape of Good Hope; being the completion of a telescopic survey of the whole surface of the visible heavens, commenced in 1825*, London, Smith, Elder and co., 1847.

Houk, N. and Smith-Moore, M.: 1988, in *Michigan Spectral Survey, Ann Arbor, Dept. of Astronomy, Univ. Michigan (Vol. 4) (1988)*, pp 0–+

Hubble, E. P.: 1926, Ap J **64**, 321

Ibata, R. A., Gilmore, G., and Irwin, M. J.: 1994, Nature **370**, 194

Kinman, T. D., Suntzeff, N. B., and Kraft, R. P.: 1994, A J **108**, 1722

Krabbe, A., Genzel, R., Eckart, A., Najarro, F., Lutz, D., Cameron, M., Kroker, H., Tacconi-Garman, L. E., Thatte, N., Weitzel, L., Drapatz, S., Geballe, T., Sternberg, A., and Kudritzki, R.: 1995, Ap J L **447**, L95+

Lin, C. C. and Shu, F. H.: 1964, Ap J **140**, 646

Lindblad, P. O., Palous, J., Loden, K., and Lindegren, L.: 1997, in *ESA SP-402: Hipparcos - Venice '97*, pp 507–512

López-Corredoira, M., Cabrera-Lavers, A., and Gerhard, O. E.: 2005, A & A **439**, 107

López-Corredoira, M., Hammersley, P. L., Garzón, F., Simonneau, E., and Mahoney, T. J.: 2000, MNRAS **313**, 392

Majewski, S. R., Polak, A. A., Law, D. R., and Rocha-Pinto, H. J.: 2005, in *ASP Conf. Ser. 338: Astrometry in the Age of the Next Generation of Large Telescopes*, pp 240–+

Martin, N. F., Ibata, R. A., Bellazzini, M., Irwin, M. J., Lewis, G. F., and Dehnen, W.: 2004, MNRAS **348**, 12

Mignard, F.: 1997, in *ESA SP-402: Hipparcos - Venice '97*, pp 5–10

Milgrom, M.: 1983, Ap J **270**, 365

Minniti, D., Olszewski, E. W., Liebert, J., White, S. D. M., Hill, J. M., and Irwin, M. J.: 1995, MNRAS **277**, 1293

Moreno, E., Alfaro, E. J., and Franco, J.: 1999, Ap J **522**, 276

Mühlbauer, G. and Dehnen, W.: 2003, A & A **401**, 975

Navarro, J. F., Helmi, A., and Freeman, K. C.: 2004, Ap J L **601**, L43

Newberg, H. J. and Yanny, B.: 2005, in *ASP Conf. Ser. 338: Astrometry in the Age of the Next Generation of Large Telescopes*, pp 210–+

Nikolaev, S. and Weinberg, M. D.: 1997, Ap J **487**, 885

Nordström, B., Mayor, M., Andersen, J., Holmberg, J., Pont, F., Jørgensen, B. R., Olsen, E. H., Udry, S., and Mowlavi, N.: 2004, A & A **418**, 989

Odenkirchen, M., Grebel, E. K., Dehnen, W., Rix, H.-W., Yanny, B., Newberg, H. J., Rockosi, C. M., Martínez-Delgado, D., Brinkmann, J., and Pier, J. R.: 2003, A J **126**, 2385

Olano, C. A.: 2001, A J **121**, 295

Ortiz, R. and Lepine, J. R. D.: 1993, A & A **279**, 90

Perrot, C. A. and Grenier, I. A.: 2003, A & A **404**, 519

Perryman, M. A. C., Lindegren, L., Kovalevsky, J., Hoeg, E., Bastian, U., Bernacca, P. L., Crézé, M., Donati, F., Grenon, M., van Leeuwen, F., van der Marel, H., Mignard, F., Murray, C. A., Le Poole, R. S., Schrijver, H., Turon, C., Arenou, F., Froeschlé, M., and Petersen, C. S.: 1997, A & A **323**, L49

Poppel, W.: 1997, *Fundamentals of Cosmic Physics* **18**, 1

Quillen, A. C.: 2003, A J **125**, 785

Quillen, A. C. and Minchev, I.: 2005, A J **130**, 576

Raboud, D., Grenon, M., Martinet, L., Fux, R., and Udry, S.: 1998, A & A **335**, L61

Reid, M. J.: 1993, ARA&A **31**, 345

Russeil, D.: 2003, A & A **397**, 133

Ryan, S. G. and Norris, J. E.: 1991, A J **101**, 1865

Schmidt-Kaler, T.: 1982, *Landolt-Bornstein: Numerical Data and Functional Relationships in Science and Technology*

Sellwood, J. A. and Wilkinson, A.: 1993, *Reports of Progress in Physics* **56**, 173

Shen, Z.-Q., Lo, K. Y., Liang, M.-C., Ho, P. T. P., and Zhao, J.-H.: 2005, Nature **438**, 62

Silk, J. and Wyse, R. F. G.: 1993, Phys. Rep. **231**, 293

Sirko, E., Goodman, J., Knapp, G. R., Brinkmann, J., Ivezić, Ž., Knerr, E. J., Schlegel, D., Schneider, D. P., and York, D. G.: 2004, A J **127**, 914

Smart, R. L., Drimmel, R., and Lattanzi, M. G.: 1997, in *ESA SP-402: Hipparcos - Venice '97*, pp 715–720

Smart, R. L., Drimmel, R., and Lattanzi, M. G.: 1999, in *Modern Astronomie and Astrodynamics.Kluwer*

Smart, R. L. and Lattanzi, M. G.: 1996, A & A **314**, 104

Sparke, L. S. and Gallagher, J. S.: 2000, *Galaxies in the universe : an introduction*, Galaxies in the Universe, by Linda S. Sparke and John S. Gallagher, III, pp. 416. ISBN 0521592410. Cambridge, UK: Cambridge University Press, September 2000.

Spergel, D. N., Malhotra, S., and Blitz, L.: 1996, in *Spiral Galaxies in the Near-IR, Proceedings of the ESO/MPA Workshop Held at Garching, Germany, 7-9 June 1995 edited by Dante Minniti and Hans-Walter Rix. Springer-Verlag Berlin Heidelberg New York. Also ESO Astrophysics Symposia (European Southern Observatory), 1996., p.128*, pp 128–+

Stanek, K. Z.: 1996, Ap J L **460**, L37+

Stanek, K. Z., Udalski, A., Szymanski, M., Kaluzny, J., Kubiak, M., Mateo, M., and Krzeminski, W.: 1997, Ap J **477**, 163

Steinmetz, M.: 1996, MNRAS **278**, 1005

Taylor, J. H. and Cordes, J. M.: 1993, Ap J **411**, 674

Torra, J., Fernández, D., and Figueras, F.: 2000, A & A **359**, 82

Vallée, J. P.: 2005, A J **130**, 569

van Loon, J. T., Gilmore, G. F., Omont, A., Blommaert, J. A. D. L., Glass, I. S., Messineo, M., Schuller, F., Schultheis, M., Yamamura, I., and Zhao, H. S.: 2003, MNRAS **338**, 857

Wahba, G. and Wendelberger, J.: 1980, *MWR* **108**, 1122

Weiland, J. L., Arendt, R. G., Berriman, G. B., Dwek, E., Freudenreich, H. T., Hauser, M. G., Kelsall, T., Lisse, C. M., Mitra, M., Moseley, S. H., Odegard, N. P., Silverberg, R. F., Sodroski, T. J., Spiesman, W. J., and Stemwedel, S. W.: 1994, Ap J L **425**, L81

Weiner, B. J. and Sellwood, J. A.: 1999, Ap J **524**, 112

Whyte, L. F., Abraham, R. G., Merrifield, M. R., Eskridge, P. B., Frogel, J. A., and Pogge, R. W.: 2002, MNRAS **336**, 1281

Wilson, R. E.: 1953, *Carnegie Institute Washington D.C. Publication* pp 0–+

Wyse, R. F. and Gilmore, G.: 2005, *astro-ph* **336**, 19

Zhao, H.: 2000, MNRAS **316**, 418

Zhao, H. and Mao, S.: 1996, MNRAS **283**, 1197

Acknowledgements

Als erstes möchte ich Herrn Prof. Ortwin Gerhard danken, dass er mir die Möglichkeit gegeben hat, in Basel zu promovieren. Seine Fähigkeit, komplexe Sachverhalte in einer klaren Sprache darzustellen und sein tiefes Verständnis für die Naturwissenschaften sind bewundernswert. Gerne erinnere ich mich auch an manch persönliches Gespräch über Gott und die Welt.

Herzlichen Dank geht auch an Herrn Prof. Burkard Fuchs, der sich, trotz sehr engem Zeitrahmen, bereit erklärt hat, als Co-Examinator meine Arbeit zu beurteilen.

Ganz speziell möchte ich Herrn Prof. Gustav A. Tammann danken. Nicht nur, weil er spontan den Beisitz meiner Prüfung übernommen hat, sondern in erster Linie wegen seiner herzlichen Art. Es hat mir immer grosse Freude bereitet, mich mit ihm zu unterhalten, und ich habe so manche interessante Anekdote aus dem guten alten "Basler-Deigg" in Erinnerung.

Peter Englmaier hat mir seine Orbit-Programme überlassen und auch sonst kräftig an meinem "Werk" mitgearbeitet. Dafür möchte ich ihm gerne danken. Seine Codes sind in derart übersichtlicher Art programmiert, dass ich viel davon lernen konnte, und durch die geplante Weiterführung unseres Projekts werden sicherlich noch einige spannende Lektionen auf mich zukommen. Ich freue mich darauf.

Another important person throughout my thesis was Niranjian Sambhus. His huge knowledge of physics impressed me. And it is every time fascinating to see how he reduces complex theories into a few clear comprehensive sentences. Special thanks to him as well for all the ideas, suggestions, and the support regarding his corrections of my thesis.
He additionally showed me that talented Indian cookers like he is one, can start loving "Sauerkraut and Bratwurst". A pity for the kitchen crew who liked to test his new Indian food creations.
I would also like to thank his wife Asmita. In the beginning of their residence in Switzerland she spent many hours in the Institute working at the computer. With her presence she doubled the number of women in the institute. I enjoyed very much our lunch time talks.

Thanks to Ayshe Siddiki. I liked very much to have her as my room mate. We had many interesting talks about our different cultures and I could learn a lot about her beautiful country. We will meet soon in Garching at the MPE. I'm already looking forward to it and I am sure we will spend many more nice hours together.

Herzlichsten Dank geht auch an Karin Ammon. Wir verbrachten unzählige Stunden bei "Guäzli" und Kaffee und haben über das Leben philosophiert. Die Stunden sind nur so dahingeflogen, denn es wird uns wohl nie der Gesprächsstoff ausgehen. Ich habe diese intensive Zeit sehr genossen und freue mich auf weitere Analysen und Interpretationen des Weltgeschehens.

Keinesfalls möchte ich die Küchentruppe unerwähnt lassen. Herrlich fand ich die Stunden, die wir bei gemeinsamem "Gebrutzel" verbracht haben. Steffis kulinarische Ausflüge waren häufig etwas gewagt. Andrea's Apfelstrudel mit Vanilleeis ist ein Genuss, und an die fröhlichen Gespräche mit ihr werde ich mich noch lange erinnern. Katrin's und Katharina's Tütenprodukte werden sicherlich auch bald in Haute Cuisine Gerichte umgewandelt. Piet jedoch wird weiterhin alles mit Mayo und Ketchup verfeinern.
Leute, es war eine super Zeit, und ich werde euch alle vermissen!

Gerne möchte ich auch meiner Familie danken. Für ihre Unterstützung durch all die Jahre. Ganz besonders hat mir meine "Mami" geholfen. Unsere Frauentage sind einsame Spitze und ich konnte jeweils sehr viel Energie tanken. Es ist schön so eine tolle Freundin als Mutter zu haben.

Ganz gewiss darf auf dieser Liste Christoph Ellenberger nicht fehlen. Er hat mich all die Jahre unterstützt und im Endspurt hat er mir so manches Leben gerettet. "Lieber Christoph, ich widme dir meine Arbeit und behalte in Erinnerung, wie schön diese anspruchsvolle Zeit war. Mit dir an meiner Seite machte selbst diese grausige Abschluss-Phase Spass."

Eines muss hier noch hinzugefügt werden:

Meine Einstellung zum Ausspruch: *"Mach kei Doktor druss"*
hat sich im letzten Halbjahr grundlegend geändert. ;-)

Curriculum Vitae

Name:	Caroline Girard
Born:	October 29, 1971 in Liestal
	citizen of Grenchen (Switzerland)

1977-1986	Primary- and *Bezirks*-school in Grenchen, Switzerland

1986-1990	Gymnasium (Collége de Gambach) in Fribourg, Switzerland
December 1990	Matura type E (Economics, in a French speaking class)

1991-1993	Studies at the *École Polytechnique Fédérale de Lausanne* (EPFL)
	Cours de Mathématiques Spéciales (CMS),
	First year of *Section de génie mécanique*,

1993-1998	Studies in Mathematics at the University of Basel, Switzerland
spring 1999	Diploma thesis at the Mathematical Institute of Basel
	"Einheitliche Feldtheorie, eine Weiterentwicklung der ART"
	supervised by Prof. Dr. H.-C. Im Hof

1999-2000	Teaching at Gymnasiums in Basel, Switzerland

October 2000	Start of the PhD thesis at the Astronomical Institute
	(UNI Basel) in Prof. Dr. Ortwin Gerhard's group
January 2006	End of the PhD thesis
	"Kinematics of OB stars in the nearby galactic disk"

During my studies I heard lectures given by:
(Mathematics) Prof. Dr. C.Bandle, Prof. Dr. N.A'Campo, Prof. Dr. J.Escher, Prof. Dr. H.Kraft, Prof. Dr. D.Kotschik, Prof. Dr. D.Masser, Prof. Dr. B.Scarpellini, Prof. Dr. H.Walser, (Physics) PD Dr. H.Muehry, Prof. Dr. H.Rudin, Prof. Dr. I.Sick, Prof. Dr. L.Tauscher, Prof. Dr. F.K.Thielemann, Prof. Dr. D.Trautmann, (Astronomy) PD Dr. B.Binggeli, Prof. Dr. R.Buser, Prof. Dr. O.E.Gerhard, Prof. Dr. G.A.Tammann.

Declaration

Ich erkläre, dass ich die Dissertation *"Kinematics of OB stars in the nearby galactic disk"* nur mit der darin angegebenen Hilfe verfasst und bei keiner anderen Fakultät eingereicht habe.

Basel, den 31. Januar 2006

Caroline Girard

" ... *und wenn gar nichts mehr hilft, dann hilft* **Schoggi** ... "

Zitat von Andrea Kayser